https://ntrs.nasa.gov/search.jsp?R=19730001548 2018-07-24T21:38:33+00:00Z

2-P
mix

[redacted]

VET. TES MEN NOV. TA- TUM

DEI VIGET SUB NUMINE

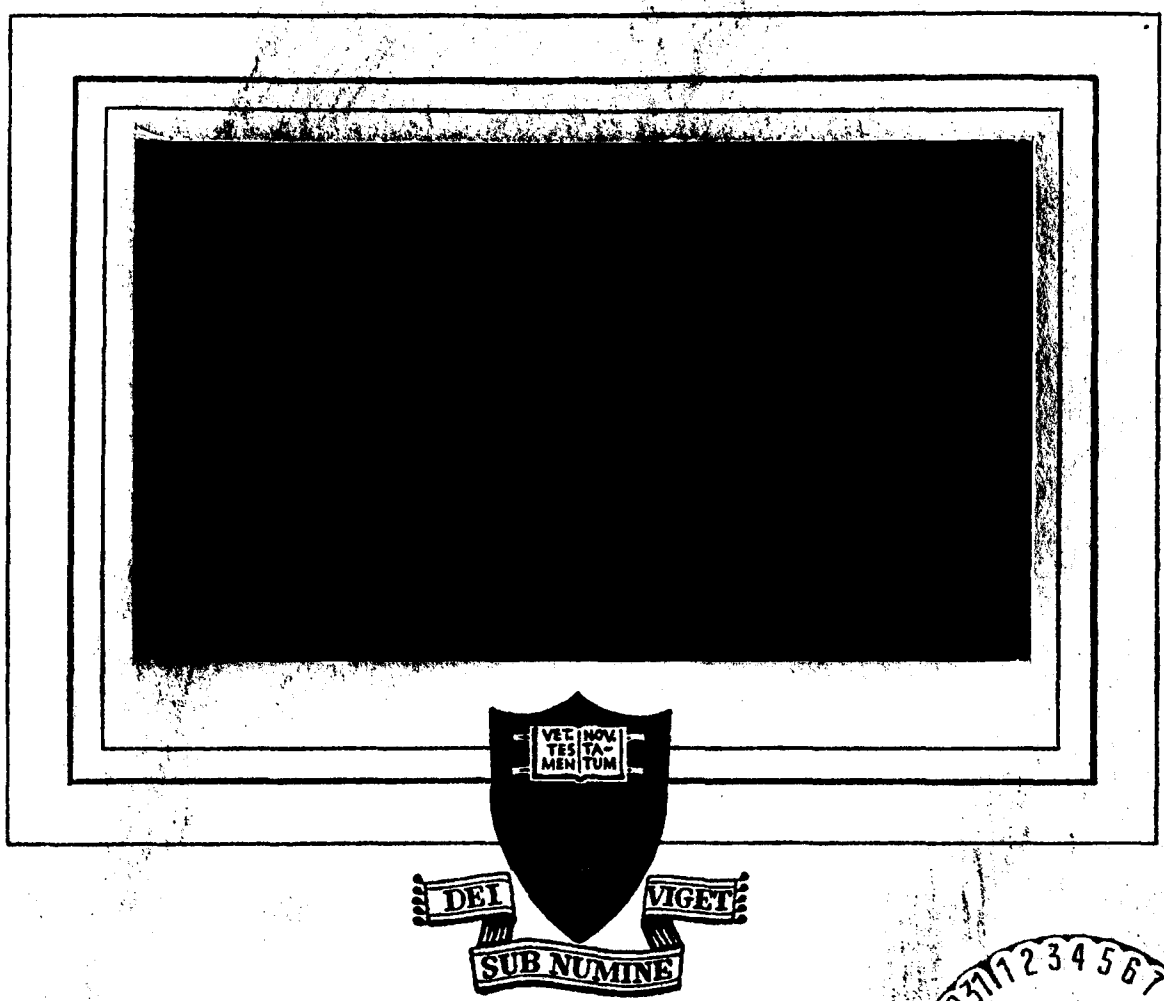

(NASA-CR-128408) ENERGY DEPOSITION IN PARALLEL-PLATE PLASMA ACCELERATORS Ph.D. Thesis M.S. DiCapua (Princeton Univ.) Dec. 1971 178 p CSCL 14B

N73-10275

Unclas
G3/11 15501

OCT 7 P
RECEIVED
NASA STI FACILITY
INPUT BRANCH

PRINCETON UNIVERSITY

DEPARTMENT OF

AEROSPACE AND MECHANICAL SCIENCES

Prepared for
National Aeronautics
and Space Administration
NASA Research Grant NGL 31-001-005

ENERGY DEPOSITION IN PARALLEL-PLATE PLASMA ACCELERATORS

M. S. Di Capua and R. G. Jahn

Report 1015*

Prepared by _____
MARCO S. DI CAPUA

Approved by _____
ROBERT G. JAHN
Dean, School of Engineering
and Applied Science, and
Principal Investigator

*This report is a reproduction in entirety of the Ph.D. dissertation of Mr. Marco S. Di Capua. It is submitted to the sponsor and to the distribution list in this form both as a presentation of the technical material, and as an indication of the academic program supported by this Grant.

Reproduction, translation, publication, use and disposal in whole, or in part, by or for the United States Government is permitted.

December 1971

School of Engineering and Applied Science
Department of Aerospace and Mechanical Sciences
Guggenheim Aerospace Propulsion Laboratories
PRINCETON UNIVERSITY
Princeton, N. J. 08540

Details of illustrations in this document may be better studied on microfiche

ABSTRACT

To appraise the ratio of energy deposition into kinetic and thermal modes in plasma accelerators, a parallel-plate plasma accelerator has been operated in the quasi-steady mode with current pulses in the range of 10 to 100 kiloamperes (kA), durations of the order of one millisecond, and argon mass flows up to 100 grams/sec. From photographic observations, spectroscopic measurements of velocity and electron density, and pressure measurements with a fast-rise piezoelectric transducer it is found that, for currents between 50 and 90 kA, the accelerated argon plasma is supersonic with ion velocities of 5 to 6 kilometers/sec, electron densities of 4 to 7 x 10^{22} m^{-3}, and static pressures of 0.3 to 0.5 atm. A momentum and energy balance obtained through a one-dimensional analysis shows that 85% of the input power (10 to 20 megawatts) delivered to the plasma appears in the exhaust flow. However, only 20% of the power in the exhaust appears as directed kinetic energy of the flow. The remainder appears as enthalpy of the flow which includes ionization. A magnetic boundary layer model explains some of the details of the discharge region. Efficient recovery of the thermal energy in the plasma by an expansion is precluded by the constant cross section of the flow channel. Therefore the parallel-plate plasma accelerator cannot exhibit the high performance typical of coaxial magnetoplasmadynamic (MPD) arc devices. The ratio of kinetic energy to enthalpy shows reasonable agreement with the ratio of induced emf to the resistive voltage drop. Both ratios indicate that the discharge imparts more energy to the flow by resistive heating than by direct body force acceleration.

CONTENTS

	Page
TITLE PAGE.	i
ABSTRACT.	ii
CONTENTS.	iii
LIST OF ILLUSTRATIONS	v
TABLES.	viii
Chapter	
1. INTRODUCTION	1
2. THE POWER SOURCE	5
2.1 Introduction	5
2.2 The "LC-Ladder" Network	6
2.3 Design of the Network	16
a. The Capacitors	16
b. The Proposed Network	19
c. The Inductors	20
d. Capacitor Fuses	22
e. Assembly of the Network	26
f. The Ballast Resistor	29
g. Accelerator Connections	32
h. The Charging Supply	35
i. Performance of the Power Source	35
3. THE PARALLEL-PLATE ACCELERATOR SYSTEM.	43
3.1 Introduction	43
3.2 The Accelerator Channel	43
3.3 The Shock Tube Mass Injection System	46
3.4 The Switch	54
4. EXPERIMENTAL OBSERVATIONS.	59
4.1 Introduction	59
4.2 Current and Voltage Measurements	59
4.3 Aerodynamic Observations of the Flow	63
4.4 Photographic Observations of the Discharge Region	67
4.5 Spectroscopic Studies	72
a. General Observations	72
b. Electron Density Measurements	78
c. Velocity Measurements	84
4.6 Wall Pressure Measurements	89
a. The Pressure Probe	90
b. Probe Response and Calibration	92
c. Results	97
4.7 Magnetic Field Measurements	102

CONTENTS-cont'd.

Page

5. ENERGY DEPOSITION IN THE PARALLEL-PLATE PLASMA ACCELERATOR. 106

5.1 Introduction 106
5.2 The Conservation Relations 107
a. Mass Conservation 107
b. Momentum Conservation 107
c. Energy Conservation 109
5.3 The Steady One-Dimensional Approach 110
5.4 Experimental Results 113
5.5 Interpretation of the Data 117
a. Momentum Conservation 117
b. Energy Conservation 121
c. The Energy Deposition Ratio 123
d. Viscous Dissipation and Heat Transfer 126

6. SUMMARY AND CONCLUSIONS 128

Appendices

A. THE LAM ACCELERATOR GEOMETRY. 130

A.1 Introduction 130
A.2 Experimental Observations 132
a. Terminal Measurements 132
b. Photographic Observations of the Discharge Region 132
c. Electron Density Measurements 136
d. Pressure Measurements 139
e. Magnetic Field Measurements 143
A.3 Momentum and Energy Balance 145
A.4 The Convection-Diffusion Model for the Acceleration Region 149

B. PHOTOGRAPHIC DETERMINATION OF LINE HALF-WIDTHS 157

B.1 Introduction 157
B.2 Determination of γ 158
B.3 Determination of the Half-Intensity Point 162

REFERENCES 167

LIST OF ILLUSTRATIONS

Figure		Page
1-1	Parallel-Plate Accelerator	3
2-1	Calculated Current Waveforms	8
2-2	Current in 4 Element Network	9
2-3	Effect of Parasitic Inductance on Current Waveform	12
2-4	GE Capacitor Unit	18
2-5	Voltage and Current in Fuse Test	25
2-6	Schematic of Network Section	27
2-7	Diagram of Network Section	28
2-8	Resistivity of Cupric Sulfate Solution as a Function of Concentration	33
2-9	View of Electrolytic Resistor	34
2-10	View of Power Source	36
2-11	Network Configurations	38
2-12	Current Pulses, V_o = 4.6 kV	39
2-13	Voltage Across R_B and Decay of Current Pulse	41
3-1	Schematic of Parallel-Plate Accelerator System	44
3-2	Parallel-Plate Accelerator System	45
3-3	Shock Tube Injector	47
3-4	Photograph of Shock Tube	48
3-5	Stagnation and Static Pressure Records	50
3-6	Gas-Prism Schlieren Densitometer	52
3-7	Stagnation Temperature at Driven Section End Wall - Driver Pressure: 2.1 atm (Argon)	55
3-8	Stagnation Temperature at Driven Section End Wall - Driver Pressure: 3.2 atm (Argon)	56
3-9	Schematic of Switch	57
4-1	Current and Voltage Signatures (100 μ Ambient Argon)	62
4-2	Current and Voltage Signatures - I = 89 kA, $\dot{m}$ = 96 g sec^{-1}	64

LIST OF ILLUSTRATIONS-cont'd

Figure		Page
4-3	Voltage as a Function of Current, Parallel-Plate Accelerator	65
4-4	Flow Over Wedge	66
4-5	Mach Number as Function of Deflection Angle	68
4-6	Mach Number as a Function of Current	69
4-7	Photographs of Accelerator Operation (Side View) I=85 kA, $\dot{m}$= 96 g sec^{-1}	71
4-8	Photographs of Accelerator Operation (Perspective) I=85 kA, $\dot{m}$ = 96 g sec^{-1}	73
4-9	Optical Arrangement	75
4-10	Parallel-Plate Accelerator Spectra I = 85 kA, $\dot{m}$ = 96 g sec^{-1}	77
4-11	Electron Density as a Function of Half Width	80
4-12	Stark Broadening of H_β , + 22.7 cm I = 85 kA, $\dot{m}$ = 96 g sec^{-1}	81
4-13	Electron Density Profiles, + 22.7 cm	83
4-14	Electron Density Contours I = 85 kA, $\dot{m}$ = 96 g sec^{-1}	85
4-15	Doppler Shift Measurement	87
4-16	Velocity as a Function of Current, $\dot{m}$ = 96 g sec^{-1}	88
4-17	Pressure Probe	91
4-18	Pressure Probe Calibration and Response	93
4-19	Yanked Weight Calibration of Pressure Probe (1000 pF Feedback Capacitor)	95
4-20	Pressure Measurements, I = 57 kA, $\dot{m}$ = 96 g sec^{-1}	98
4-21	Pressure Measurement, I = 72 kA, $\dot{m}$ = 96 g sec^{-1}	99
4-22	Pressure Measurements, I = 85 kA, $\dot{m}$ = 96 g sec^{-1}	100
4-23	Normalized Magnetic Field B/B_1 I = 85 kA, $\dot{m}$ = 96 g sec^{-1}, t=80-200 usec	104

LIST OF ILLUSTRATIONS-cont'd

Figure		Page
5-1	Schematic of Parallel-Plate Accelerator	111
5-2	Terminal and Pressure Measurements	114
5-3	Electron Density Profile	116
A-1	Parallel-Plate Accelerator-Lam Geometry	131
A-2	Terminal Properties - Lam Geometry	133
A-3	Current Voltage Characteristic $\dot{m}$ = 96 g sec^{-1} (Lam Geometry)	134
A-4	Photographs of Accelerator Operation (Side View) I = 85 kA, $\dot{m}$ = 96 g sec^{-1} (Lam Geometry)	135
A-5	Electron Density Profiles (Lam Geometry)	137
A-6	Electron Density Profiles (Lam Geometry)	138
A-7	Pressure Measurements, I = 57 kA, $\dot{m}$ = 96 g sec^{-1} (Lam Geometry)	140
A-8	Pressure Measurements, I = 72 kA, $\dot{m}$ = 96 g sec^{-1} (Lam Geometry)	141
A-9	Pressure Measurements, I = 85 kA, $\dot{m}$ = 96 g sec^{-1} (Lam Geometry)	142
A-10	Normalized Magnetic Field B/B_1 I = 86 kA, $\dot{m}$ = 96 g sec^{-1} t = 80 - 200 μsec (Lam Geometry)	144
A-11	Magnetic Boundary Layer Model	152
A-12	Summary of Experimental Observations (Lam Geometry)	155
B-1	Density as Function of Exposure	159
B-2	Optical Arrangement for Film Calibration	160
B-3	Idealized Transmission Profile	163
B-4	Transmission Factor Ratios	166

TABLES

TABLE		Page
5-I	Momentum Conservation	119
5-II	Energy Conservation	119
5-III	V_{uB} For Different Velocity and Current Density Distributions	125
A-I	Momentum Conservation (Lam Geometry)	146
A-II	Energy Conservation (Lam Geometry)	146

CHAPTER 1

INTRODUCTION

The advantage of electric thrusters for space propulsion over chemical and nuclear rockets consists of their ability to accelerate propellants to a high velocity. This property enables delivery of a large fraction of the initial mass to a given destination.[1] Of all the electric propulsion systems available today (electrostatic, electromagnetic, electrothermal), the magnetoplasmadynamic (MPD) accelerator, which is a hybrid of the electromagnetic and electrothermal varieties, is unique inasmuch as it combines two highly desirable properties: a high exhaust velocity ($1\text{-}2 \times 10^4$ m sec^{-1}) as well as a high thrust density ($\sim 5 \times 10^4$ N m^{-2}), a combination which is not available in purely electrostatic or electrothermal thruster systems.

Since the mass delivered to destination by all electric thruster systems consists of the powerplant mass in addition to the payload mass, the powerplant mass must be kept as small as possible. Therefore, to realize fully the advantages offered by the high exhaust velocity and high thrust density capability the system must satisfy two requirements: a high overall efficiency of the acceleration process, i.e., the conversion of electrical input power into kinetic energy of the exhaust beam, and a low specific mass for the powerplant.

In any MPD accelerator, the overall efficiency of the acceleration process heavily depends on the initial apportionment of input power to the kinetic and thermal modes of the plasma in the discharge region. Some of the thermal energy deposited in the plasma may subsequently be recovered as directed kinetic energy by flow expansion downstream of the discharge region. However, irreversible processes such as heat transfer to electrodes and other surfaces, radiation

frozen flow effects and free expansion into vacuum invariably limit this recovery. High performance accelerators should therefore minimize the fraction of input power initially delivered to plasma heating.

The task of assessing the initial energy deposition ratio to kinetic and thermal modes of the plasma in an MPD accelerator requires a detailed knowledge of the electromagnetic fields, gasdynamic flow fields and the thermodynamic state of the plasma in the acceleration region. This task is complicated by difficulties in obtaining reliable measurements of the relevant quantities in the hostile environment present in the accelerator as well as by the complex nonequilibrium nature of the working fluid. It is therefore desirable to establish the energy deposition ratio in a simpler geometry which retains the feature of high power self-field MPD accelerators.

The purpose of this thesis is to provide some insight into the energy deposition ratio in plasma accelerators using a parallel-plate accelerator geometry[2] which is shown schematically in Fig. 1-1. It consists of two sections: one formed by two short parallel plate electrodes separated and supported by insulated sidewalls followed by an insulating channel. The advantages of this geometry for this study are: a) By minimizing downstream expansion of the flow the initial energy deposition ratio is preserved, b) The electromagnetic fields upstream of the acceleration zone can be obtained through simple one-dimensional arguments while the flow field downstream of the acceleration zone is amenable to a one-dimensional treatment as well, and c) Assessment of the motional emf, whose ratio to resistive voltage drop is a valuable indication of the energy deposition ratio, becomes simplified as well.

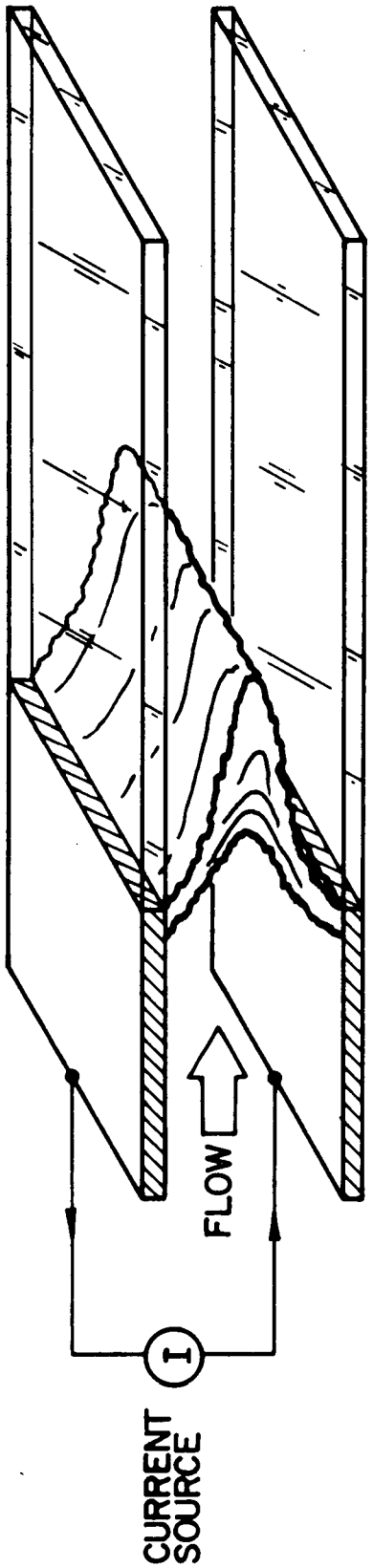

PARALLEL-PLATE ACCELERATOR

FIGURE 1-1
AP 25 4787

The accelerator system, described in detail in Chapter 3 is operated in the quasi-steady regime. Investigations of Eckbreth[2] and Clark[3] show that this regime of high power operation (~20 MW) is characterized by: a) Current pulses of 10^4 -10^5 A which insure vigorous electromagnetic acceleration of the flow by diffuse conduction of current densities of 10^7 - 10^8 A m^{-2}, and b) Pulses of sufficient duration (0.2 - 1.0 msec) which permit the discharge to achieve a steady state by allowing fresh gas from an external supply to flow into the discharge region. The power source and mass injection system designed for quasi-steady operation are described in Chapters 2 and 3 respectively.

The approach which is used to obtain the energy deposition ratio is based upon a "black box" or terminal analysis of the accelerator. This analysis, presented in detail in Chap. 5, is based upon measurements of the terminal properties of the accelerator such as current and voltage and measurement of the properties of the flow into and out of the acceleration region namely: electron densities, velocities and pressures on the wall of the channel. Details of these measurements are presented in Chap. 4. To obtain a self-consistent description of the flow, momentum and energy conservation arguments are used. The energy deposition ratio is then obtained as a ratio of streaming to thermal energy in the exhaust. The motional emf, calculated on the basis of the prevailing velocities and magnetic fields in the acceleration region, when compared to the resistive voltage drop also provides a valuable indication of this ratio.

CHAPTER 2

THE POWER SOURCE

2-1 INTRODUCTION

The operating regime outlined at the end of the previous chapter, namely current pulses with a magnitude of 10^4 - 10^5 A and a duration of 10^{-4} -10^{-2} sec, makes the design and construction of a power source for such pulses a substantial task. Moreover, for physically oriented laboratory studies, a premium is placed on precision and cleanliness of the current waveform as well as on flexibility of the power source in terms of the intensity and duration of the pulse delivered. All these requirements, in turn, conflict with obvious cost limitations and the desire to use standard components to shorten development time.

The most straightforward and versatile power source for laboratory studies is a pulse forming network derived from the so called "LC-Ladder" network. This type of network, when connected to a matched load, fulfills the requirements associated with cleanliness and precision of the pulse form and flexibility of the available current pulses.

Experience at this laboratory has shown that networks of this type are quite serviceable for experiments in plasma propulsion in general and in the quasi-steady regime in particular.[3,4,5] It was found, however, that the power sources utilized in the past suffered from two major drawbacks:

1. Inadequate total charge capacity: For currents in the interesting amplitude range of 10^4 - 10^5 A the power sources delivered pulses of marginal duration for quasi-steady experiments. Longer pulses, achieved at the expense of current amplitude, precluded vigorous electromagnetic acceleration and hampered experimental observations.

2. The severe mismatch between the power source and the accelerator produced a ringing waveform[3] that confined most of the experiments to the first half-cycle and seriously hampered time-integrated diagnostics due to spurious behavior of the accelerator during current reversal.

This section deals with the design and construction of an "LC-Ladder" pulse-forming network with a total capacity of 3.3 mF and a maximum stored charge of 26 kA-msec (26 C) when charged to 8 kV. This network is capable of delivering nonreversing current pulses with amplitudes up to 100 kA and durations up to 1 msec. (100 kA @ 0.26 msec or 26 kA @ 1 msec)

2-2 THE LC-LADDER NETWORK

An "LC-Ladder Network"[6] consisting of n shunt ideal capacitors and n series ideal inductors arranged in n sections is sketched below:

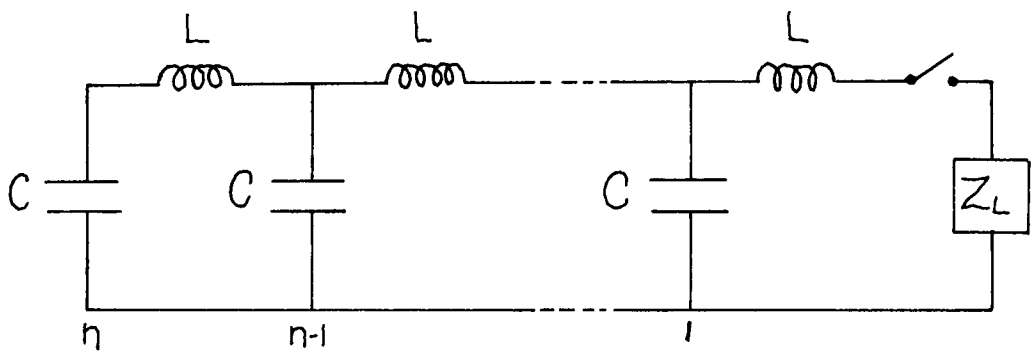

The characteristics of this network approximate the characteristics of an ideal transmission line with distributed capacitance and inductance in which the capacitance per unit length and inductance per unit length have been replaced by the capacitance and inductance of each section. The characteristic impedance Z_s of such transmission line is equal to:

$$Z_s = \left(\frac{L}{C}\right)^{1/2} \tag{2-1}$$

and the two way transit time of a signal along the line τ_p is given by:

$$\tau_p = 2n\,(LC)^{1/2} \tag{2-2}$$

This network, when charged to a voltage V_o and discharged into a load Z_L whose impedance is equal to Z_s, produces a single current pulse of magnitude:

$$I = \frac{V_o}{2Z_s} \tag{2-3}$$

and duration equal to τ_p.

The behavior of this network, however, differs from the behavior of the ideal distributed transmission line inasmuch as the pulse exhibits a finite risetime, some overshoot, some ripple, and a finite fall time as shown in Fig. 2-1a. The trace represents the calculated current for a pulse produced by a 5 section uniform network discharged into a matched load (i.e., $Z_L = Z_s$). A pulse delivered by an ideal distributed line would follow the dotted outline. Black[4] performed calculations for networks of 3,5,10, and 20 sections showing that the greater number of sections the more nearly the network approximates the ideal response. However, he found that the overshoot magnitude is independent of the number of sections remaining at about 9% of the current magnitude.

For design purposes, it is important to determine the current in each capacitor as a function of time. These partial currents observed experimentally[6] in a network of 4 sections like the one shown above are shown in Fig. 2-2a. The total current as a function of time resulting from the graphical addition of the traces is shown in Fig. 2-2b. It can be seen from the figure that the total current delivered by the network remains roughly constant and it is composed of an orderly succession of pulses delivered by each successive

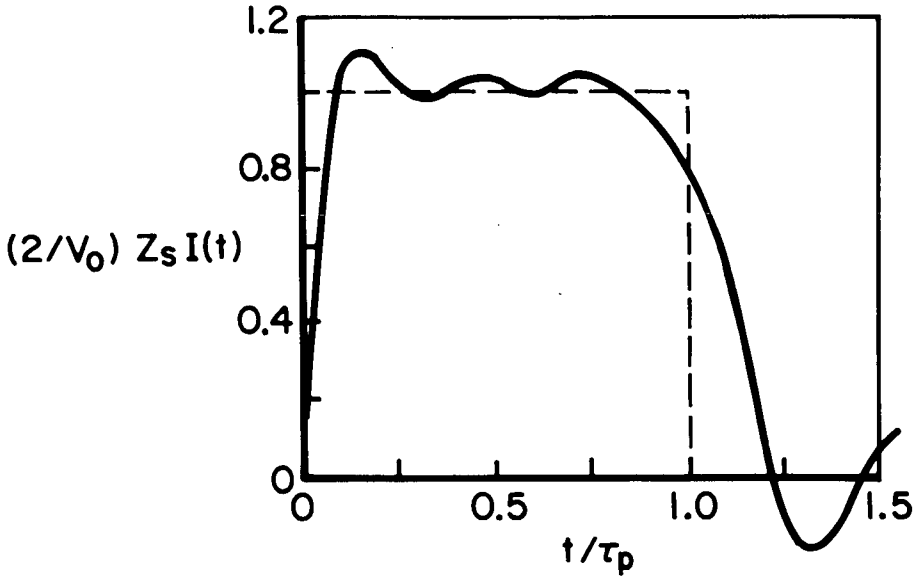

a) 5 SECTION NETWORK DISCHARGED INTO MATCHED LOAD

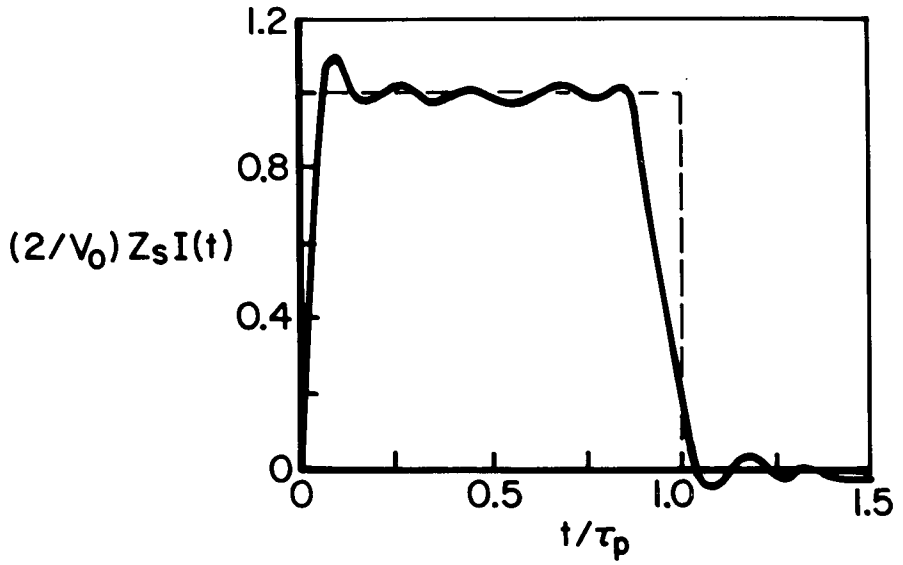

b) 5 SECTION NETWORK WITH MUTUAL INDUCTANCE DISCHARGED INTO MATCHED LOAD

CALCULATED CURRENT WAVEFORMS (REF. 6)

FIGURE 2-1

AP25 · 4754

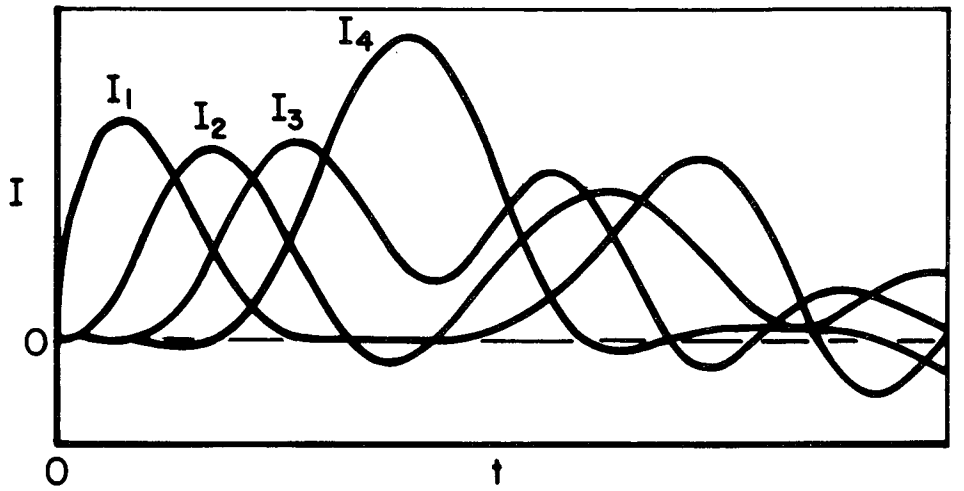

a) CURRENT IN EACH CAPACITOR, 4 ELEMENT NETWORK

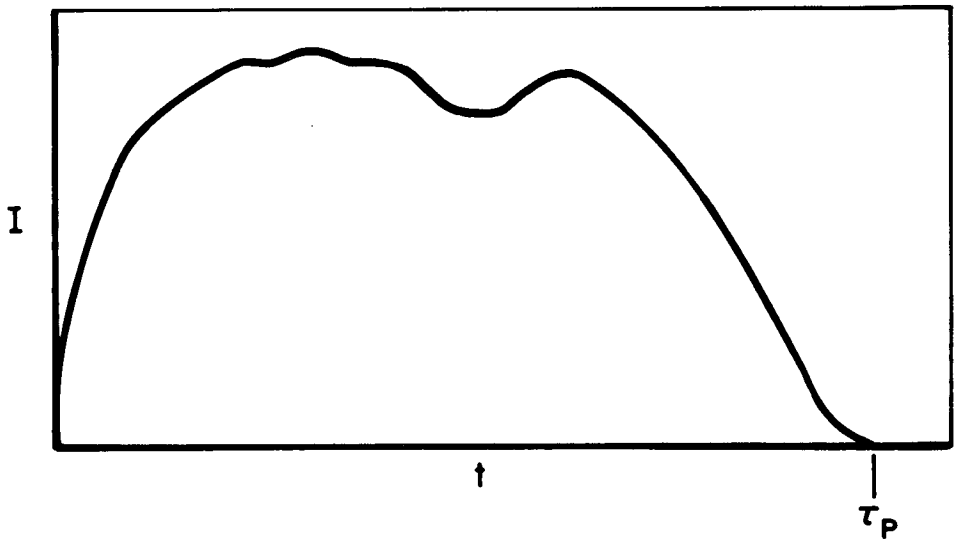

b) GRAPHICAL SUM OF CURRENTS

CURRENT IN 4 ELEMENT NETWORK (REF. 6)

FIGURE 2-2
AP25·4755

capacitor as the pulse propagates from the front to the tail end of the network, reflects at the back end, and propagates to the front end again. The current in each capacitor, except for the last one, resembles the positive portion of a sine wave while the current in the last capacitor results from the addition of two such sine waves. The frequency of these sine waves is given approximately by:

$$f = \frac{n}{2\tau_p} \tag{2-4}$$

and therefore the risetime τ_R of the pulse is equal to:

$$\tau_R = \frac{\tau_p}{2n} = (LC)^{1/2} \tag{2-5}$$

From the figure it can also be seen that the maximum current in each capacitor, an important design parameter, is at most 1/2 of the total current except for the last capacitor, in which the current is roughly equal to the total current.

The approach to the ideal behavior presented above is limited in practice by four factors related to the quality of the available capacitors and inductors and to the geometrical disposition of the elements in the network. The important effects which must be taken into account are:
Effect of:

1. Parasitic inductance associated with each capacitor.
2. Mutual inductance coupling between the series inductors.
3. Parasitic series resistance associated with the inductors.
4. Parasitic series resistance associated with the capacitors.

Since any capacitor has a parasitic inductance associated with its internal connections, the effect of this inductance on the shape of the pulse must be explored.

Black[4] has determined numerically the effects of the parasitic inductance βL with the following network

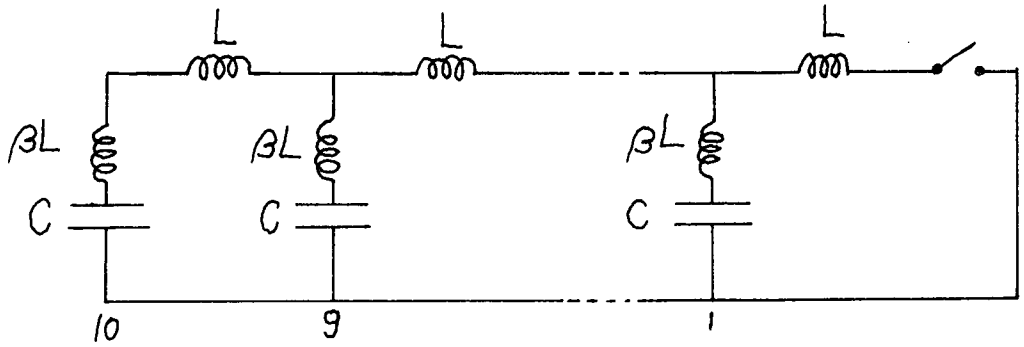

The short circuit currents, for different values of β, for a 10 section network like the one shown above are shown in Fig. 2-3. It is evident that as β increases the pulse shows an increased overshoot and ripple which sets a limit on β depending on how much of these effects can be tolerated. Conversely, through β, the parasitic inductance of the capacitor sets a practical limit on the minimum impedance of a network which can be realized with a given capacitor to provide a pulse of acceptable shape.

This limit, however, is less restrictive than it might be thought at first, since it applies to a single network only. It is possible to connect m networks in parallel such that:

$$Z_s\,(m) = \left(\frac{L/m}{mC}\right)^{1/2} = \frac{1}{m}\left(\frac{L}{C}\right)^{1/2} \qquad (2\text{-}6)$$

and

$$\beta(m) = \frac{\frac{\beta L}{m}}{\frac{L}{m}} = \beta \qquad (2\text{-}7)$$

Therefore, for a capacitor of given parasitic inductance, a parallel connection of networks allows the assembly of a power source with a Z_s lower than the minimum predicted for a single network. This technique has been used by Wilbur[5] and is also used in the power source designed for this experiment.

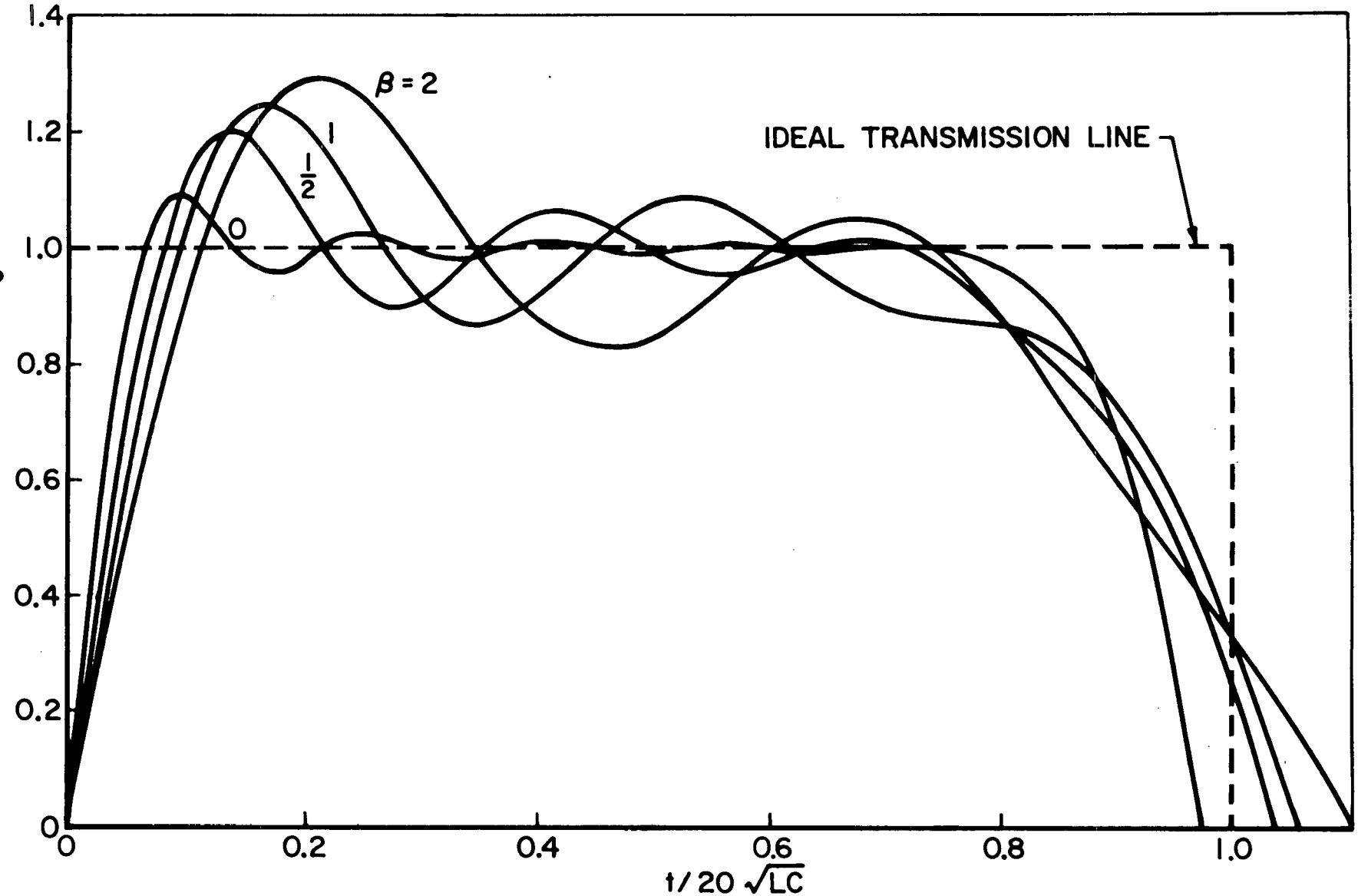

EFFECT OF PARASITIC INDUCTANCE ON CURRENT WAVEFORM (REF. 4)

FIGURE 2-3
AP25-4115

In the physical construction of an LC-Ladder network there always is some degree of mutual inductance coupling between adjacent inductors. To examine the effects of this coupling M, the following example will be considered:[6]

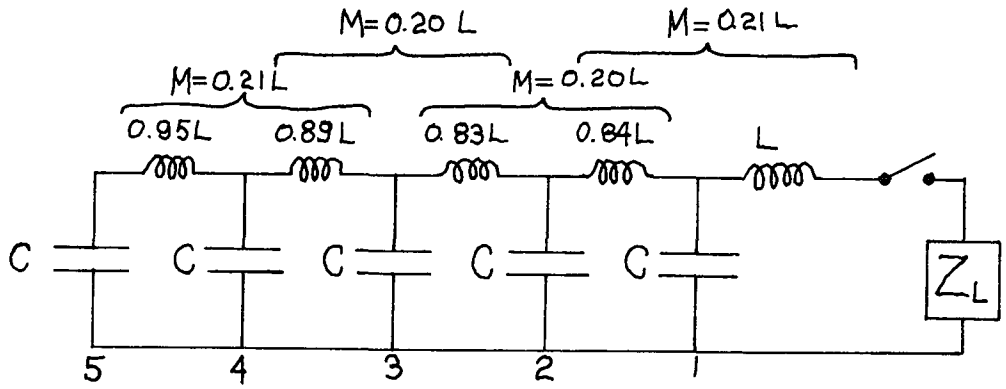

The current waveform delivered by this network, with a duration of 9.5 $(LC)^{\frac{1}{2}}$ into a load of impedance equal to $0.91(L/C)^{\frac{1}{2}}$, is shown in Fig. 2-1b. The risetime of the pulse as well as its overall shape shows an improvement with respect to the pulse shown in Fig. 2-1a.

It is interesting to note that the network shown above is the physically realizable form of the network:

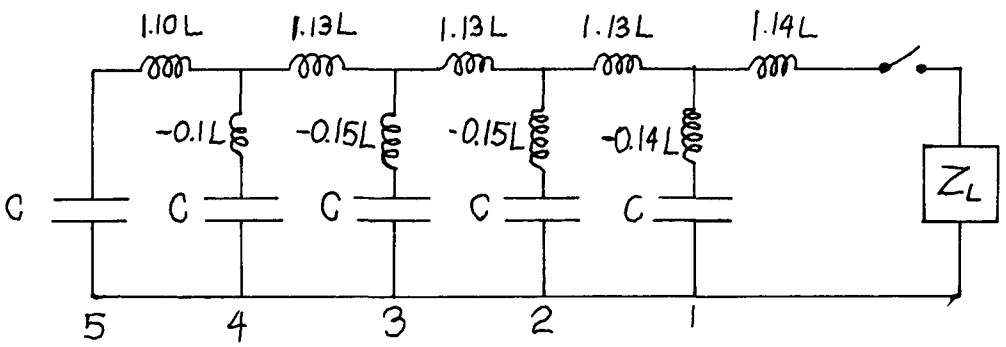

obtained by the methods of network synthesis. In this network, β is negative, suggesting that one way to alleviate the effects of the parasitic inductance associated with each capacitor is to couple the series inductors through mutual inductance. This effect can be achieved practically by winding the series inductors in a long continuous solenoid and connecting the shunt capacitors to equally spaced taps on the inductors.

All the networks presented so far are composed of non-dissipative elements. However, from a practical standpoint, every capacitor and inductor has some parasitic series resistance associated with it. Therefore, it is necessary to establish a criterion on the maximum value of parasitic resistance which can be tolerated without seriously degrading the magnitude and shape of the pulse. Since a survey of these effects is not available, some physical insight can be used to estimate their magnitude.

To estimate the effect of the parasitic resistance R_L, associated with the station to station inductance, the following network will be considered:

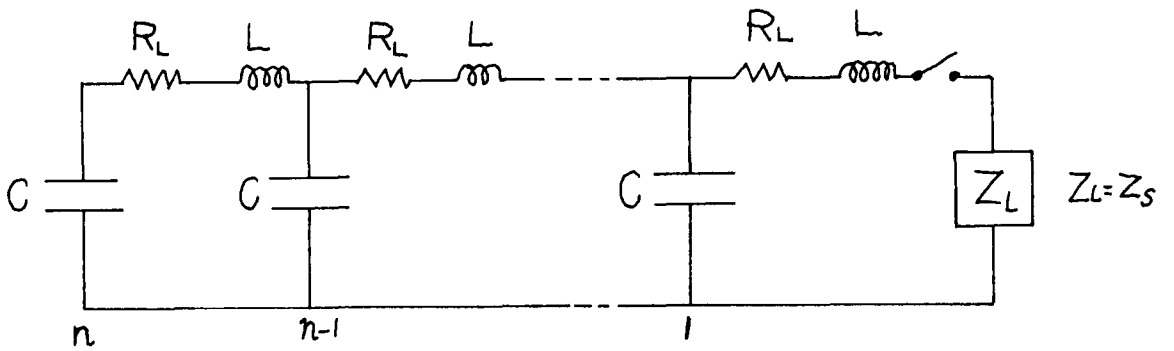

According to Fig. 2-2a, each capacitor delivers its charge in the form of a short current pulse. The total current is the sum of an orderly succession of these current pulses. Since the time derivatives of current and voltage in the elements ahead of a capacitor are zero once a capacitor has delivered its current pulse, the effective circuit for the nth section can be represented as:

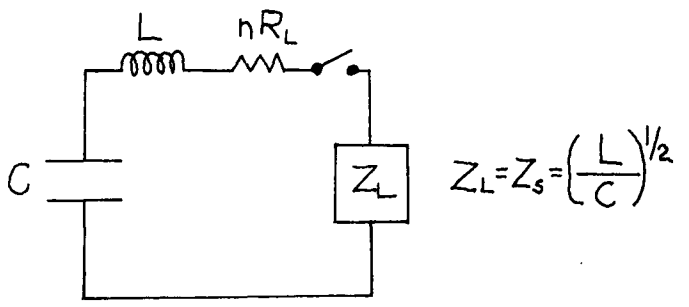

It is therefore required that:

$$nR_L \ll Z_s \tag{2-8}$$

or otherwise a significant voltage drop will occur across nR_L thereby lowering the total current through Z_s. The requirement expressed in Eq. 2-8, through the use of Eq. 2-1 and Eq. 2-2, yields the decay time:

$$\tau_D = \frac{2L}{R_L} \gg \tau_p \tag{2-9}$$

The form of τ_D is exactly the same as the form of the decay time for the current in an ordinary RLC network. Laboratory tests with a prototype network have shown that this criterion is indeed correct to within a factor of 2. The measured τ_D for a prototype network, with L = 600 nH and R_L = 1.12 mΩ, was found to be 0.7 msec while, for a network with the same L and R_L = 1.73 mΩ, was found to be 0.5 msec, showing quantitative agreement with the formula above. Measured values of τ_D are probably somewhat lower than the calculated ones because the formula above considers the losses on the series inductors only, while the measured decay time takes into account all losses.

The criterion presented above, sets a practical limit on the maximum number of stations or equivalently on the longest pulse with acceptable decay which can be obtained with a network with inductors of given parasitic resistance. It can also be shown that if a network of given impedance is desired, which is to be constructed with given capacitors, the problem presented by τ_D can be alleviated by the parallel connection of capacitors. To keep Z_s constant, from Eq. 2-1, L will have to be increased. However, for solenoidal inductors, L goes roughly as the length of the conductor squared while R_L goes linearly with the length of the conductor. Therefore τ_D increases with the increased

inductance and in that way the problem can be somewhat alleviated at the expense of risetime of the pulse.

A similar argument can be presented to estimate the effect of the series resistance associated with each capacitor. In this case the circuit becomes:

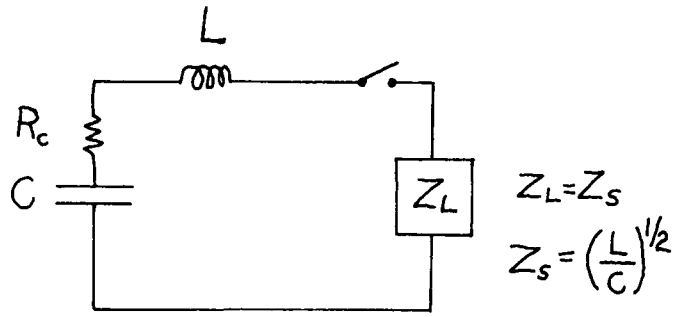

and the criterion in this case is:

$$R_c \ll Z_S \qquad (2\text{-}10)$$

2-3 DESIGN OF THE NETWORK

a) The Capacitors

To provide a current pulse of 30 kA and 1 msec duration, which lies in the middle of the range described in Sec. 2-1, formulae 2-1, 2-2, and 2-3 show that a total stored charge equal to $I\tau_p = 30$ C is required. For this purpose, 120 identical capacitors with a total capacity of 3.3×10^{-3} F, were obtained on a long term loan from the Plasma Physics Laboratory at Princeton University. These units, manufactured by the General Electric Co. in 1957 for the B-3 Stellarator, have the following characteristics:

Catalog Number	14F641
Nominal Capacitance	26.1 uF
Operating Voltage	10 kV

Their internal characteristics as supplied from the manufacturer are:

Dielectric stress at 10 kV: 1892 V/mil

Insulation: 8x .00066" Kraft paper impregnated with Pyranol, a non-flamable, non-explosive chlorinated dyphenyl

Foil: Aluminum with tab connections to the foil

Maximum Short Circuit Current: 52 KA for 25 discharges

Operating Current: 40A (6 msec discharge time)

Maximum Reverse Voltage: 10% of nominal voltage rating ($\sim$1 kV)

A photograph of one of the units is shown in Fig. 2-4.

To determine the capacitance of the units, 5 units were picked at random and their capacitance was measured with a General Radio Impedance Bridge Type GRC-1650A. The measurement was carried at 1 kHz. One determination of internal resistance was also performed on the bridge by measurement of the dissipation of the capacitor at 1 kHz. The inductance and the internal resistance of the capacitor were obtained by loading the capacitor to about 200 volts and discharging it through a short circuit across its terminals. The conductors were dressed in a configuration to minimize the stray inductance of the circuit since otherwise,the stray inductance could introduce a serious error in the measurement of the inductance of the capacitor. The low inductance switch, used to discharge the capacitor, was assembled from a large rat trap in which the mechanism was provided with indium contacts.[7] The trap was armed, the capacitor was charged, and then the trap was closed with a mechanical release. The current was monitored with a small Rogowsky coil[8] equipped with a passive R-C integrator and the integrator output was monitored on a Tektronix 555 oscilloscope. The current waveform is an exponentially damped sine wave. The

GE CAPACITOR UNIT CAT. # 14F641

FIGURE 2-4

AP25 P420

inductance of the circuit, L_C, was obtained from the measured frequency of the current in the circuit and the measured capacitance while the resistance R_C was obtained from the measured decay time of the current waveform and from the inductance determined as before. The values obtained are summarized below

$$C = (27.1 \pm 0.5)\,\mu F$$

$$L_C = (280 \pm 5)\,nH$$

$$R_C = (24 \pm 3)\,m\Omega \quad \text{(Decay time)}$$

$$R_C = (25 \pm 3)\,m\Omega \quad \text{(Dissipation @ 1 kHz)}$$

The value of R_C measured by both methods is likely to be high. In one case, it includes the resistance of the leads connecting the capacitor to the bridge while in the other it includes the resistance of the switch which is estimated to be around 4 mΩ. Therefore R_C, and L_C where a similar argument applies, are taken as upper bounds of the parasitic resistance and inductance of the capacitor.

b) <u>The Proposed Network</u>

Once the internal characteristics of the capacitor are established, it is possible to determine the feasibility of the proposed network. Again, utilizing Eqs. 2-1 and 2-2 for an "LC-Ladder" network with C=27.1 μF and n=120, the values of L and Z_s become:

$$L = 640\ nH$$

$$Z_S = 150\ m\Omega$$

It can be immediately seen that:

a. To obtain a current of 30 kA for 1 msec across a load equal to Z_s the network must be charged to V_o = 9 kV which falls within the rated voltage of the capacitors.

b. The peak current in each capacitor is on the order of 15 kA which is below the rated short circuit current.

c. The criterion: $\beta = L_c/_L = 0.4 < 1$ is satisfied and therefore the overshoot and ripple should be tolerable.

d. The criterion: $R_c/Z_o = 1/6 \ll 1$ is satisfied

e. The criterion $\tau_D = 2L/_{R_L} \gg \tau_p$ can be satisfied with a practical value of R_L. For $R_L = 0.13$ mΩ, $\tau_D = 10$ msec $= 10\tau_p$ and therefore $\frac{I(1\text{ msec})}{I(o)} = 0.9$ assuming an exponential decay of the pulse.

c) <u>The Inductors</u>

The design of the inductors was approached in a semi-empirical fashion. With the aid of the well known formula,[9] the inductance L of a long solenoid with large length to diameter ratio is

$$L = \frac{\mu_0 \pi n^2 d^2}{4\ell} \qquad (2\text{-}11)$$

where n is the total number of turns of the solenoid, d is its diameter, ℓ is its length and μ_o is the permittivity of free space. This formula, though not exact, allows an estimate of the required dimensions of a solenoid of given inductance. The dimensions are not unique and considerable freedom is allowed in the choice of number of turns and diameter. In this case, ℓ = 19.7 cm is fixed by the spacing between capacitors. It was found experimentally, with a prototype network, that a solenoid with n=3 and d=95 cm wound with 3.8 cm wide copper strip, provided the value sought for the inductance: L = 670 nH. The required mutual coupling is accomplished by winding the inductors in one continuous solenoid and, to reduce the number of connections, four inductors are wound from a strip of copper 3.66 m-long.

To make $R_L = 0.13\ m\Omega$ such that $\tau_D = 10$ msec, the thickness of the conductor is chosen to be 3.2 mm. A simple calculation indicates that this thickness corresponds approximately to the skin depth δ_s:

$$\delta_s = \left(\frac{\rho_E \tau_p}{\mu_0}\right)^{1/2} \tag{2-12}$$

where $\rho_E = 1.7 \times 10^{-6}\ \Omega$ -cm is the resistivity of copper and $\tau_p = 1$ msec is the length of the pulse. Therefore, the resistance R_L of the inductor cannot be significantly reduced by using a thicker conductor.

Another problem which arises in the design of circuit elements which carry large currents is the forces which are generated by the interaction of these currents with their own magnetic fields. While these forces can be successfully exploited for plasma acceleration, they introduce stresses in the system which have to be accounted for in the mechanical design of the network. For a solenoid, the forces act outward in the radial direction and inward in the axial direction. These forces can be calculated approximately through a virtual work approach with Eqn. 2-10. For a solenoid carrying a current I, the total electromagnetic energy in the system is:

$$Q = \frac{1}{2} L I^2 \tag{2-13}$$

For a virtual displacement $\delta \ell$,

$$\delta Q = F \delta \ell \tag{2-14}$$

and therefore, for the solenoid:

$$\delta Q = \frac{\pi \mu_0 n^2 I^2 d^2}{8 \ell^2} \delta \ell = F_x \delta \ell \tag{2-15}$$

For the dimensions above, and a current of 60 kA in case of a fault, the axial force is:

$$F_x = 4 \times 10^3 \, N$$

This force acts on all the inductors for a few microseconds as the current pulse propagates down the network and therefore does not present severe problems. However, the end inductors are subject to this force for the whole length of the pulse and therefore, the turns have to be braced to prevent their collapse. A similar analysis can be performed to obtain the radial force which appears as a hoop stress on the conductor. The total radial force on the conductor is given by:

$$F_r = \frac{\pi \mu_0 n^2 I^2 d}{2 \ell} \qquad (2\text{-}16)$$

and the radial force per unit circumference is:[10]

$$q = \frac{\mu_0 n I^2}{2 \ell} \qquad (2\text{-}17)$$

The stress σ on the conductor, is therefore:

$$\sigma = \frac{\mu_0 n I^2 d}{4 \ell a} \qquad (2\text{-}17)$$

where $a = 1.2 \times 10^{-4}$ m^2 is the cross section of the conductor. This number falls well within the elastic limits for copper.

d) <u>Capacitor Fuses</u>

Should an insulation breakdown occur in one of the capacitors, it is possible that a large fraction of the total energy stored in the system (130 kJ at 9 kV) could be released within the unit causing its metal case to rupture. Since the rupture of the case could damage adjacent units, as well as endanger life and property, it is necessary

to limit the amount of energy flow in a capacitor in case of a fault. Some protection can be afforded by connecting each capacitor to its respective inductor through a fuse[11] designed for this purpose.

When a fault occurs, the energy released in the capacitor is given by:

$$Q_p(t) = \int_0^t I^2 R_f \, dt' \qquad (2\text{-}19)$$

Typically, this fault will be an arc with a resistance $R_f = 10\ m\Omega$. Industry sources indicate that 10 kJ released into a capacitor casing are enough to rupture it and cause damage to adjacent units. Therefore, it is desirable to limit the energy flow to a value well below 10 kJ. For a safety factor of 5, $Q_f \leq 2$ kJ with $R_f = 10\ m\Omega$ will require:

$$\frac{Q_f}{R_f} = \int_0^{t_i} I^2 \, dt' \leq 2 \times 10^5\ A^2\,sec$$

On the other hand, operation of the power source requires from each capacitor, by Eqn. 2-4,

$$\int I^2 dt = \int_0^{\tau_p/n} 2\left(\frac{I}{2}\sin\frac{\pi n t}{\tau_p}\right)^2 dt = 2 \times 10^3\ A^2\,sec \qquad (2\text{-}20)$$

for $I = 3 \times 10^4$ A, $\tau_p = 10^{-3}$ sec and $n = 120$. Therefore, under the stated conditions the fuse can be designed to operate within comfortable margins.

The fuses used in this network are of the exploding wire type. They consist of a tinned copper wire surrounded by a 10 cm long piece of Tygon (R 3603) tubing with a bore of 1.6 mm and a wall thickness of 1.6 mm as well. This tube is placed inside a nylon tube (Polypenco Nylaflow) with a 4.8 mm ID and a 0.8 mm wall. The role of the Tygon tube is to prevent expansion of the metal after vaporization while

the role of the Nylon tube is to prevent the Tygon tubing from bursting. An explanation of the processes which are believed to occur in the fuse when the current is interrupted are discussed in detail in Ref. 12 .

The size of wire to be used was determined experimentally with a prototype network in which the fuse was used as a load. Some typical experimental results for the network loaded to 4.7 kV are shown in Fig. 2-5. The top trace in each oscillogram shows the voltage across the fuse while the bottom trace shows the current in the circuit. Figure 2-5a shows the current and voltage obtained with a 10 cm long, 2.5 cm wide, and 1.6 mm thick aluminum strip which is used as a reference in place of the fuse. The current is 30 kA and the duration of the current pulse is 160 μsec. The current shows the usual ringdown pattern due to the impedance mismatch between the source and the load. The voltage shows mainly the contributions due to the time rate of change of current in the circuit. The bottom oscillogram (Fig. 2-5b) shows the current across a fuse which is a 10 cm-long #16 AWG tinned copper wire. The behavior of current and voltage are essentially the same as for the aluminum strip up to 220 μsec at which time the voltage across the fuse begins to rise and the current starts to drop. The current is then effectively interrupted at t_i = 520 μsec. Examination of the fuse after the experiment showed that the wire had completely melted and vaporized and the whole area around the fuse supports was coated with a thin copper plating. The same piece of tubing was used for several tests and remained intact throughout the tests. The results for two sizes of tinned copper wire are shown below:

WIRE (AWG)	DIAMETER (mm)	$\int_0^{t_i} I^2 dt$ (10^5 A^2 sec)
16	1.29	2.1 ± 0.2
18	1.05	0.75 ± 0.1

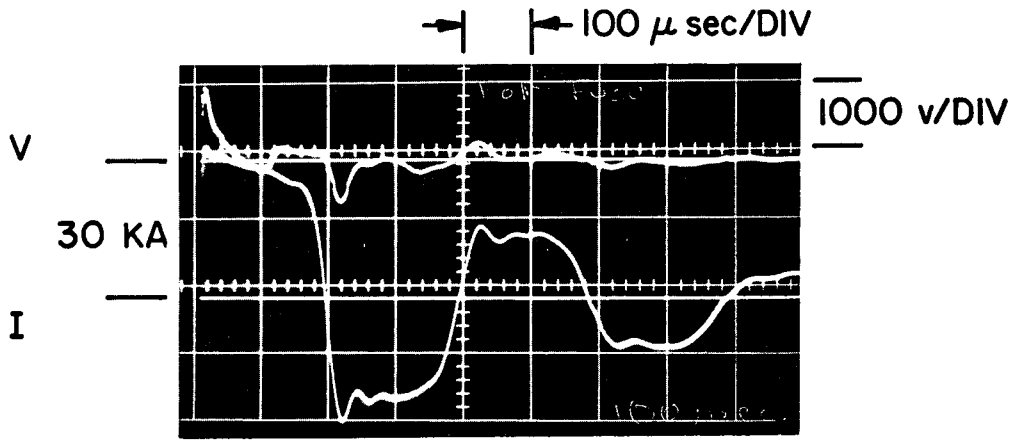

a) ALUMINUM STRIP

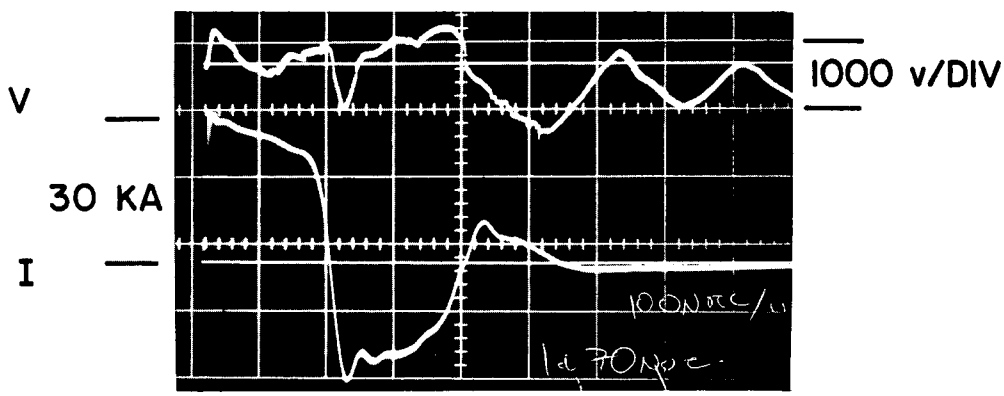

b) FUSE

VOLTAGE AND CURRENT IN FUSE TEST

FIGURE 2-5
AP 25 P 257

These results were obtained by graphical integration. It was therefore decided to use #16 AWG tinned copper wire since the added resistance (0.13 mΩ) is negligible and the added inductance (100 nH) did not visibly affect the shape of the pulse in a prototype network.

Later experience with the power source,has shown that the weakest point of the capacitor is its terminal insulator and bushing. Eight failures have been experienced in 18 months of operation ($\sim$ 3800 pulses). All eight have resulted in a broken insulator bushing and terminal and in 7 of them the fuse as well as the capacitor case was found intact. In one failure, the fuse completely vaporized, the case was swollen and the terminal was imbedded in a plasterboard wall. This indicates that the fuse had limited the amount of energy deposited within the case preventing its rupture.

e) Assembly of the Network

The schematic diagram of one section of the network which summarizes all the electrical parameters presented in the previous section is shown in Fig. 2-6. The construction details of a typical section are shown in Fig. 2-7 which presents a front view and a side view of the section. The figure shows the following elements:

1. Capacitor
2. Capacitor terminals and insulator bushing
3. Inductor
4. Fuse
5. Ground Return Conductor (Copper, 0.8 mm thick)
6. 2 cm Plywood
7. Spacer (For clearance between capacitor and rack)
8. Inductor Support Mounting (Aluminum)
9. Inductor Support (Phenolic)
10. Polyethylene insulation

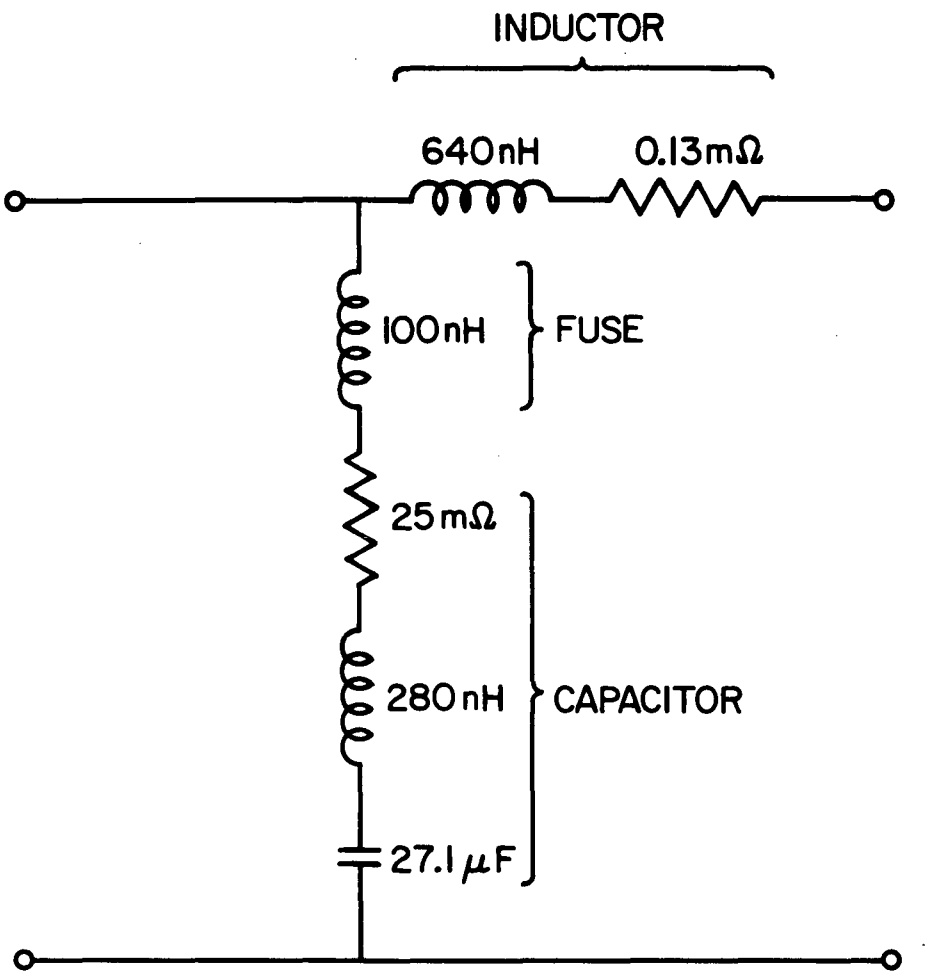

SCHEMATIC OF NETWORK SECTION

FIGURE 2-6
AP25 · 4752

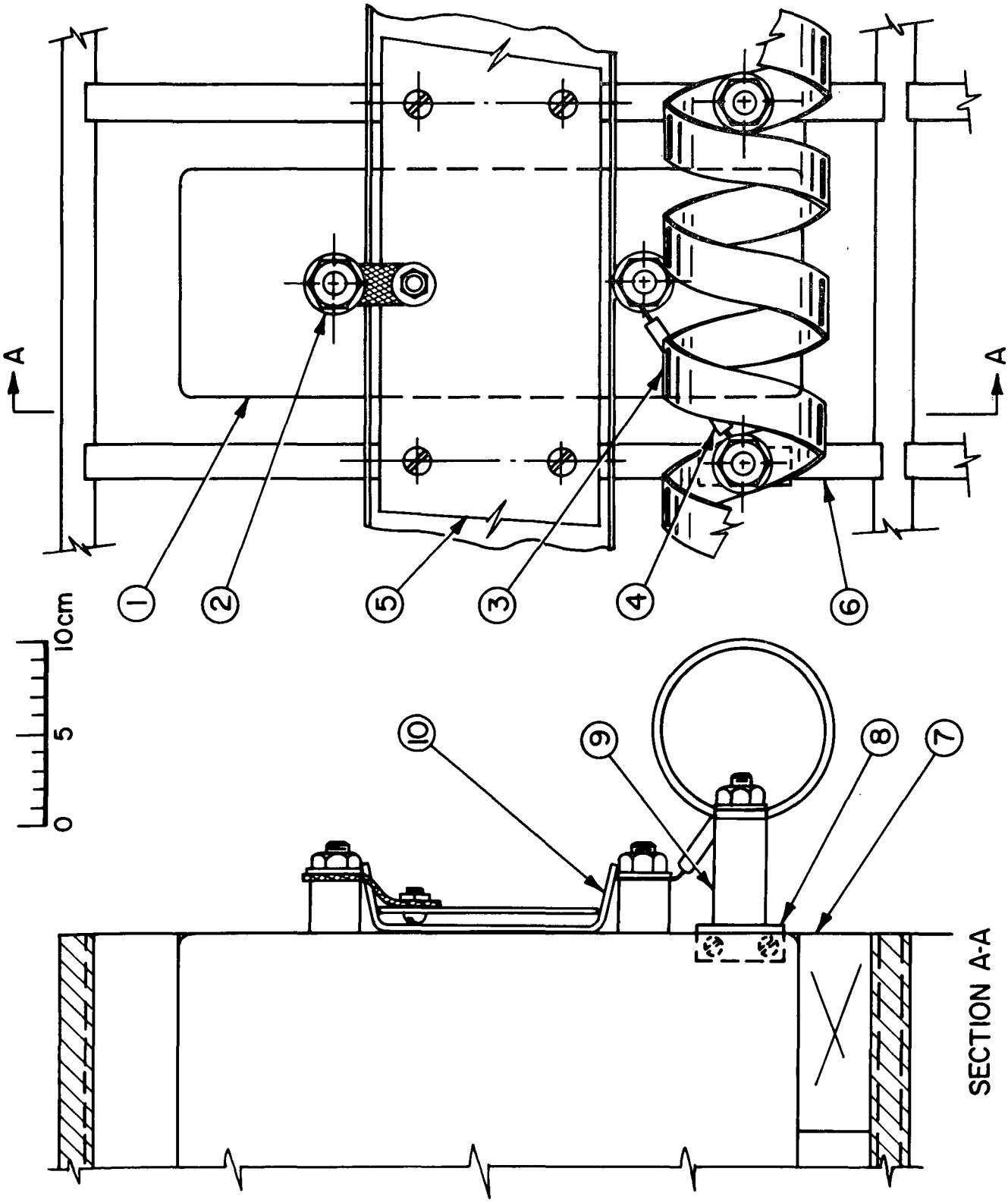

DIAGRAM OF NETWORK SECTION
(LEGEND ON PAGE 26)

FIGURE 2-7
AP25 4751

f) The Ballast Resistor

Since the network is required to deliver a nonreversing current pulse, some means must be provided to adjust the impedance of the load Z_L to prevent a voltage reversal on the network upon reflection of the current pulse at the end of the network. Since the impedance of plasma accelerators in the regime of interest is of the order of a few milliohms, it is necessary to connect a ballast resistor in series with the accelerator to provide the proper value of Z_L. This requirement, first presented in Sec. 2-1, acquires a new dimension in the light of the capacitor characteristics presented in Sec. 2-3a. The electrical stress within the dielectric of these capacitors, which operate with an electric field of 7.5×10^4 V mm^{-1} at 10 kV, is significantly higher than the generally accepted field for capacitors of this type which is roughly $4\text{-}5 \times 10^4$ V mm^{-1}. Therefore, repeated voltage reversals across such a highly stressed dielectric would seriously compromise the life of the units, and the prevention of voltage reversal becomes an economic necessity as well.

For this network, the required electrical characteristics for the ballast resistor R_B which will make the load impedance Z_L equal to the source impedance $Z_S = 150$ mΩ are approximately:

$$R_B = 140 \text{ m}\Omega$$

$$L_R = 200 \text{ nH}$$

since the impedance and inductance of the accelerator and connections are expected to be about 10 mΩ and 500 nH respectively, and the risetime of the pulse requires a front end inductor L = 700 nH. The resistor must be able to dissipate and instantaneous power $\dot{Q}$ equal to:

$$\dot{Q} = R_B I^2 \qquad (2\text{-}21)$$

which for a resistance of 140 mΩ and a current of 3×10^4 A is equal to 1.3×10^8 W. The total energy Q dissipated per pulse, on the other hand is:

$$Q = R_B I^2 \tau_p \qquad (2\text{-}22)$$

which in this case amounts to 1.3×10^5 J.

To obtain a resistance of this magnitude, capable of dissipating the required instantaneous power $\dot{Q}$ and total energy Q with a low inductance L, a large number ($\sim$100) of commercially available carborundum resistors would be required, at a prohibitive cost. On the other hand, an electrolytic resistor can ideally satisfy the above requirements.[13] The large heat capacity of the electrolyte in the resistor permits dissipation of both the instantaneous power and the total energy of the pulse. It can be built in a low inductance geometry and its resistance can be easily adjusted by changes in the concentration of the electrolyte. The resistors chosen for this network consist of copper electrodes immersed in an aqueous solution of cupric sulfate. The cathode reaction for this cell is:

$$Cu^{++} \longrightarrow Cu - 2e^-$$

while the anode reaction is the opposite one:

$$Cu \longrightarrow Cu^{++} + 2e^-$$

Therefore, copper is transferred from anode to cathode during operation. The advantages of this cell are:

1. The cell produces no net emf and therefore there is no electrolytic action when the terminals are in short circuit.
2. The cell is reversible; therefore, the two electrodes can be restored by passing a current in the reverse direction.

3. It does not produce explosive gases as a by-product of electrolysis and the electrolyte is not highly corrosive and will not produce burns.
4. It is economical to build and easy to maintain since it only needs periodic addition of distilled water.

The design of the resistor is dictated by the maximum temperature rise which can be tolerated during a pulse. Since the conductivity of an aqueous solution exhibits a strong temperature dependence, it is preferable to maintain the temperature rise during a pulse as small as possible. It is also necessary to maintain a given 2" minimum electrode separation to prevent a flashover over the surface of the electrolyte; baffles, can be used to relieve this problem. The temperature rise of a volume V of electrolyte is given by:

$$\Delta T = \frac{I^2 R_B \tau_p}{C \rho V} = \frac{Q}{C \rho V} \qquad (2\text{-}23)$$

where ρ is the density of the electrolyte and C is its heat capacity. For $Q = 1.3 \times 10^5$ J and $\Delta T = 3^\circ C$ the volume V is 10 liters. If a plate separation $d = 5$ cm and a plate area of $0.2 m^2$ is adopted, the resistivity ρ_E of the electrolyte can be obtained approximately from:

$$R_B = \frac{\rho_E d}{A} \qquad (2\text{-}24)$$

For the dimensions above, the required resistivity is

$$\rho_E = 56\ \Omega\ cm$$

The resistivity of the cupric sulfate solution as a function of concentration was determined experimentally by measuring the resistance of a cell formed by a Plexiglas

cylinder with an internal diameter of 3.74 cm and a length of 11.9 cm, closed at both ends by copper electrodes. Two small holes were provided to fill the cylinder and to monitor the temperature of the solution. A direct current was passed through the cell (100 mA for 2 min.) to expose a fresh electrode surface and its resistance was then measured with a GRC 1650-A Impedance Bridge at 1 kHz. It was found that without the direct current conditioning the resistance measurements on the cell were erratic and varied with time. The resistivity of the electrolyte,obtained from the measured resistance and the measured dimensions of the cell is shown in Fig. 2-8 which displays the resistivity of aqueous cupric sulfate solution as a function of concentration at 23.5°C and at 1 kHz. From the figure, for example, $\rho_E = 56\,\Omega$ cm corresponds to a 0.28 molar solution.

The final configuration for the resistor is shown in Fig. 2-9. The copper electrodes,shown on the left,consist of copper sheet, 61 cm.-long, 33 cm-wide, and 0.8 mm thick, Nylon separators keep the distance between the plates at 5 cm. Two Plexiglas baffles,mounted on the support for the plates,are immersed in the electrolyte to a depth of 10 cm. These baffles are designed to prevent a breakdown between the two plates directly across the surface of the electrolyte. The electrodes are immersed in a .58 molar solution with $\rho_E = 33\,\Omega$ cm,contained in the 61 liter vat shown on the right. The overall volume of solution should keep the temperature rise of the electrolyte well below the 3°C per pulse mentioned before. The inductance of this configuration is estimated at 40 nH.

g) <u>Accelerator Connections</u>

Coaxial cables were chosen to provide a flexible low inductance connection to the accelerator. The application of coaxial cables to pulsed high current systems is discussed in detail in Ref. 14 . The main design considerations

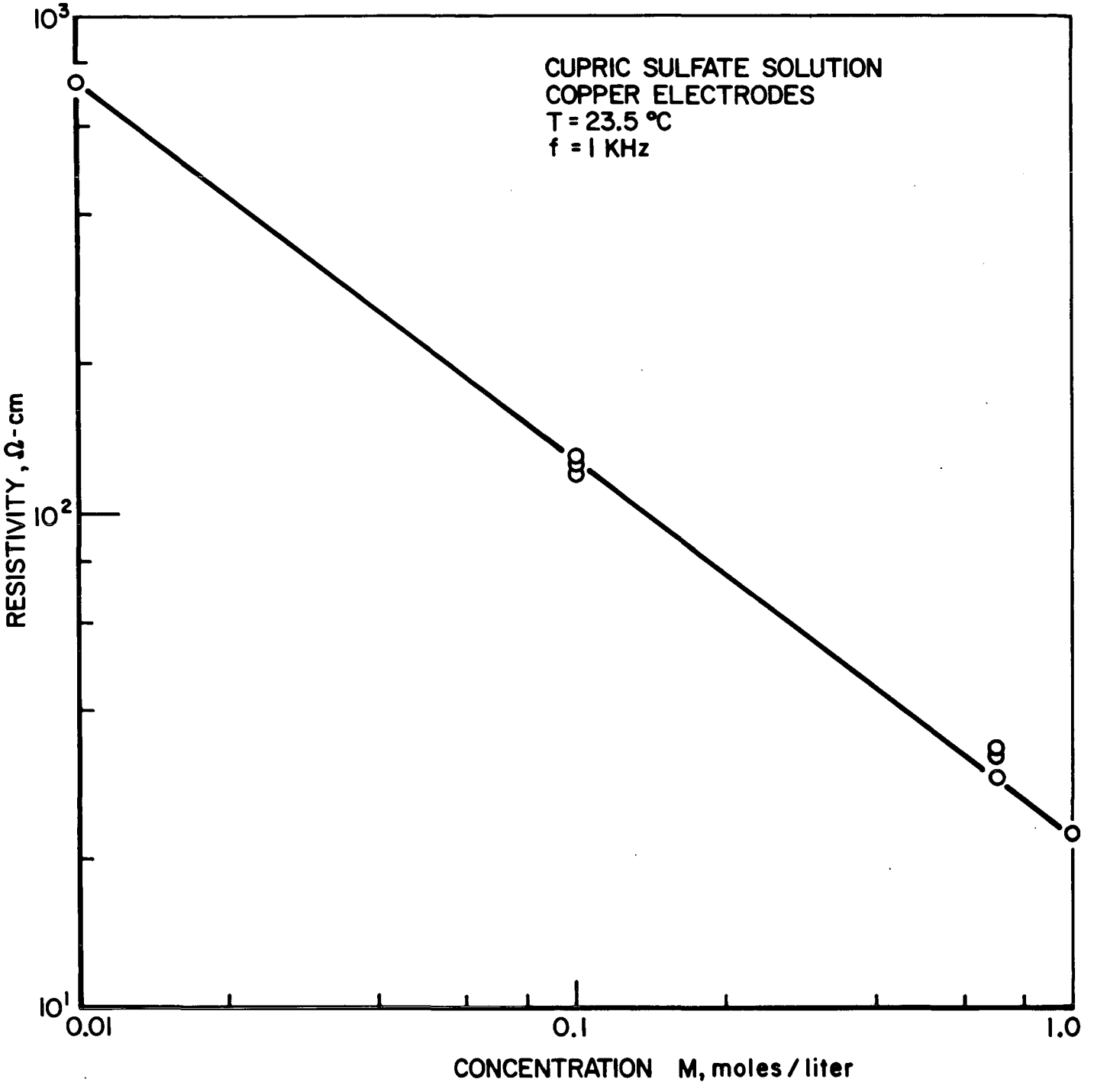

RESISTIVITY OF CUPRIC SULFATE SOLUTION
AS A FUNCTION OF CONCENTRATION

FIGURE 2-8
AP25-4753

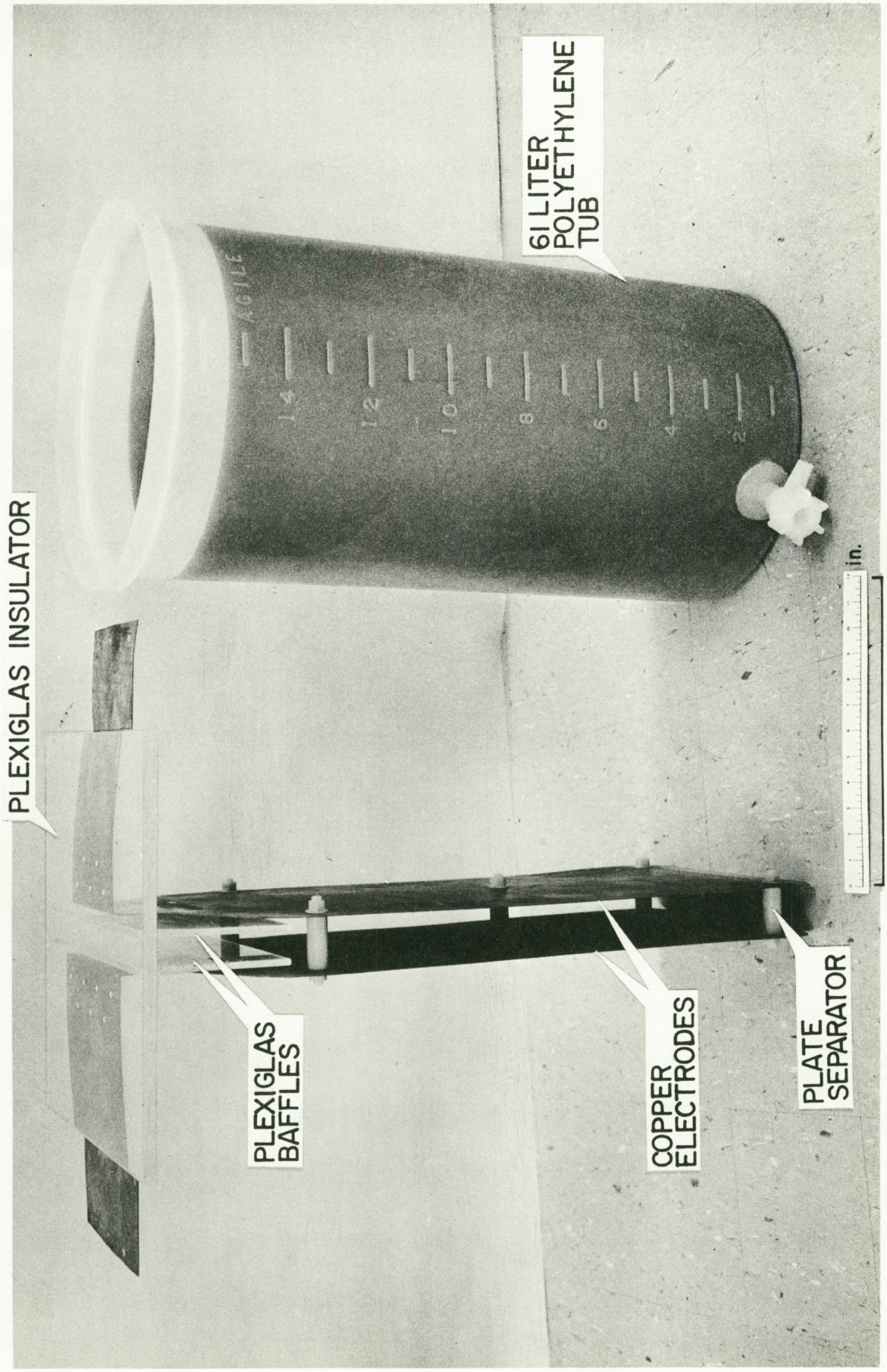

VIEW OF ELECTROLYTIC RESISTOR

FIGURE 2-9

AP 25 P418

for this connection are the maximum operating voltage, the temperature rise of the conductor per pulse which must be kept well below the melting point of the Polyethylene insulation, and the maximum resistance and inductance which can be tolerated in this connection. The 11 m-long connection between the power source and the accelerator consists of five RG/14A-U coaxial cables with a total resistance of approximately 10 mΩ and a total inductance of 680 nH. The resistance is quite tolerable and the cables contribute to the inductance for the first section of the network.

h) The Charging Supply

The charging supply, manufactured by Del Electronics Inc., is capable of delivering 5 kW of DC power at 10 kV. A smaller size supply would take longer than 1 minute to charge the bank to full voltage with deleterious effects on the capacitors since all components would be subject to a high voltage for a long time. The circuit is a three phase voltage doubler developed by Prof. N. W. Mather at Princeton University and described in detail in Ref. 15 . Since the initial charging rate (1.8 A) in this type of supply is limited by a series capacitor, the network is charged by connecting the power supply directly to it and disconnecting it when the voltage in the network reaches the desired value. A 1000 Ω bleeder resistor,of the electrolytic type described before,is provided to discharge the network safely in case of an abort with a time constant RC of 3 seconds.

i) Performance of the Power Source

A photograph of the complete power source is shown in Fig. 2-10 which displays the pulse-forming network, the ballast resistors, the bleeder resistor and the charging supply. A large degree of flexibility is provided by subdividing the 120-section network into 4 units of 30 sections

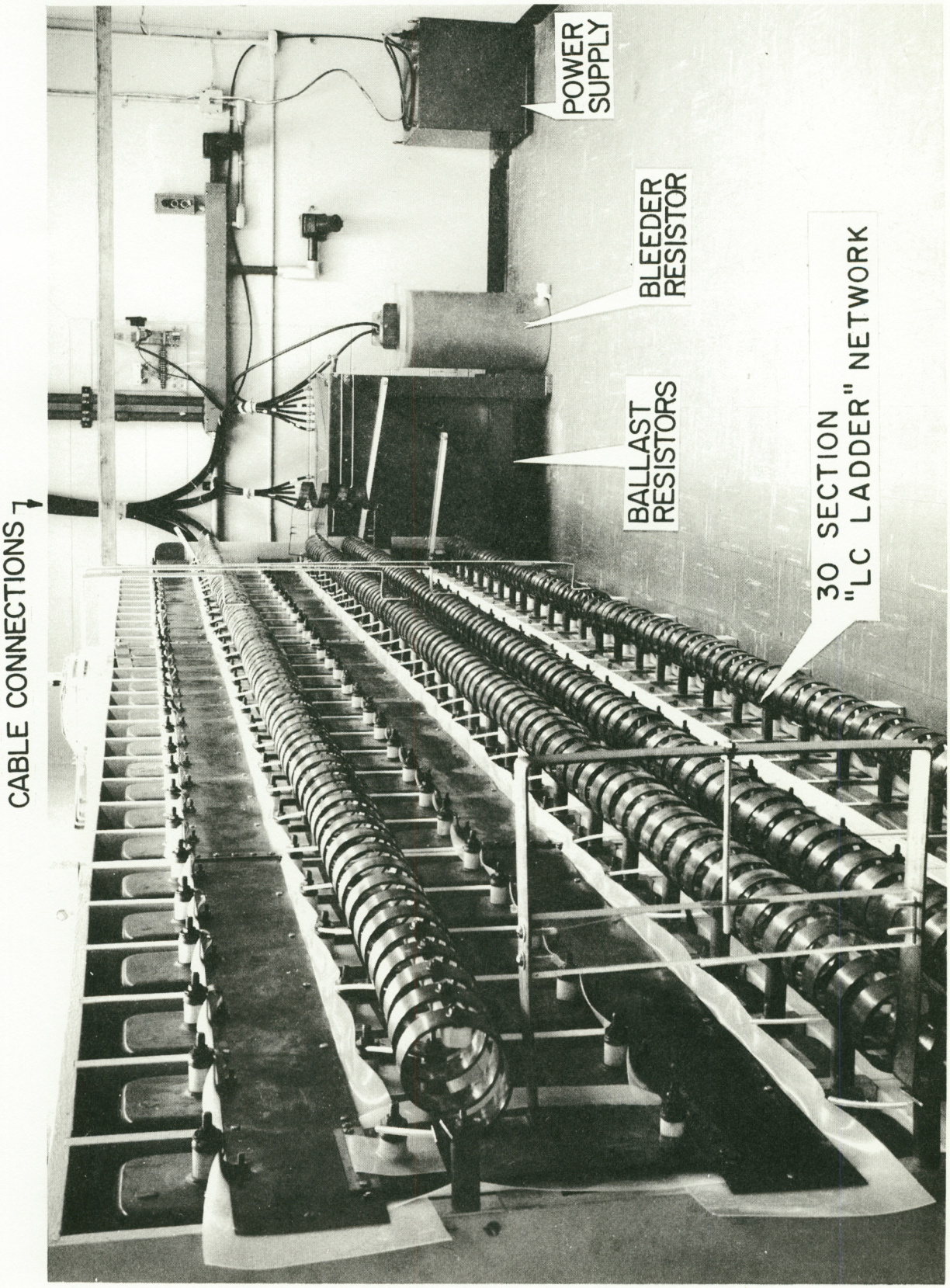

VIEW OF POWER SOURCE

FIGURE 2-10
AP25 P 419

each as shown in the photograph. These units can be connected in three configurations as shown in Fig. 2-11: a) front to end connection which provides a 1 msec pulse, b) parallel connection of two units connected front to end which provides a current pulse of 1/2 msec with twice the current and c) parallel connection of the units which provides a pulse of 1/4 msec with four times the current. To provide the proper load impedance for the three configurations, each unit is equipped with its own ballast resistor and its own set of cable connections to the accelerator. Therefore, one resistor and one set of cables are used for configuration (a), two resistors and two sets of cables for configuration (b), four resistors and four sets of cables for configuration (c). The subdivision of the network into four units,also allows operation of the accelerator at a future date in a repetitive-pulse mode by the installation of a high current switch in each of the units.

The signatures of the current pulses delivered to a coaxial MPD accelerator[16] and switch by the three network configurations are shown in Fig. 2-12. The current signatures are obtained by passive integration of the signal from a Rogowsky coil[8] with a time constant RC = 105 msec to preserve fidelity in the reproduction of the current pulse. The magnitude of the three current pulses shown in the figure, obtained with a charging voltage V_o = 4.6 kV, and other pertinent data on the circuit are summarized below:

Configuration	V_o (kV)	I (kA)	τ_p (msec)	Z_s (mΩ)	R_B (mΩ)	Z_T (mΩ)	$Z_T-R_B-Z_s$ (mΩ)
(a)	4.6	17	.84	150	104	270	16
(b)	4.6	32	.42	75	52	144	17
(c)	4.6	61	.21	37.5	26	77	14

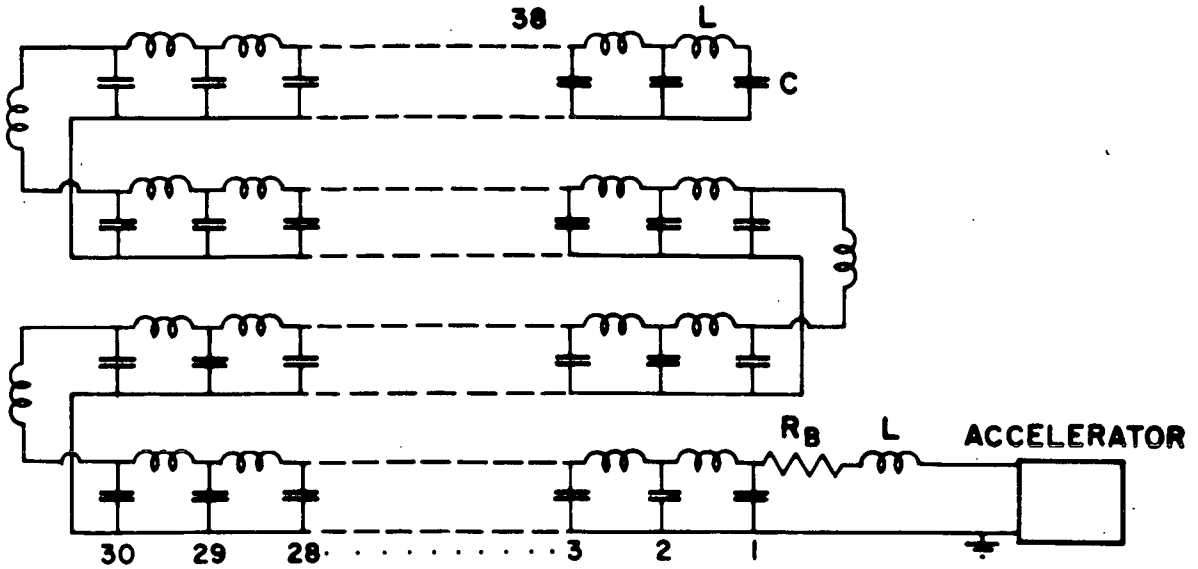

a) FRONT TO END CONNECTION OF 4 UNITS

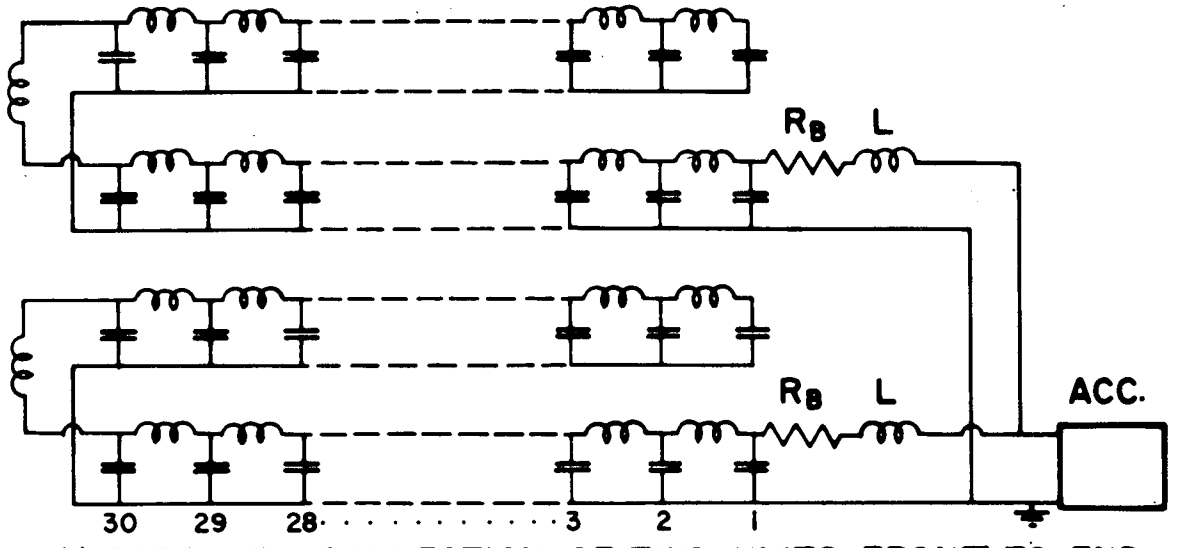

b) PARALLEL CONNECTION OF TWO UNITS FRONT TO END

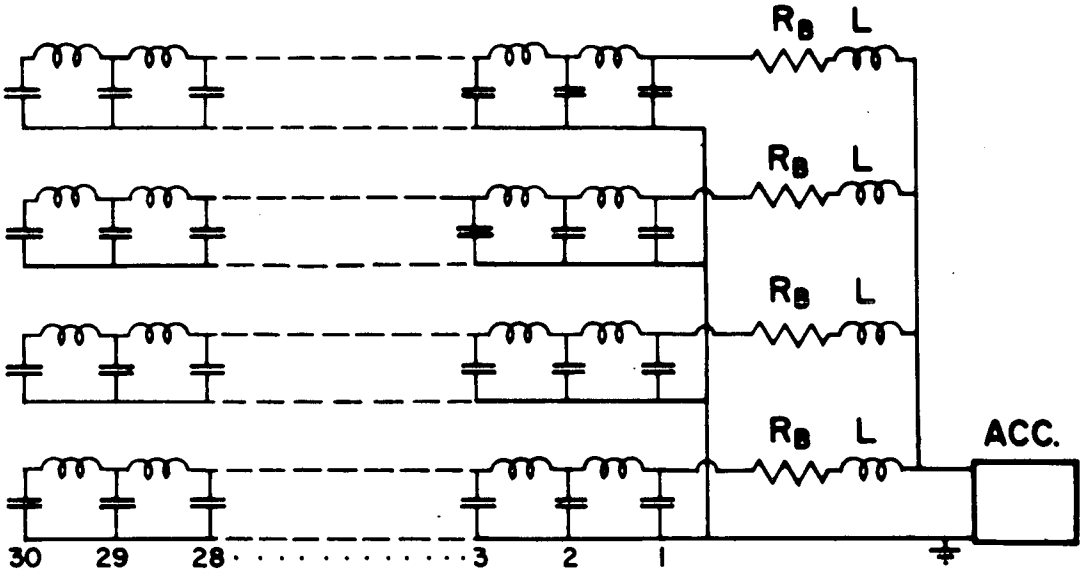

c) PARALLEL CONNECTION OF 4 UNITS

NETWORK CONFIGURATIONS
FIGURE 2-11
AP25 4788

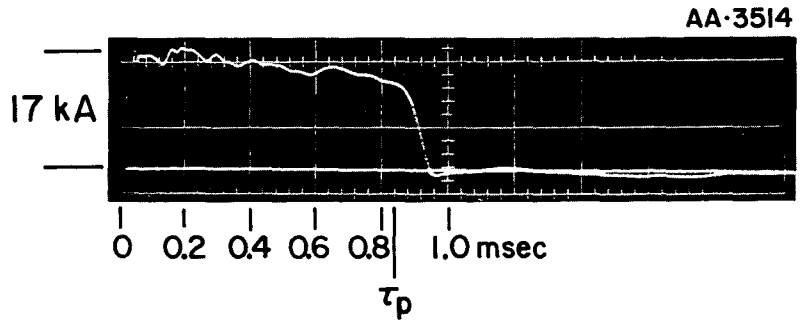

a) FRONT TO END CONNECTION

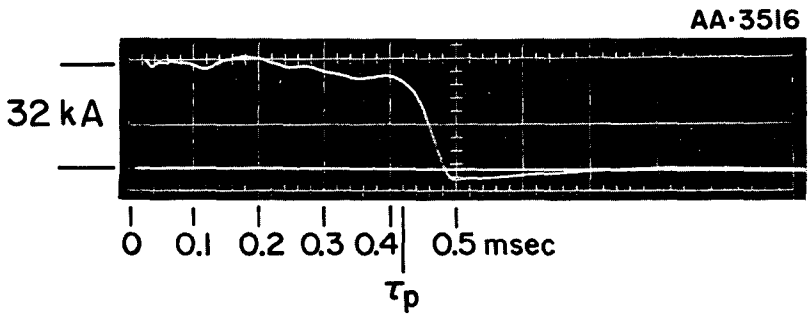

b) PARALLEL CONNECTION OF 2 UNITS FRONT TO END

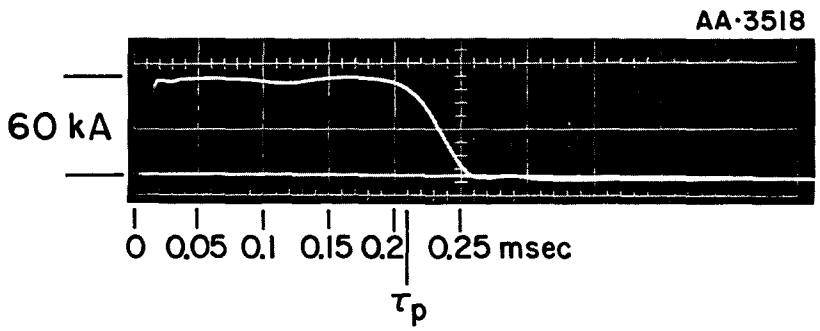

c) PARALLEL CONNECTION OF 4 UNITS

CURRENT PULSES, V_0 = 4.6 kV

FIGURE 2-12
AP25·P·404

The total impedance of the system Z_T, which includes the impedance of the network, the ballast resistor, the connections and the accelerator is obtained by dividing the loading voltage V_o by the current I in the circuit. The network impedance Z_s is obtained on the basis of the inductance and capacitance of each section, (Sec. 2-3b) and the resistance of the ballast resistor R_B, is obtained by the simultaneous measurement of the current in the circuit and the voltage across the resistor as shown in Fig. 2-13a. The column Z_T-R_B-Z_s denotes the impedance of the accelerator, connections and switch as obtained form the measurements above. A 5% accuracy is estimated on the above measurements. The current for configuration (a) is about 10% higher than the design current of 15.4 kA at 46 kV, (30 kA at 9 kV), and the pulse duration τ_p = 0.84 msec is shorter than the 1 msec design duration.

Despite the apparent impedance mismatch, (Z_s = 150 mΩ, Z_L = 120 mΩ), the current reversal (Fig. 2-12) for the three pulses is either minimal or nonexistent. This is probably due to the attenuation of the current pulse due to the series resistance R_L of the inductors. The current pulses delivered by the three configurations (Fig. 2-12) are tolerably smooth. The ripple in the pulses delivered by configurations (a) and (b) is introduced by the inductors which connect the four units to form these configurations. The ripple arises from reflections in the network which appear every time the electromagnetic pulse goes around a corner. The ripple is most severe for the pulse delivered by configuration (a) which goes around 6 corners in its two-way transit and the ripple is nonexistent for the pulse delivered by configuration (c) which goes around none.

The decay of the current pulse is clearly evident in Fig. 2-13b which shows the pulse delivered by configuration

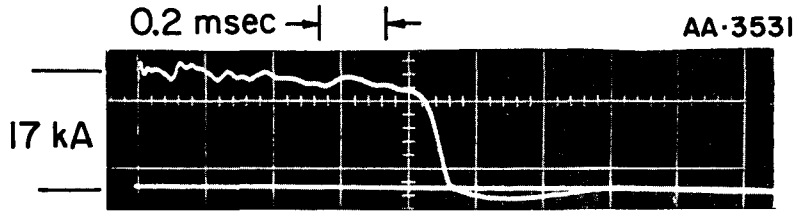

a) CURRENT

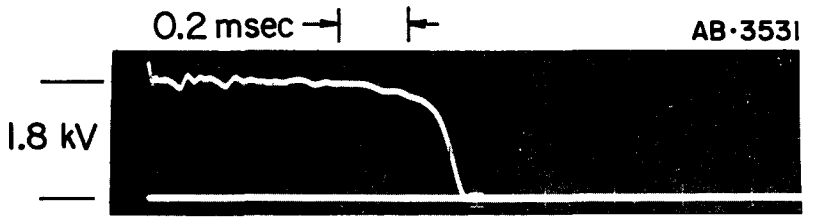

b) VOLTAGE

a) CURRENT AND VOLTAGE ACROSS $R_B, V_0 = 4.6$ kV

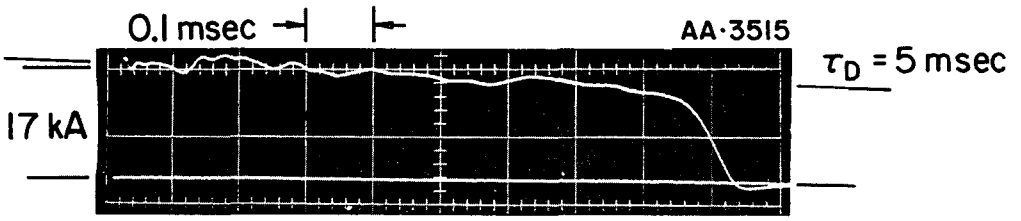

b) DECAY OF CURRENT PULSE

FIGURE 2-13
AP25·P·405

(a) on an expanded time scale. The decay time τ_D, (Eqn. 2-9) measured from the oscillogram, is 5 msec which is in quantitative agreement with the value predicted by Eqn. 2-9 for a section inductance L = 670 nH and an inductor resistance R_L = 0.13 mΩ. (2L/R = 10 msec)

CHAPTER 3

THE PARALLEL-PLATE ACCELERATOR SYSTEM

3-1 INTRODUCTION

The parallel-plate accelerator system utilized in these experiments is composed of an accelerator channel, a shock tube mass injection system and a switch which connects the power source to the accelerator. These components, which are shown in the schematic of the system presented in Fig. 3-1 and in the photograph of the apparatus in Fig. 3-2, will be described in detail in the sections that follow.

3-2 THE ACCELERATOR CHANNEL

The accelerator channel[2], shown schematically in Fig. 3-1, is 15.2 cm-wide, 5.1 cm-high and 1.22 m-long. It is formed by two 13.8 cm-long aluminum electrodes which occupy the 15.2 cm-width of the channel followed by a Nylon insulating section 109 cm-long. The sidewalls, which also form the supporting structure of the channel, are made of Plexiglas. The choice of dimensions, which has been discussed in detail in Ref. [2], is dictated by the requirement that the channel height be small in comparison with its width to alleviate two-dimensional effects. The 15.2 cm-width of the channel is chosen to enable the discharge to maintain diffuse conduction of current densities of the order of 10^6-10^7 A m^{-2} with currents of 10^4 -10^{-5} A, which is an essential feature of quasi-steady MPD accelerators.

The choice of Nylon and Plexiglas is based upon their ease of fabrication and low initial cost coupled with their excellent insulating properties. The Plexiglas walls, also allow unhindered photographic observation of the discharge. These advantages are somewhat offset, however, by the comparatively high vapor pressure of these materials

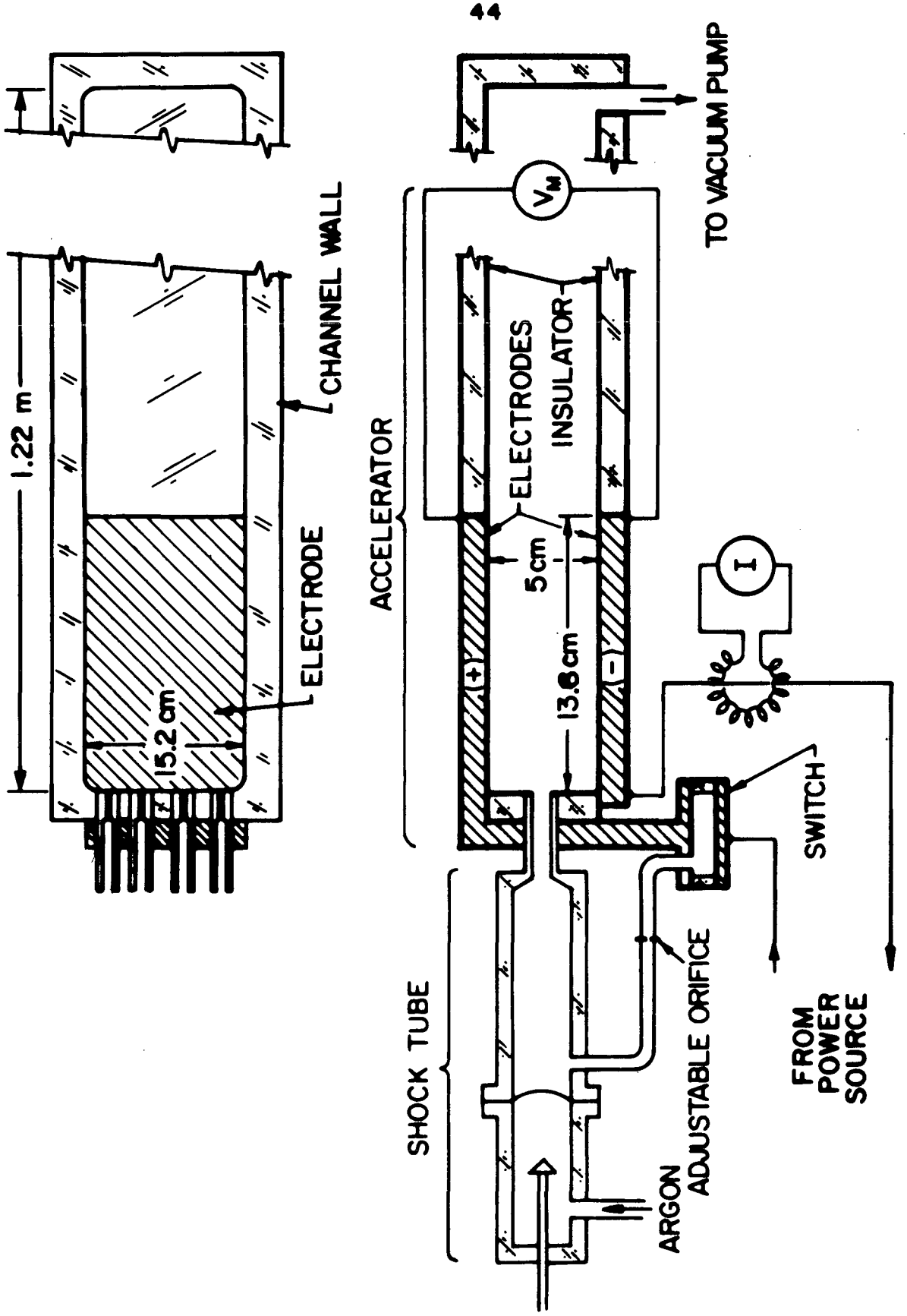

SCHEMATIC OF PARALLEL PLATE ACCELERATOR SYSTEM

FIGURE 3-1

AP25 4769

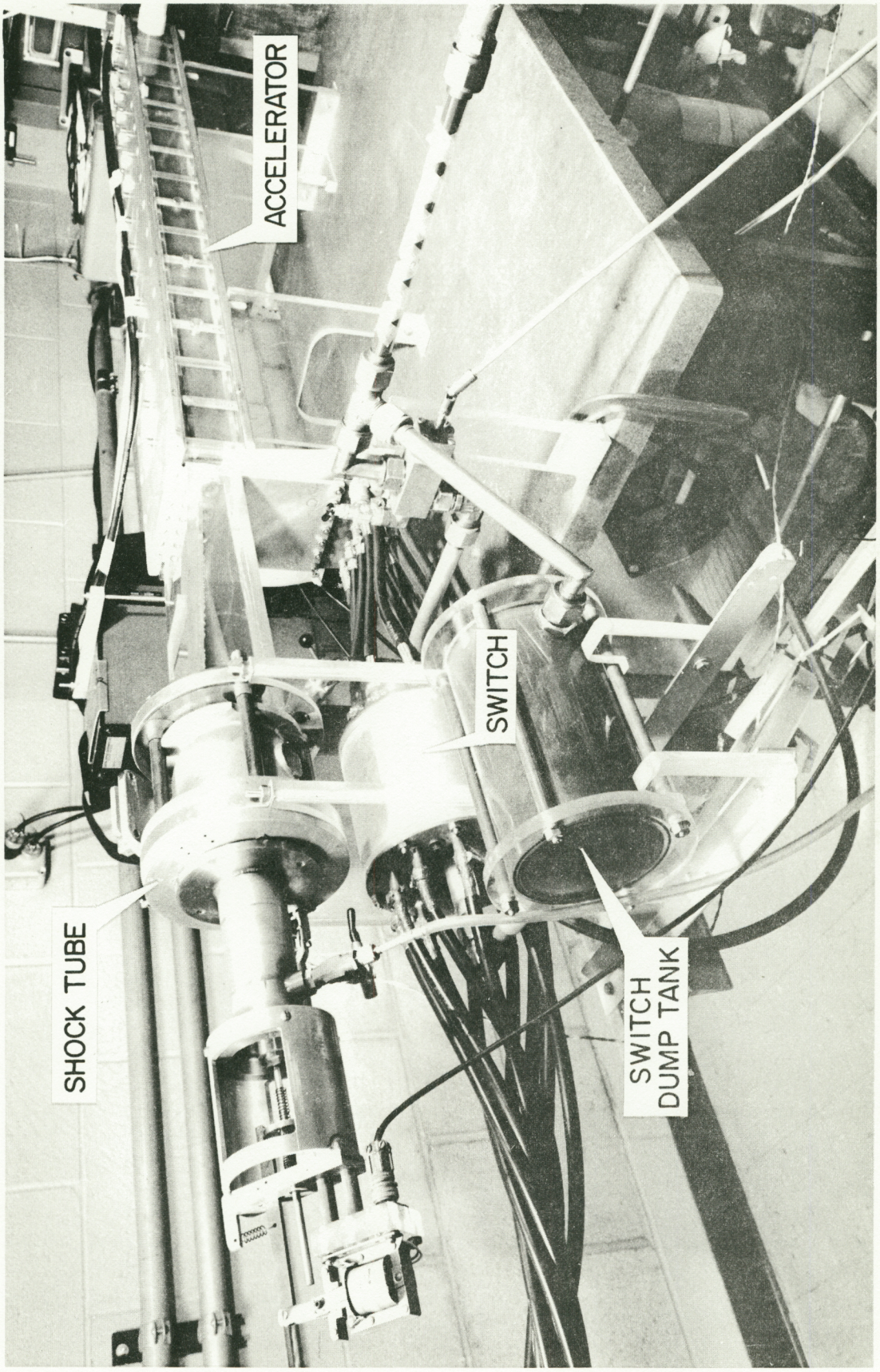

PARALLEL PLATE ACCELERATOR SYSTEM

FIGURE 3-2
AP 25 P 409

which results in the introduction of their ablation products, such as carbon and hydrogen, into the flow.

3-3 THE SHOCK TUBE MASS INJECTION SYSTEM*

The design concept of the mass injection system for this accelerator is similar to that employed in the MPD arc facility described in Ref. 3. The shock tube, illustrated in Fig. 3-3, consists of a 16 cm-long x 6 cm-ID driver section and a 49.5 cm-long driven section. The driven section consists of a ball valve and a 30.5 cm Plexiglas transition piece whose internal dimensions change from 6 cm-square at the ball valve to 2.5 x 12.7 cm at the injector end. A photograph which shows the driver section, ball valve, transition piece and a portion of the accelerator channel is shown in Fig. 3-4. Four Nylon injector tubes, 4.5 cm-long and 9.5 mm-ID connect the driven section directly to the accelerator channel. To adjust the mass flow to the desired value, injector orifice plugs of various sizes are inserted in the injection tubes at the accelerator side.

In a typical operating sequence, the driven section, the accelerator channel and switch are evacuated and the driver section is filled with argon to 2.1 atm; the safety systems are activated and the power source is loaded to the appropriate voltage. The diaphragm is then burst by a spring loaded plunger released by a solenoid. A stagnation region of relatively high pressure (of the same order as that originally in the driver) is formed at the end of the driven section where the injectors are located. Some gas is bled just downstream of the ball valve through a hole in the sidewall and is led to the gas-triggered switch through a 9.5 mm-ID Nylon tube. The length of this tube is adjusted to synchronize switch breakdown with the

*Mr. Adam Bruckner was instrumental in the design and testing of the apparatus described in this section. His cooperation is gratefully acknowledged.

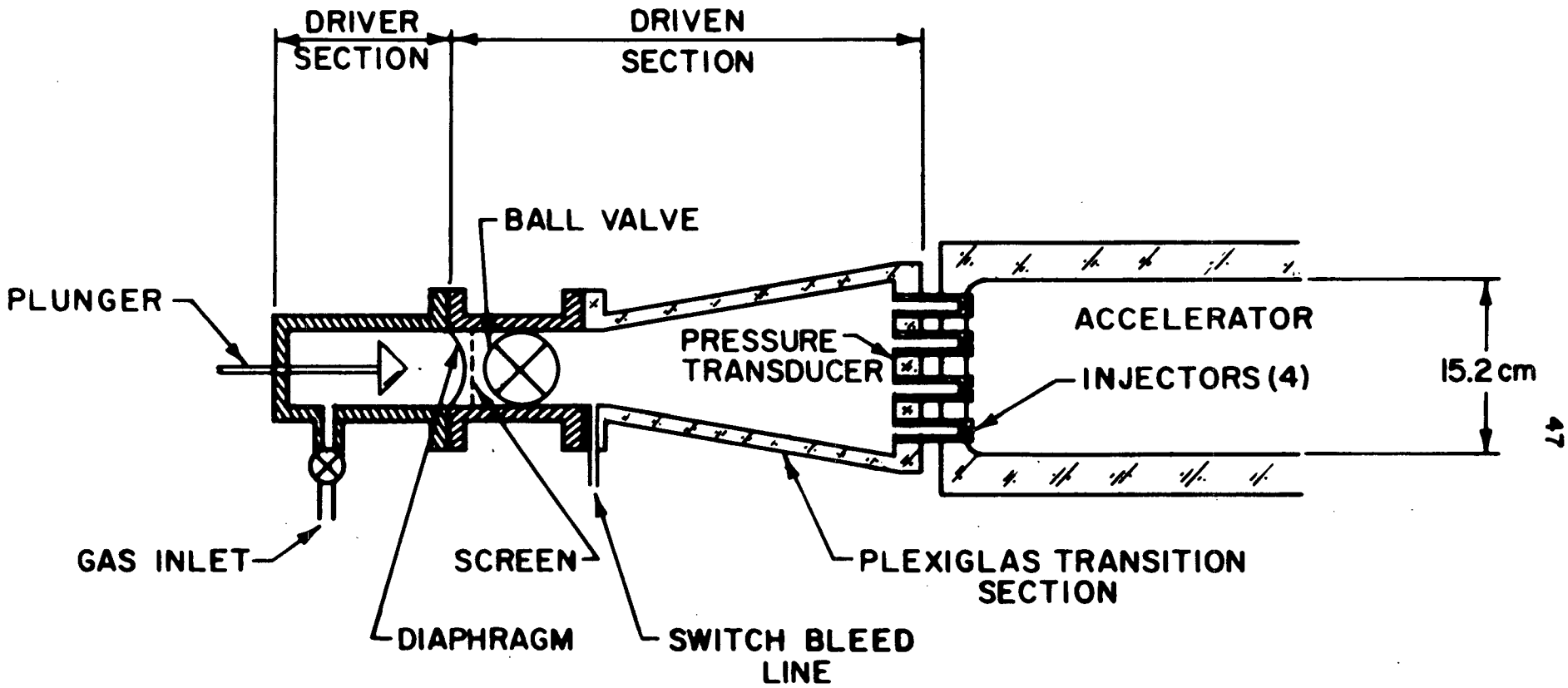

SHOCK TUBE INJECTOR

FIGURE 3-3
AP25-4635

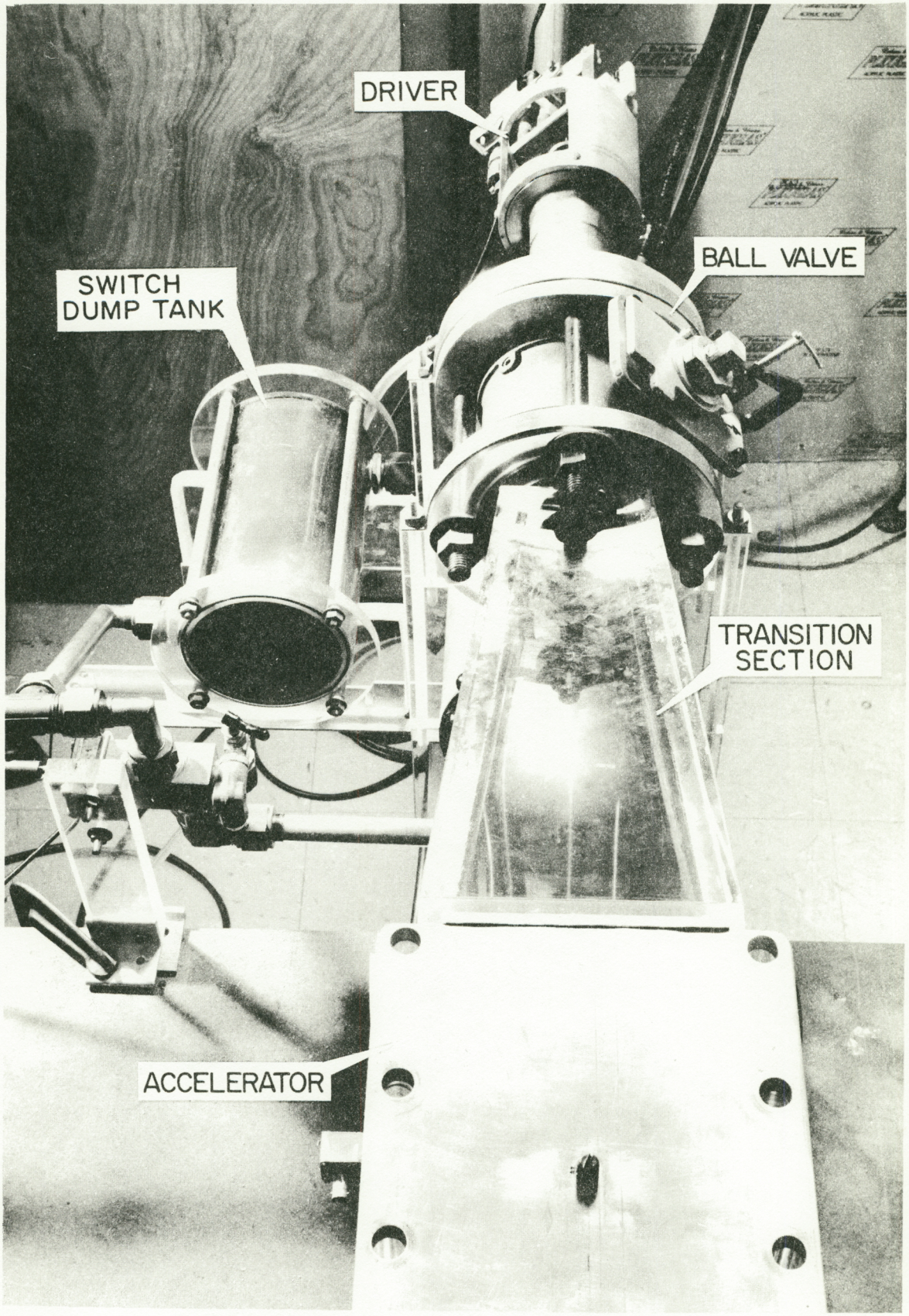

PHOTOGRAPH OF SHOCK TUBE

FIGURE 3-4

AP25 P410

achievement of steady cold gas flow in the accelerator. Depending on the loading voltage, breakdown in the accelerator occurs between 1.5 and 2 msec after the transducer in the shock tube begins to register pressure, by which time steady flow has been achieved in the accelerator, as will be shown later.

The mass flow requirements for the accelerator are determined by calculating the thrust due to the self-induced magnetic field (assuming one-dimensional MHD flow) with an exhaust velocity in the range of 10-25 km sec^{-1}. For example, a current of 10^5 A with an exhaust velocity of 25 km sec^{-1} predicates a mass flow rate of 85 g sec^{-1} while a current of 10^4 and an exhaust velocity of 10 km sec^{-1} predicates a mass flow rate of 2.1 g sec^{-1}. In order to arrive at the proper orifice size for a given mass flow, initial performance tests were carried out with the injector tubes closed. The pressure at the end wall of the Plexiglas driven section was monitored with a piezoelectric transducer described in Ref. 17 equipped with a cathode-follower amplifier. A typical stagnation pressure profile obtained with 2.1 atm driver pressure and a 0.071 mm thick, soft aluminum diaphragm, is shown in Fig. 3-5a. It shows a risetime of about 1.2 msec and exhibits a constant plateau after a slight overshoot. To establish the orifice sizes, the stagnation temperature of the gas at the injectors was initially approximated by assuming isentropic expansion from the driver pressure to the measured stagnation pressure in the driven section. With the orifices established, a series of static pressure measurements were carried out with 9.5 and 4.8 mm-ID orifices to monitor the onset of steady gas flow at various locations along the length of the channel. A large piezoelectric pressure transducer built by Eckbreth was employed[2]. Figure 3-5b shows the static pressure profile at a location 16 cm downstream from the injectors for

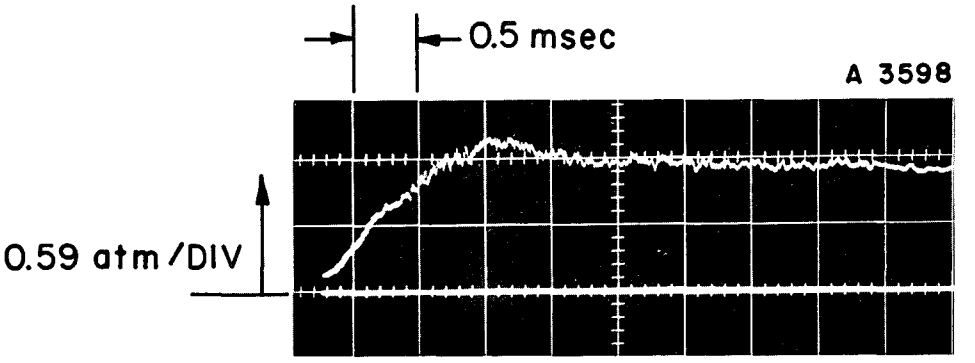

a) STAGNATION PRESSURE AT ENTRANCE TO INJECTOR

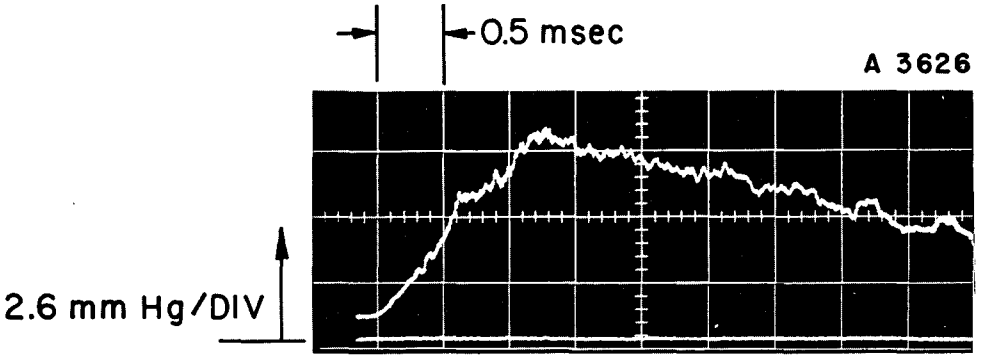

b) STATIC PRESSURE IN ACCELERATOR CHAMBER

STAGNATION AND STATIC PRESSURE RECORDS

FIGURE 3-5
AP25·343

9.5 mm orifices and 2.1 atm driver pressure. (The pressure sensor has been found to have an intrinsic decay of 7% per msec so that the static pressure after the 1.5 msec rise decays more slowly than it appears.) The steady pressure levels reached within the chamber are of the order of 7-10 Torr as a result of the large mass flow rates required for high current operation.

To check whether the isentropic assumption concerning the stagnation temperature in the driven section of the shock tube is reasonable, this temperature may be calculated indirectly using the measurements of stagnation pressure and static pressure described before. Assuming isentropic expansion through the injectors, the Mach number of the cold flow in the channel can be computed from the ratio of the static pressure measured on the channel wall to the stagnation pressure measured in the driven section of the shock tube. The flow velocity in the channel is obtained from the arrival times of the static pressure signal at various axial locations in the channel. The static temperature is then computed from the local sound speed, calculated from the Mach number and velocity of the flow. The stagnation temperature in the driven section may then be obtained from the Mach number and the static temperature. Although this method is based upon some questionable assumptions, it yields consistently high temperatures --- from 400 ^{o}K to 900 ^{o}K, depending on the initial shock tube driver pressure.

A more refined determination of the stagnation temperature was performed with a method which capitalizes on the prismatic shape of the transparent driven section of the shock tube and the density dependence of the refractive index of a gas. The apparatus, dubbed the "gas-prism schlieren densitometer", is shown in Fig. 3-6a. A laser light beam is passed through the driven section just upstream of the injectors. Since the Plexiglas walls are not parallel,

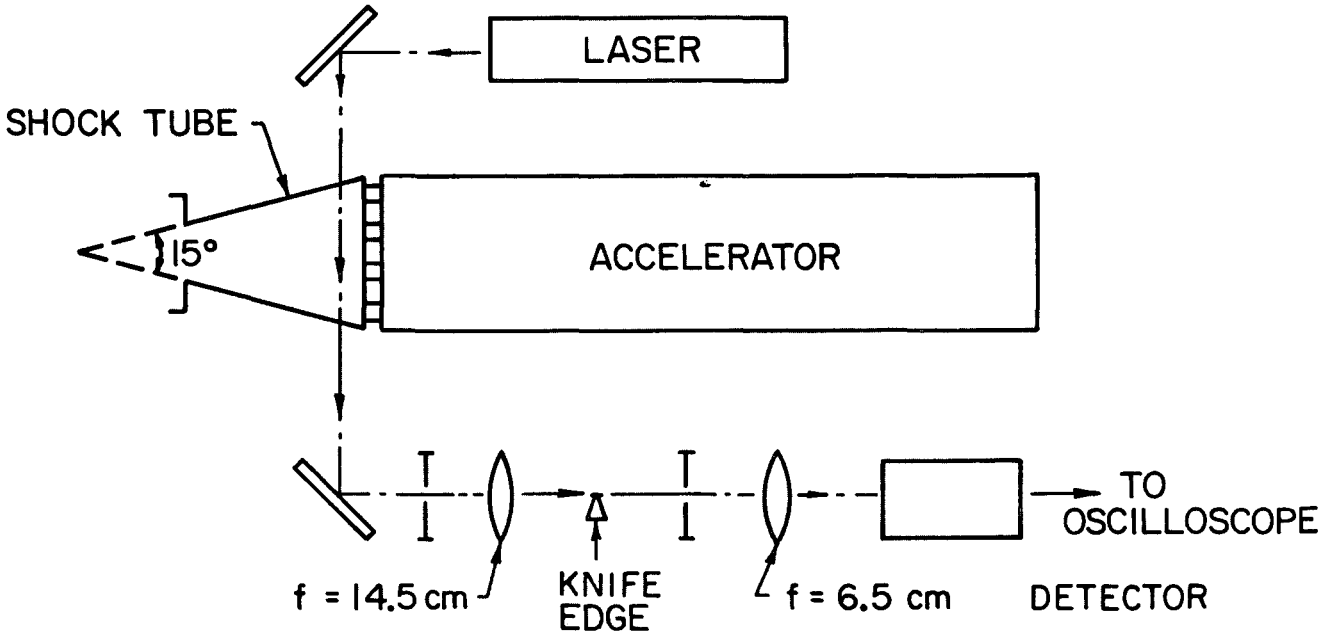

a) SCHEMATIC

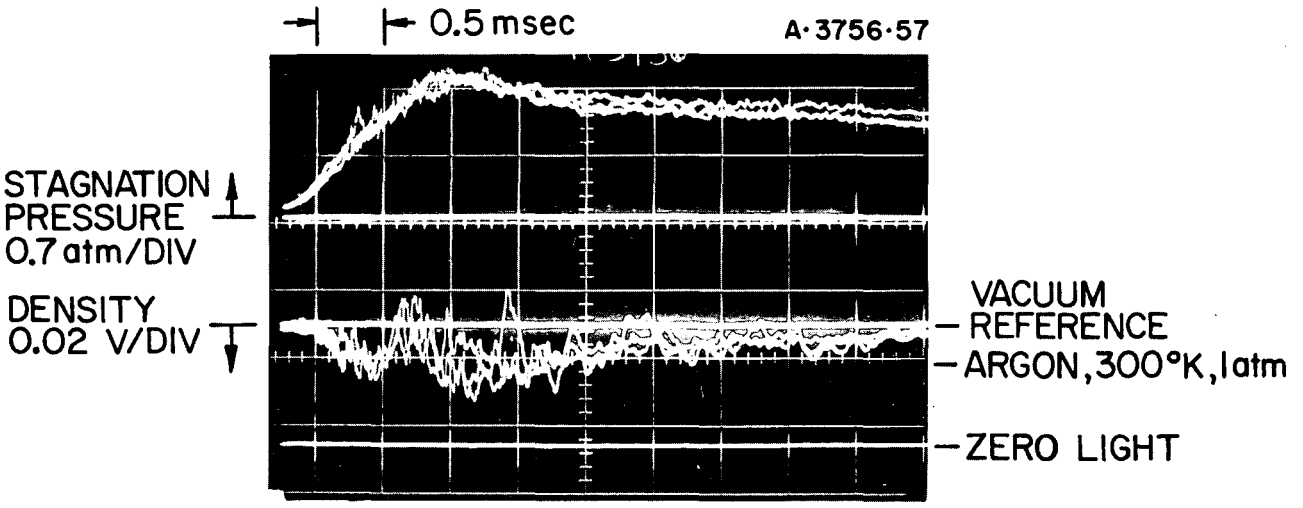

b) STAGNATION PRESSURE AND DENSITY
DRIVER PRESSURE: 30 psia (ARGON)

GAS PRISM SCHLIEREN DENSITOMETER

FIGURE 3-6
AP25-344

the interior constitutes a prism which will cause a deflection of the light beam through an angle which depends on the gas density in the interior of the prism and its apex angle. For small apex angles, the deflection is proportional to μ-1 (where μ is the refractive index) which for gases is proportional to the density. After passing through the shock tube, the laser beam is focused to a very small spot on an adjustable knife edge by a lens. Thence, the light passes through another lens which focuses the beam on a silicon photodiode detector. With the shock tube initially evacuated ,the knife edge is moved about halfway into the focused laser beam. Thus any deflection of the beam ahead of the knife edge will cause more or less of it to be cut by the knife edge, which results in a change of intensity at the photodiode. This system is very sensitive to the small deflections (typically 10^{-4} radians) of the laser beam caused by density variations within the shock tube.

A typical set of results is shown in Fig. 3-6b,which is an overlay of three tests. The top trace represents the stagnation pressure and the bottom trace represents the light intensity reaching the protodetector. The upper baseline bracketing the lower trace was obtained with the shock tube evacuated and the lower baseline is the zero light intensity reference. The mark: "Argon, 300°K, 1 atm" corresponds to the deflection obtained by filling the shock tube with argon to a pressure of 1 atm at 300°K. A density increase in the driven section deflects the light beam in a direction such that more of the beam is intercepted by the knife edge, hence reducing the light intensity at the detector. Shot to shot reproducibility is fair. The high frequency noise on the signal is due to true schlieren effects, i.e., local density gradients perpendicular to the laser beam which could be the result of turbulence in the shock tube gas.

The simultaneous pressure and density data may be used to calculate the stagnation temperature assuming the perfect gas law. The stagnation temperature as a function of time is shown in Fig. 3-7 and 3-8 for initial driver pressures of 2.1 atm and 3.2 atm respectively. Due to the shot-to-shot variations in both the pressure and the density, the possible error is rather large as shown by the typical error bars in the graphs, especially at the location of the high temperature peak. (The latter is probably due to true schlieren effects associated with large scale wave phenomena.) The results confirm that the stagnation temperature is larger than the value estimated on the basis of isentropic expansion from driver to driven section. Another interesting result is that little is gained by operating the driver section with pressures above 2.1 atm because the resulting rise in the stagnation temperature in the driven section tends to nullify the effect of increased stagnation pressure.

With the measured values of stagnation pressure, $p_o = 1.3 \times 10^5$ N m^{-2}, and stagnation temperature, $T_o = 400^oK$, the computed mass flow for the 2.1 atm driver and the 9.5 mm-ID orifices is 96 ± 16 g sec^{-1} while for the 4.8 mm-ID orifices the mass flow is 24 ± 4 g sec^{-1}. Due to the uncertainty in the temperature determination, the error in the computed mass flow is of the order of 30%.

3-4 THE SWITCH

The power source is connected to the accelerator through a cylindrically symmetric gas-triggered discharge switch. The switch, shown schematically in Fig. 3-9, is a modification of the one described in Ref. 18. Modifications were required due to premature breakdown of the switch after 4 or 5 pulses and leaks which developed after operation above 50 kA. A chemical analysis of the material deposited on the surface of the Plexiglas insulators confirmed the presence of Fe which was presumed to have sputtered

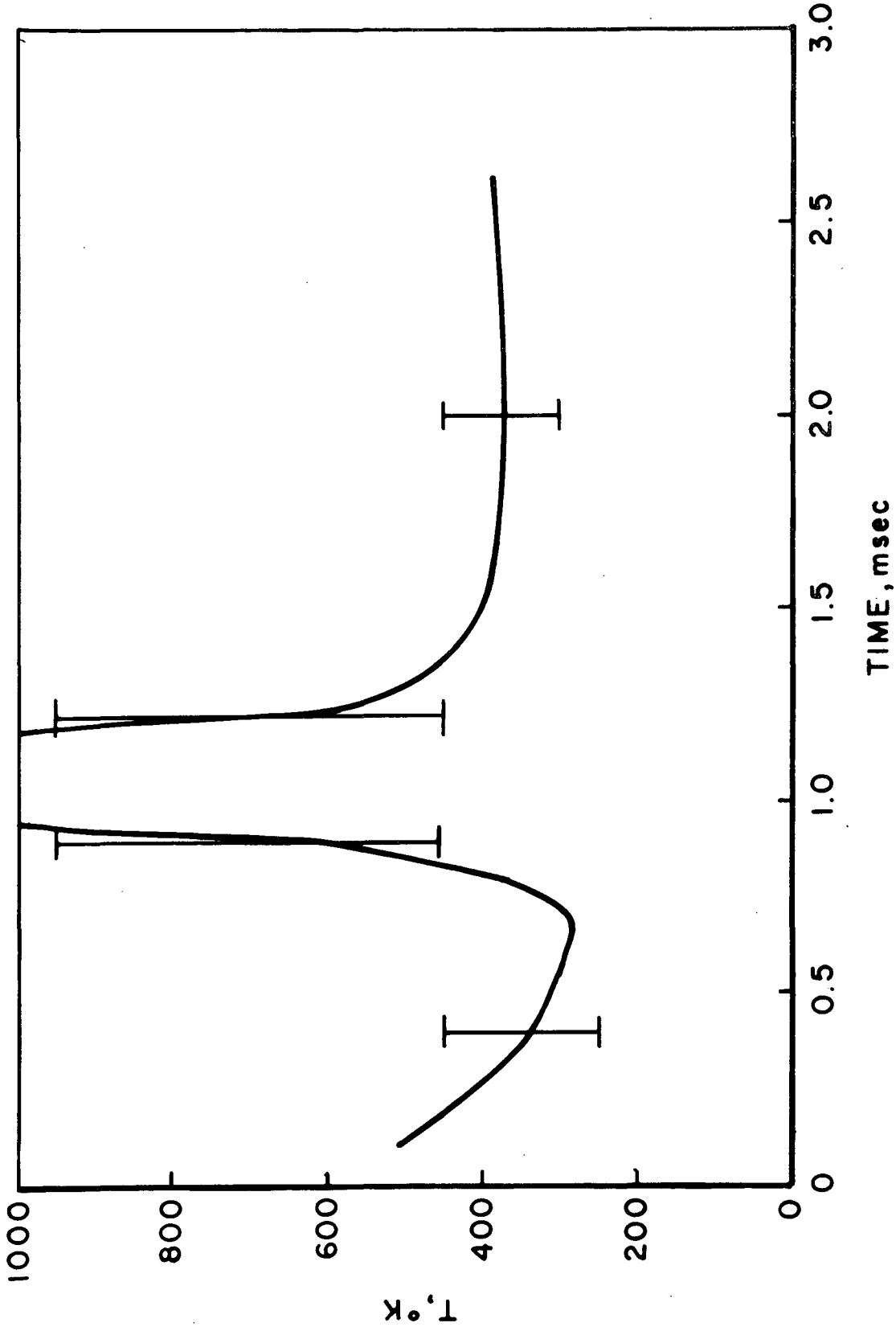

STAGNATION TEMPERATURE AT DRIVEN SECTION END WALL
DRIVER PRESSURE: 2.1atm (ARGON)

FIGURE 3-7
AP25-4637

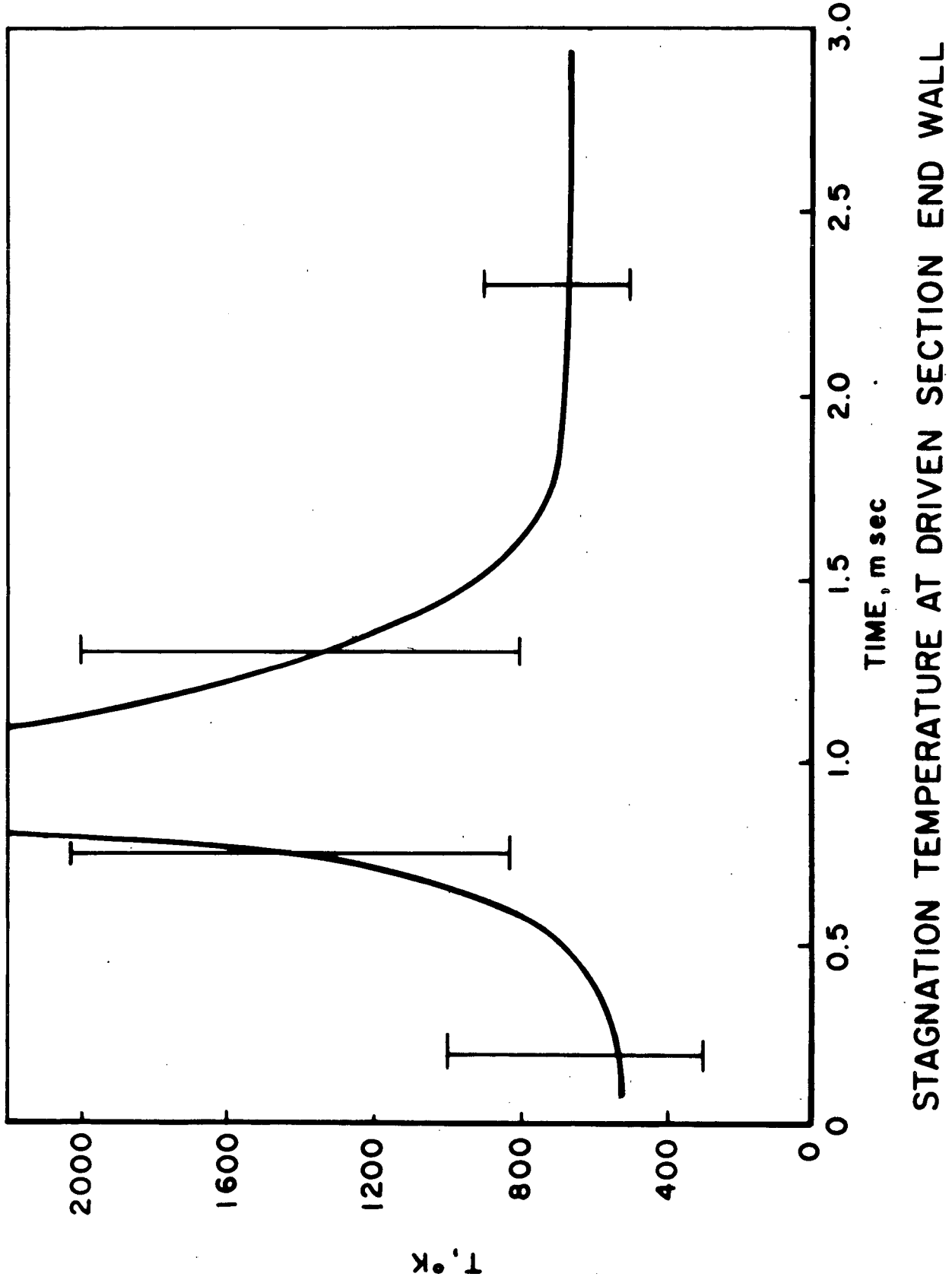

FIGURE 3-8
AP 25-4636

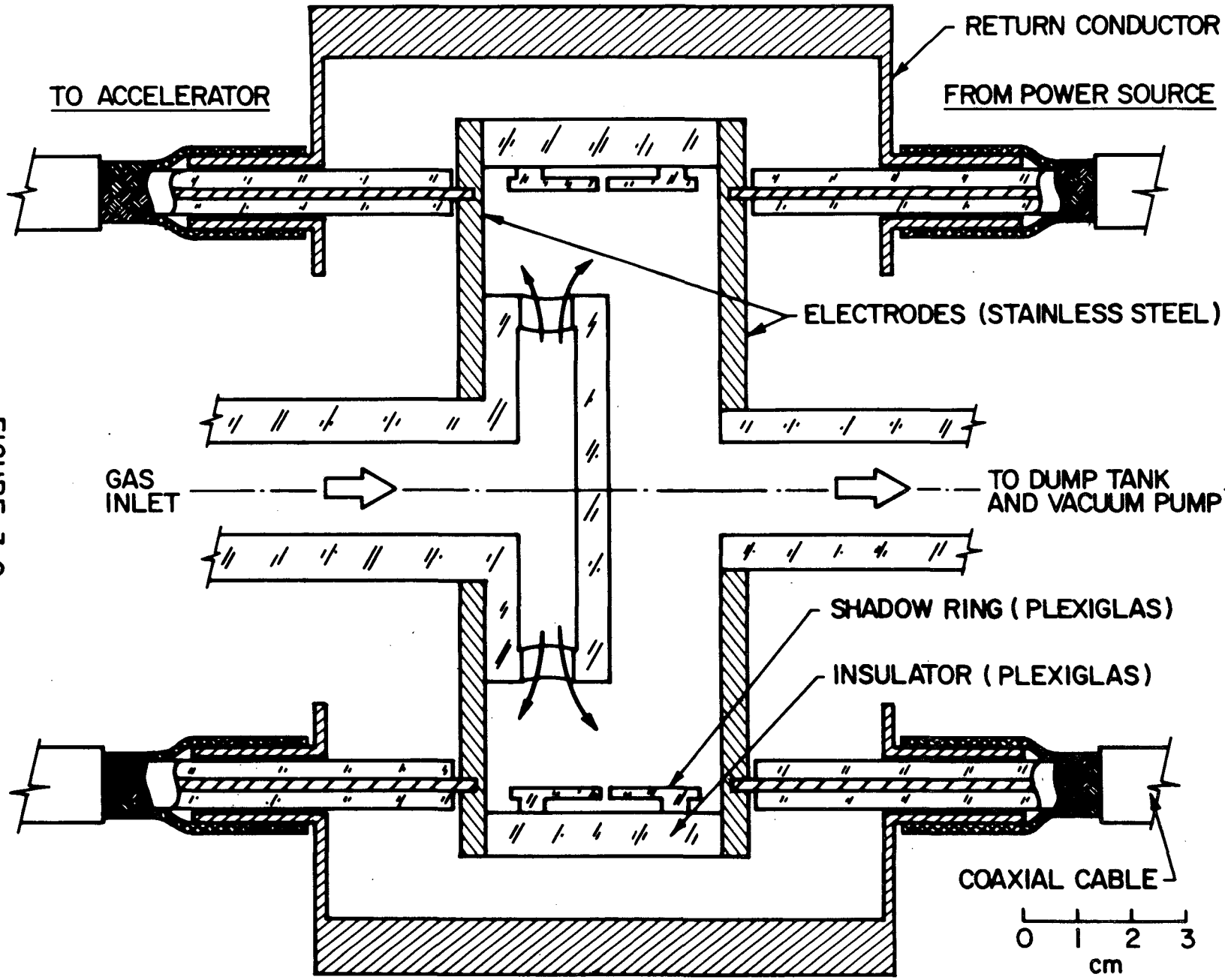

SCHEMATIC OF SWITCH

FIGURE 3-9
AP25 4770

from the stainless steel electrodes and which is believed to be responsible for the premature breakdown of the switch. The insulator was also covered with soot, a by-product of the ablation of Plexiglas. The breakdown problem was solved by the addition of two rings to the surface of the outer insulator, which shadows it from sputtered electrode material, and by shortening of the central insulator to provide one less surface along which breakdown can occur. Soot, blown past the "O" ring seals is believed to be responsible for the leaks encountered during high current operation. This problem was solved by addition of a dump tank shown in Fig. 3-2. This tank relieves the pressure developed in the switch during the current pulse. At the same time it provides a large surface to condense the by-products of ablation from the switch before they deposit on the insulator surfaces causing premature breakdowns. With these modifications, the switch can withstand as many as 150 pulses before requiring disassembling for cleaning of the electrodes and insulator.

CHAPTER 4

EXPERIMENTAL OBSERVATIONS

4-1 INTRODUCTION

This chapter describes all the experimental observations and measurements performed on the parallel plate accelerator. The measurements are concentrated mainly upon the terminal properties of the accelerator and upon the properties of the flow out of the acceleration region. For completeness, however, some measurements and observations performed on the acceleration region will be presented as well. Analysis of the observations and measurements is presented in the next chapter.

The main portion of the investigation was performed with the pulse of 210 μsec,duration delivered by the parallel connection of the four units in the power source. It will be shown that the pulse length is sufficient to insure quasi-steady operation, and that current levels above 50 kA in this geometry insure vigorous electromagnetic acceleration of the flow to supersonic velocities, which is an important characteristic of quasi-steady MPD accelerators.[19] At these current levels, moreover, the back emf of the accelerator, which scales as the product of velocity and magnetic field is expected to reach a significant fraction of the voltage drop across the accelerator. It is shown in the next chapter that this expectation is not fully realized, because of the low velocities encountered.

4-2 CURRENT AND VOLTAGE MEASUREMENTS

The current is measured with a 175 turn 13.6 cm-long coil wound on a 6.3 mm-OD Plexiglas rod. It is located between the 15.1 cm-wide copper plates which connect the switch to the accelerator and has its axis perpendicular

to the direction of the current flow. It provides a signal which is proportional to the time rate of change of current in the circuit. This signal is integrated with a passive integrator with a time constant RC = 9.0 msec and displayed on a Tektronix 555 oscilloscope. A detailed discussion of the circuitry which is usually employed in this type of measurement is presented in Ref. 8. The coil and integrator assembly were calibrated against a Pearson Electronics Inc. Model 301 wide-band precision current transformer SN 1128-9. The calibration constant of the assembly is: $(1.87 \pm 0.05) \times 10^5$ A V^{-1}

The voltage drop V across the accelerator is the sum of three components: a resistive drop V_R, an induced emf V_{uB} which originates with the motion of the plasma across the magnetic field and an inductive drop V_D. This voltage arises due to a time rate of change of magnetic flux in the accelerator which originates either with time derivatives of the current, or with gross motions of the current distribution. Unfortunately, it is not possible to measure V_R and V_{uB} separately. However, $(V_R + V_{uB})$ and V_D can both be obtained through straightforward techniques. In the schematic presented below, V is the voltage measured across the terminals of the accelerator, V_M is the voltage measured downstream of the current distribution with a circuit which links no magnetic flux and V_D is the voltage measured with a loop which encloses the same magnetic flux as the accelerator. By Faraday's Law, traversing the circuit formed by V and V_M in a counterclock wise direction:

$$-V + V_M = -\frac{d\phi}{dt} \tag{4-1}$$

where ϕ is the magnetic flux linked by the circuit.

Traversing the circuit formed by V_D and the loop,

$$-V_D = -\frac{d\phi}{dt} \tag{4-2}$$

and therefore:

$$-V_D + V_M = V \tag{4-3}$$

V_M is therefore the sum of V_R and V_{uB}.

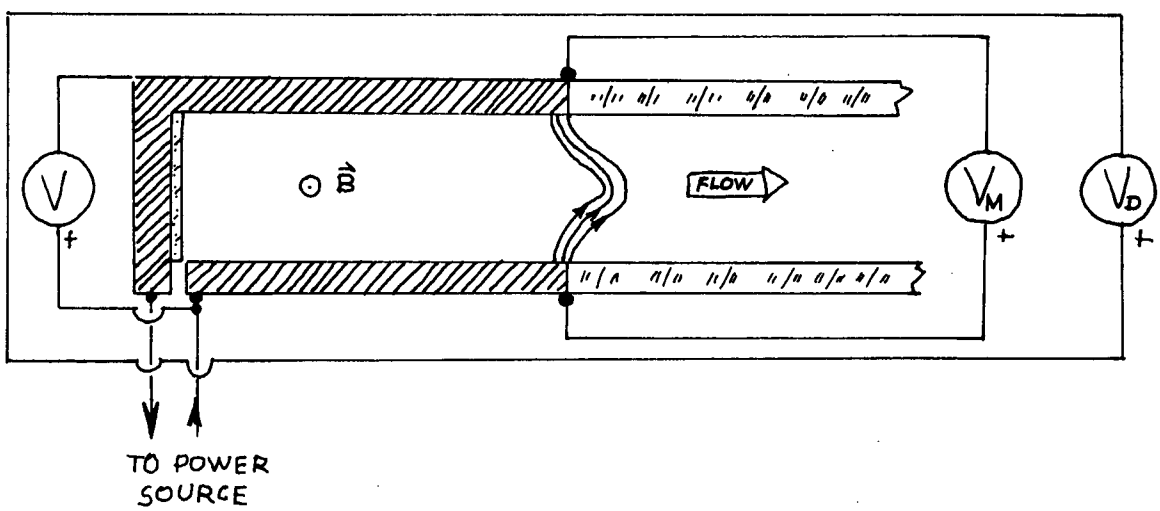

The three voltages V, V_M and V_D are measured with Tektronix P 6013 voltage probes and displayed on a Tektronix 555 oscilloscope. The loop employed to measure V_D consists of one turn of wire insulated from and taped to the electrodes in order to enclose the same magnetic flux as the accelerator. Fig. 4-1a shows a simultaneous record of V, V_M and $-V_D$ as well as the current I in the accelerator. The current is constant and V and V_M are identical except for the first 50 μsec in which the voltage V_D is substantial. For the rest of the pulse, V_D is almost indistinguishable from the baseline indicating that the inductive component of V is negligible. Fig. 4-1b shows

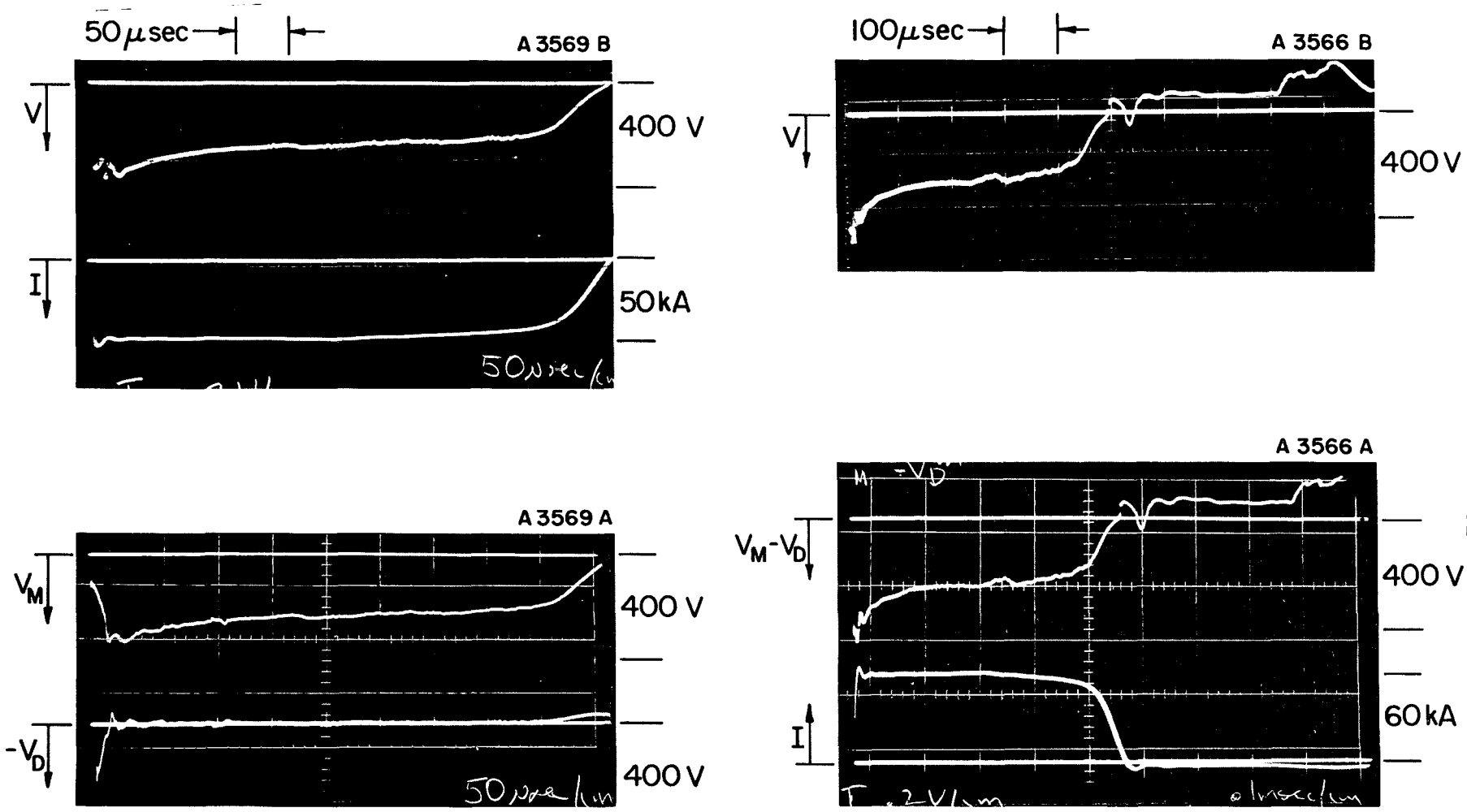

a) V, I, V_M AND $-V_D$
I = 50 kA

b) V, $V_M - V_D$ AND I
I = 60 kA

CURRENT AND VOLTAGE SIGNATURES
(100 μ AMBIENT ARGON)

FIGURE 4-1
AP25 P 421

a simultaneous record of V and $V_M - V_D$, the latter obtained by subtracting the signal from the two probes in a Type G differential preamplifier. As predicted by Eqn. 4-3, V and $V_M - V_D$ are identical. Therefore, the inductive component of the terminal voltage V can be measured independently as V_D, which helps to establish when the discharge attains electrodynamic stabilization.

Figure 4-2 shows a simultaneous record of V_M, V_D and I for the pulse of 210 μsec duration and a mass flow of argon of 96 g sec^{-1}. The current I is 85 kA, the inductive voltage V_D attains a value of less than 10V, 60 μsec after current initiation indicating that electrodynamic stabilization has been achieved. At 60 μsec V_M achieves a plateau of 275 V which lasts 140 μsec indicating that the accelerator is operating in the quasi-steady regime. The measured plateau in the voltage V_M, which is identical to the terminal voltage after stabilization, obtained with three different mass flows of 24, 48, and 96 g sec^{-1} is presented in Fig. 4-3. The accuracy of the measurements is limited by the oscilloscope to $\pm$ 5%. The voltage is almost linear with current and the slope of the current-voltage characteristic increases with decreasing mass flow.

4-3 AERODYNAMIC OBSERVATIONS OF THE FLOW

Photographic observation of self-luminous bow shock waves over wedge-shaped airfoils inserted in the flow provides another indication that quasi-steady operation of the accelerator has been achieved and allows an estimate of the Mach number of the flow. A typical photograph of attached bow shocks formed on a wedge 2.5 cm wide slightly inclined to the flow, 20 cm downstream of the electrode insulator junction is shown in Fig. 4-4. The photograph was taken through the sidewall of the accelerator, 130 μsec after discharge initiation on Polaroid Type 52 film with a Graflex camera (127 mm $f/4.7$ Lens) through an Electro Optical

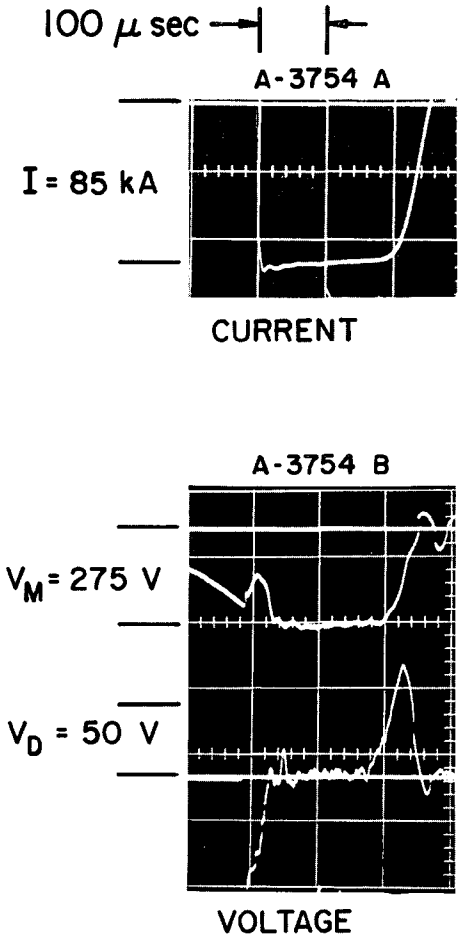

CURRENT AND VOLTAGE SIGNATURES
I = 85 kA, $\dot{m}$ = 96 g/sec

FIGURE 4-2
AP25 P 358

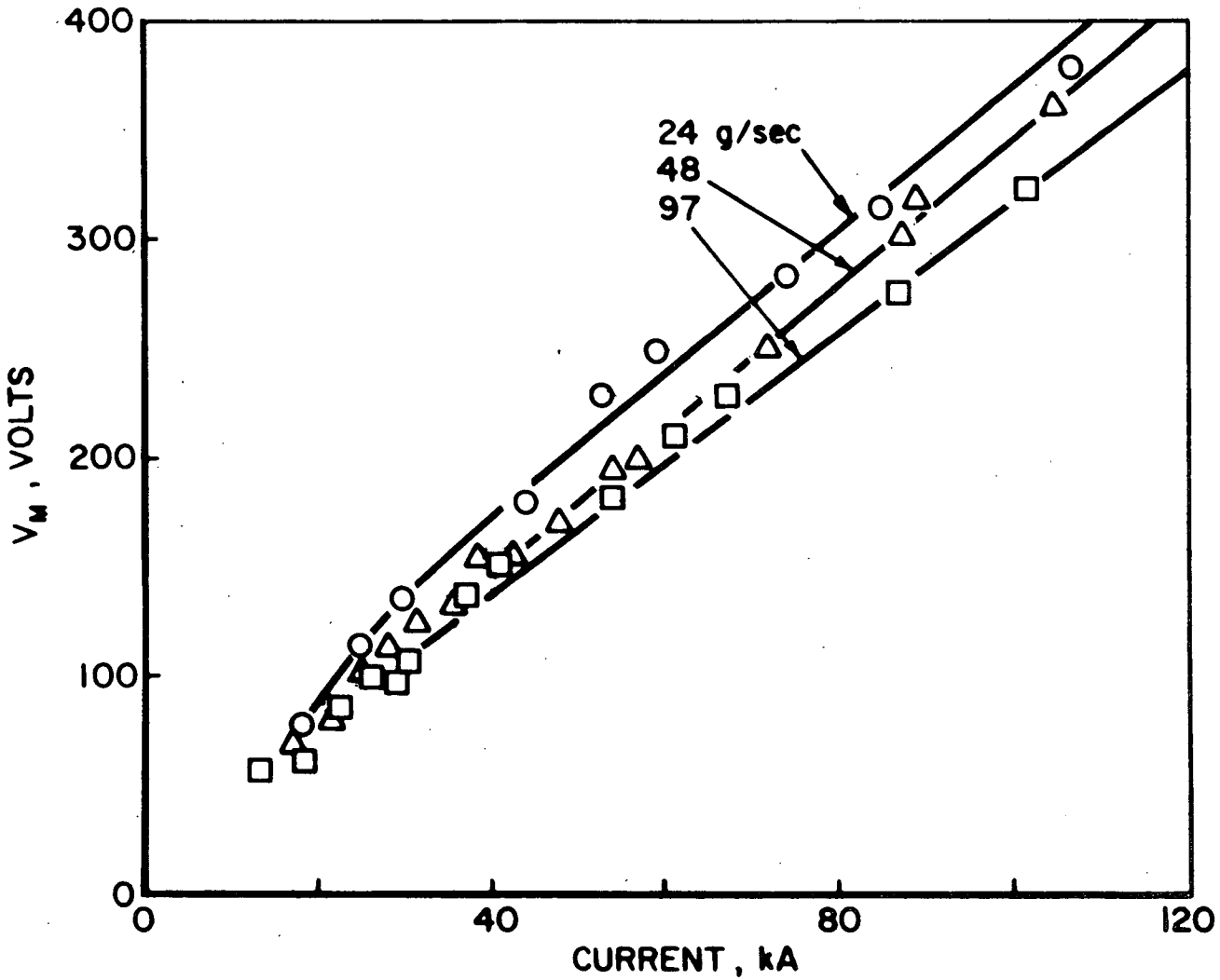

VOLTAGE AS A FUNCTION OF CURRENT, PARALLEL-PLATE ACCELERATOR

FIGURE 4-3
AP 25 R 4623 70

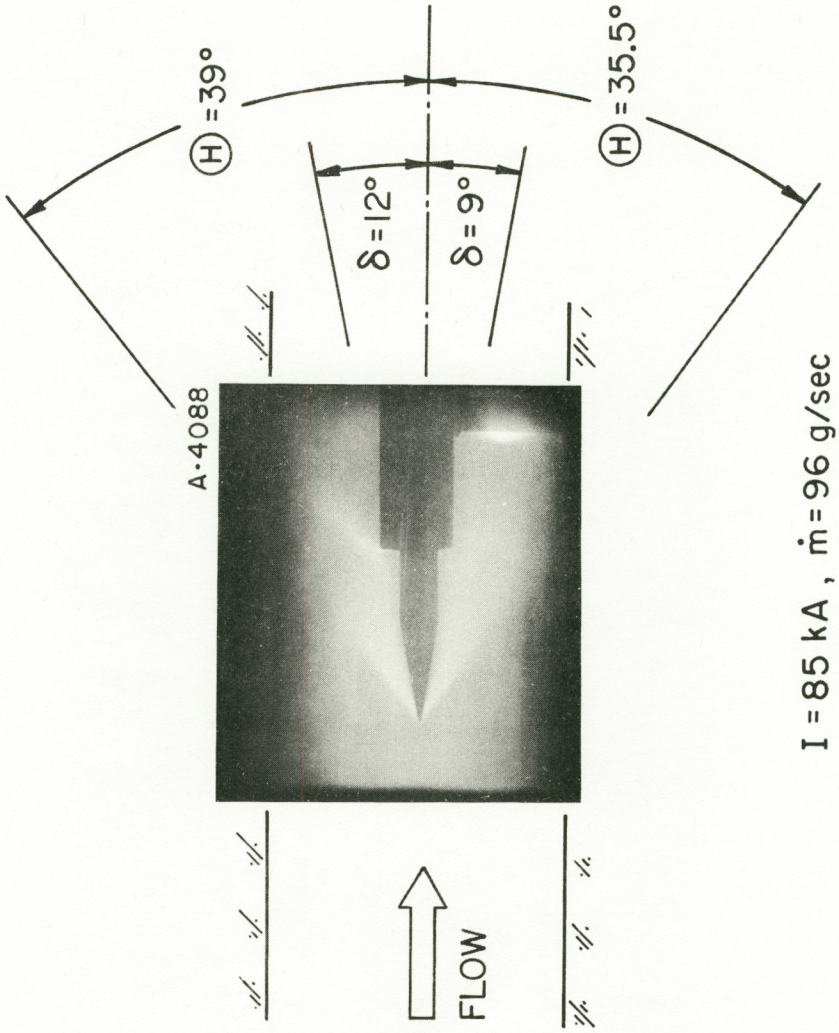

FLOW OVER WEDGE

FIGURE 4-4
AP 25 P 357 70

Instruments Inc. E-51 Kerr-cell shutter which can be triggered at a preset time during the pulse and which remains open for 5 μsec. The shock angles observed in a sequence of such photographs are found to be constant over a large fraction of the current pulse. This observation lends support to the conclusion drawn from the terminal measurements that quasi-steady flow prevails in the accelerator.

To obtain an estimate of the Mach number of the flow and the effective specific heat ratio γ, the shock angle θ has been measured from photographs of the flow over wedges with turning angles δ ranging from 9° to 24°. The Mach number can be obtained from:[20]

$$M = \left(\frac{2 \operatorname{ctn} \theta + 2 \tan \delta}{\sin 2\theta - (\gamma + \cos 2\theta) \tan \delta} \right)^{1/2} \qquad (4\text{-}4)$$

The effective specific heat ratio γ is not known <u>a priori</u>. Therefore, the Mach number is obtained with different assumed values of γ ranging from 1.3 to 1.7 as shown in Fig. 4-5. The requirement that the indicated Mach number remain constant for wedge angles up to the maximum deflection angle of the flow is satisfied by an effective γ of the plasma between 1.3 and 1.4. The corresponding Mach number for I = 87 kA and $\dot{m}$ = 48 g sec^{-1} is close to 2. Fig. 4-6 shows the Mach number determined in this manner for various currents in the range of 50 to 100 kA for two different input mass flows. Within experimental accuracy, the Mach number for the 24 g sec^{-1} input mass flow is nearly independent of current with a value of 1.9 ± 0.2 while for 96 g sec^{-1} its value is 2.0 ± 0.2. For 96 g sec^{-1} mass flow, the shocks became too diffuse to provide useful measurements below 80 kA.

4-4 PHOTOGRAPHIC OBSERVATIONS OF THE DISCHARGE REGION

Photographic observations of the discharge region were undertaken with two purposes in mind: to provide another

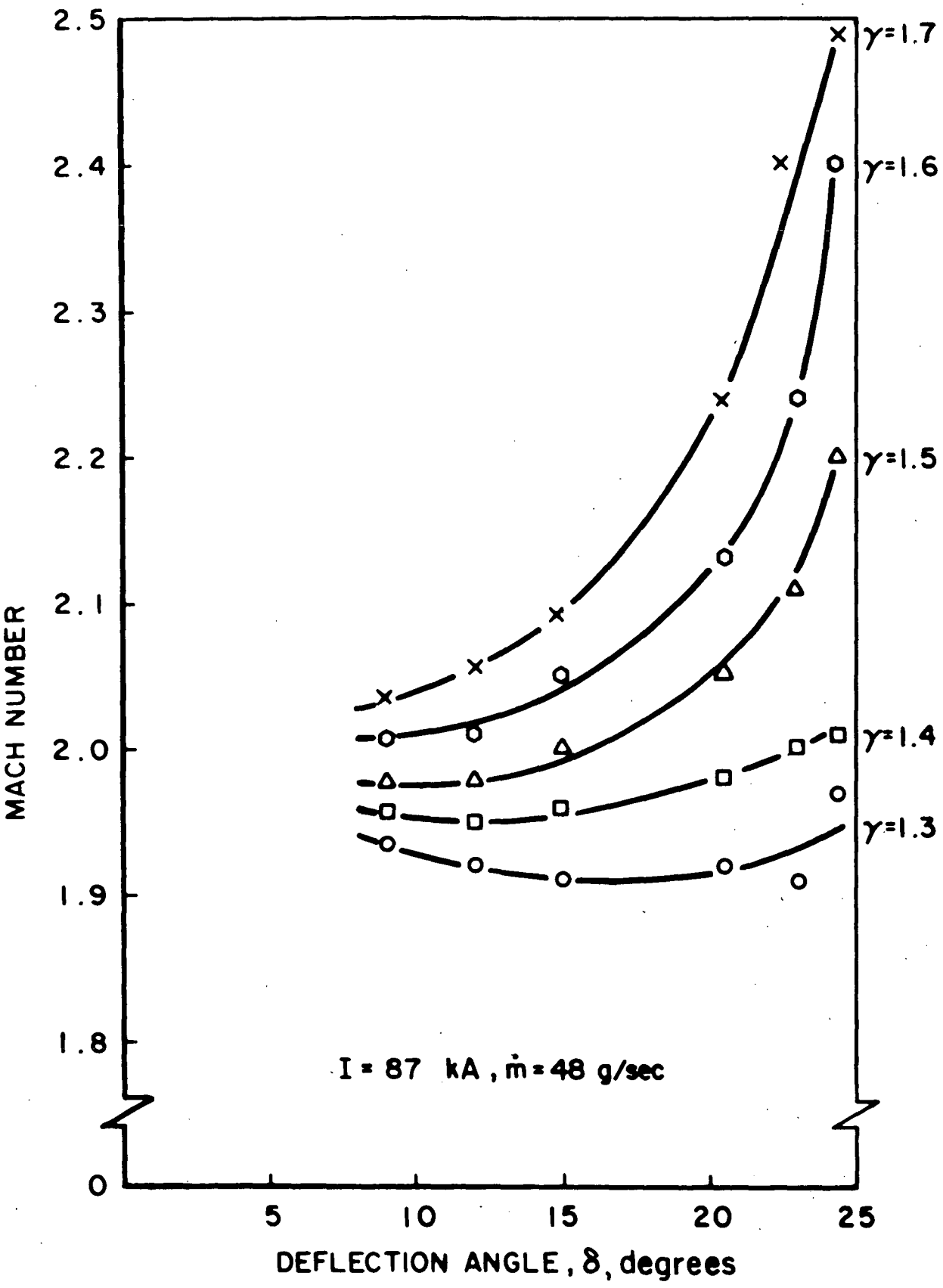

MACH NUMBER AS FUNCTION OF DEFLECTION ANGLE

FIGURE 4-5

AP 25 R 4625 70 A

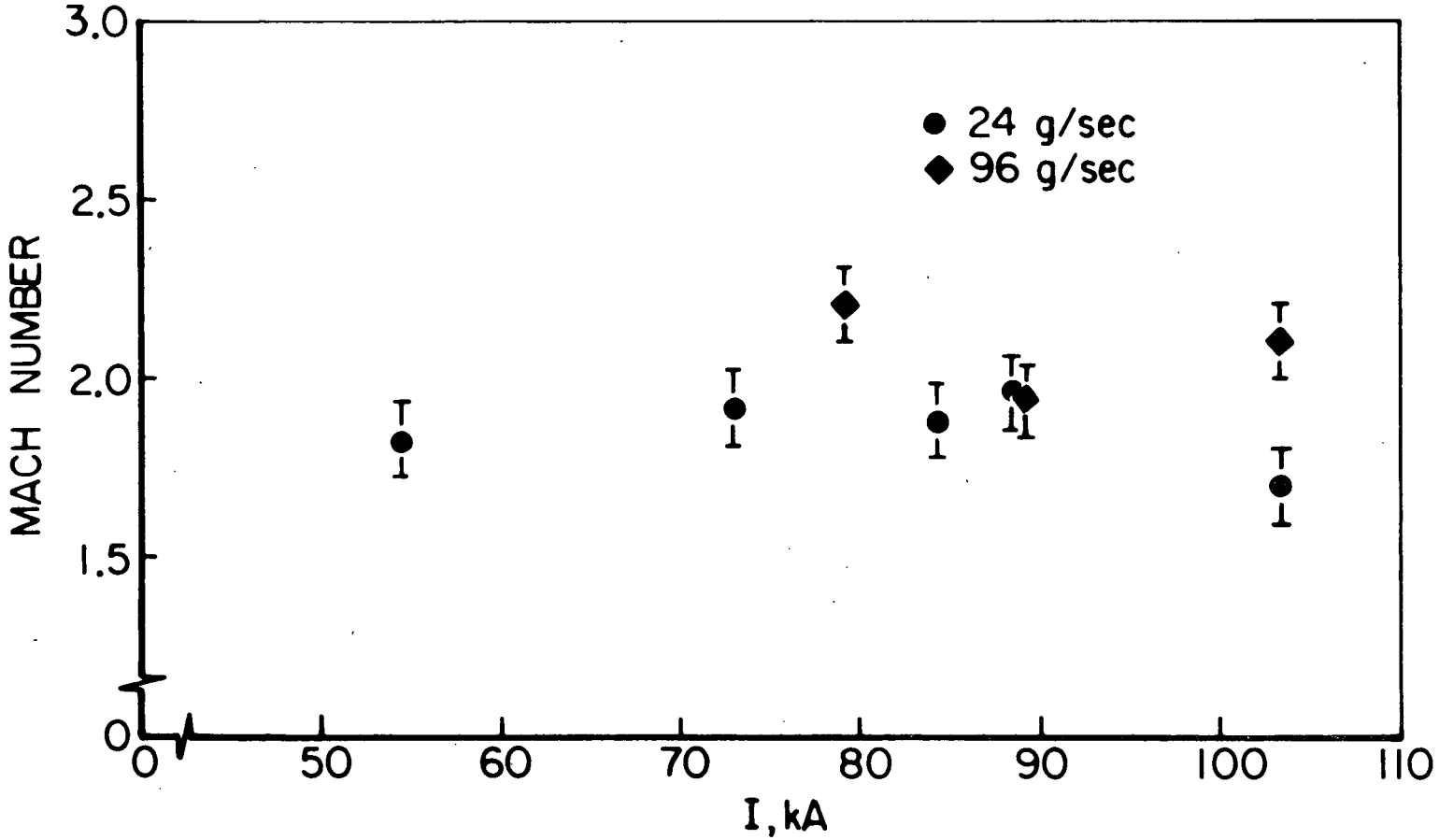

MACH NUMBER AS A FUNCTION OF CURRENT

FIGURE 4-6
AP 28 4675 70 A

confirmation of quasi-steady operation and to estimate the extent and shape of the discharge region. In particular, it was desired to establish that the radiance from any region of the discharge remains reasonably constant over a major portion of the pulse and that the radiance associated with the initiation of the discharge can be neglected. These are important considerations in the interpretation of spectroscopic data which is recorded with an open shutter and which therefore represents a time integral of the radiance of the discharge over the length of the current pulse. It was also desired to establish whether the discharge exhibits any tendency to collapse into a spoke.

Figure 4-7 shows a side view of the discharge for I = 85 kA using the camera and shutter described in the previous section. Figure 4-7a shows the accelerator channel and the location of the electrode insulator junction. Figure 4-7b taken at 20 μsec, displays the initiation phase and Fig. 4-7c, at t = 60 μsec, shows the discharge radiance in the configuration it will retain for the rest of the pulse, as verified in Figs. d, e, and f taken at 140, 180, and 200 μsec respectively. It is evident from the photographs that the radiance pattern achieves a steady state and remains fixed throughout the remainder of the current pulse. Since each pulse yields only one photograph, and since the radiance pattern at different times for successive pulses remains unchanged, it can be concluded that the accelerator operates in the quasi-steady regime in a highly reproducible manner. At the cathode, the radiance is diffuse and appears uniform across the whole width of the channel. At the anode there is the appearance of a slight concentration, the extent of which can be determined from a perspective view of the discharge region which will be presented shortly. The space between the

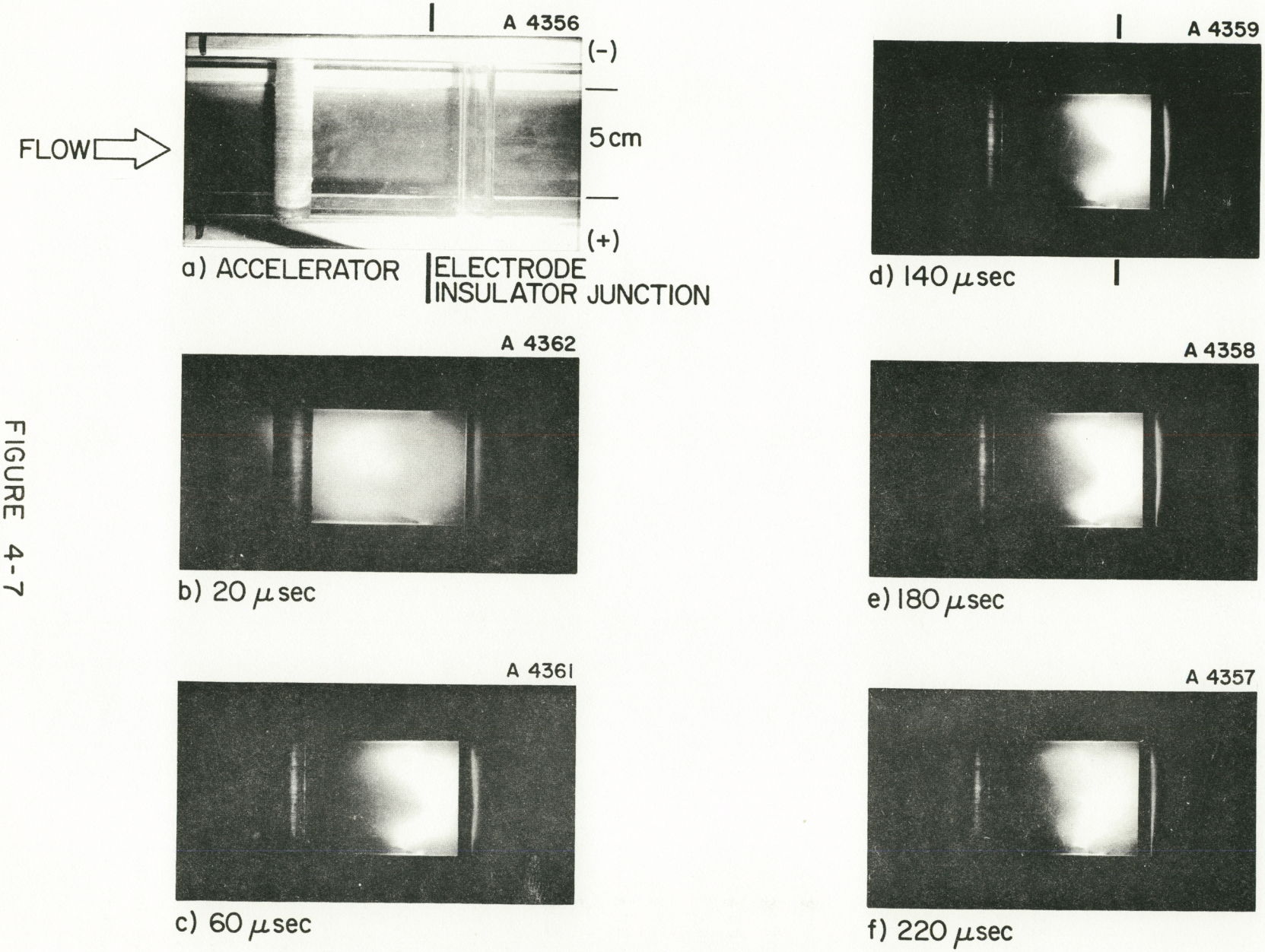

PHOTOGRAPHS OF ACCELERATOR OPERATION (SIDE VIEW)
$I = 85$ kA , $\dot{m} = 96$ g/sec

FIGURE 4-7
AP25 P 422

electrodes at the axial position of the electrode insulator junction is dark suggesting that the central portion of the discharge region is convected downstream by the flow while the edges remain attached to the electrodes, giving the discharge its characteristic hair-pin appearance.*

A perspective view of the discharge is presented in Fig. 4-8. It was taken at approximately a 68° angle upstream to the direction of flow. The target mark shown in Fig. 4-8a is placed across the channel and its center coincides with the center of the channel. Again, the radiance at the cathode is diffuse and occupies the whole width of the channel while it appears to occupy only about one-half of the channel width at the anode. From this view, the central portion of the discharge region appears to be formed from two parabolically shaped radiance zones which merge one channel height downstream of the electrode-insulator junction.

4-5 SPECTROSCOPIC STUDIES

a) General Observations

Spectroscopic analysis of the visible radiation emitted by the plasma in this accelerator was undertaken to obtain information about the plasma composition. This composition, though qualitative in nature, is used to determine which species take part in the discharge and flow out of the acceleration region. This information is important because, ideally, the accelerator should operate only with the injected mass flow of argon. It is important to stress at this point that the information obtained about the composition is purely of a qualitative nature since the intensity of a spectral line is a complicated function of the population density, the photon energy and the transition probability of the levels between which the radiation originates. It is, therefore, difficult to establish the

*The small acceptance angle of the Kerr-cell system cuts off the radiance beyond the post shown in the right of the photographs.

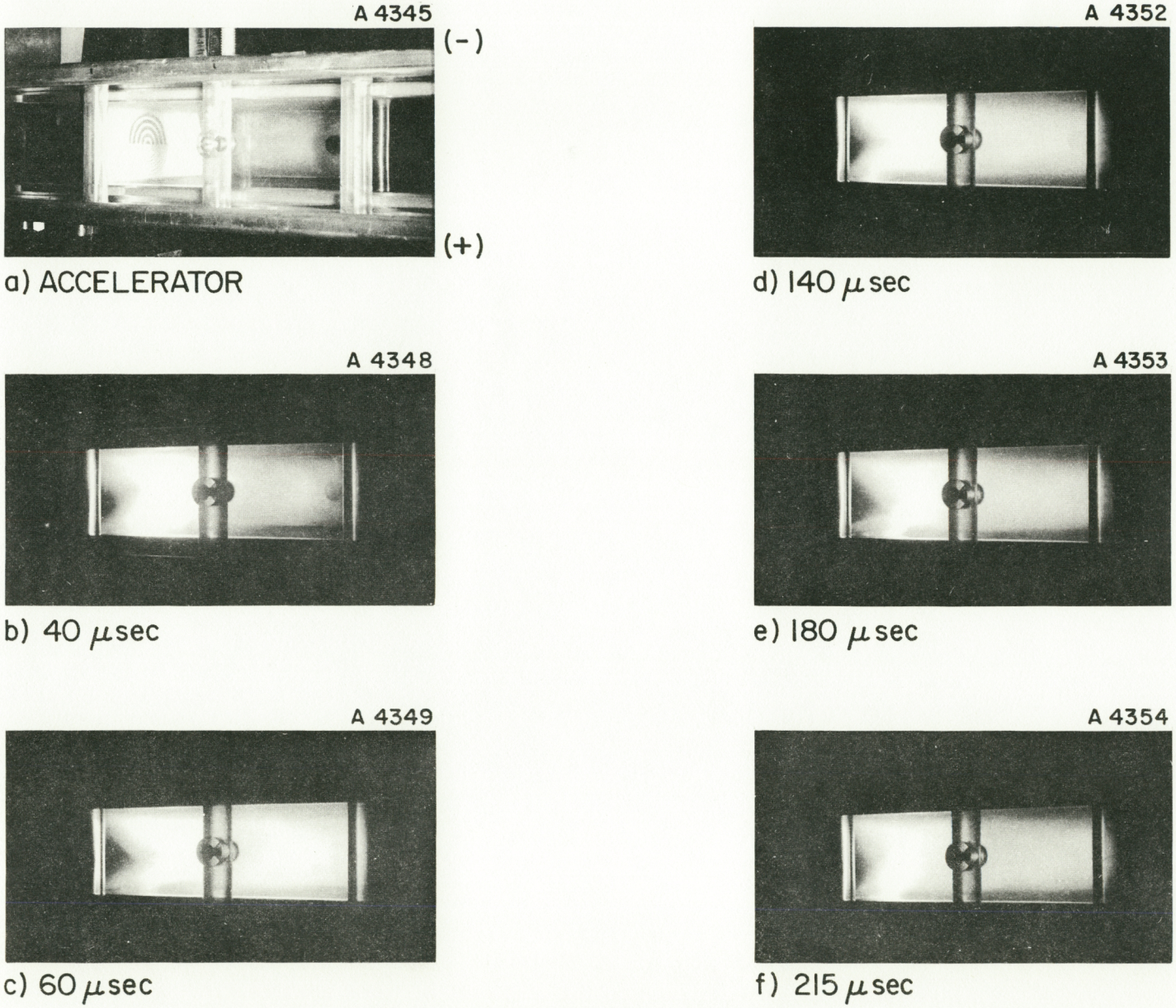

PHOTOGRAPHS OF ACCELERATOR OPERATION (PERSPECTIVE)
$I = 85$ kA, $\dot{m} = 96$ g/sec

FIGURE 4-8
AP 25 P 423

abundance of radiators from the intensity of their radiation. Another difficulty which arises is that the radiance of an optically thin plasma represents the contribution of all the radiating elements which happen to lie in the line of sight. Therefore some caution must be exercised in ascribing the spatial origin of the spectral components observed. A third difficulty which must be kept in mind is that the spectroscopic information presented in this section was obtained with an open shutter over the length of the whole pulse and therefore it represents not only a line of sight integral as described before but a time integral as well. However, the time resolved photographs presented in the previous section show that the radiance downstream of the electrode-insulator junction remains constant over a large fraction of the pulse and that the duration of the transient phase of the discharge is sufficiently short so that hopefully its contribution to the photographic exposure can be neglected.

The instrument used in this study is a Steinheil GH 3-prism (glass) spectrograph with a linear dispersion of 5.4 $\mathring{A}$-mm^{-1} to 40.0 $\mathring{A}$ mm^{-1} over the range from 4300 to 6600 $\mathring{A}$. Its 650 mm f.l. collimator and a 640 mm f.l. camera lens have an effective f/.10. The optical arrangement used for the spectra taken at 22.8 cm downstream of the electrode insulator junction is shown in Fig. 4-9. Since both the accelerator and spectrograph are fixed, minor adjustments in the position of the lenses which image the whole height of the accelerator along the slit of the spectrograph are needed to obtain the spectra at other axial locations. The spectra were recorded on Royal - X Pan Kodak film developed with a procedure described in detail in Appendix B. The slit width used was 1.25×10^{-2} mm.

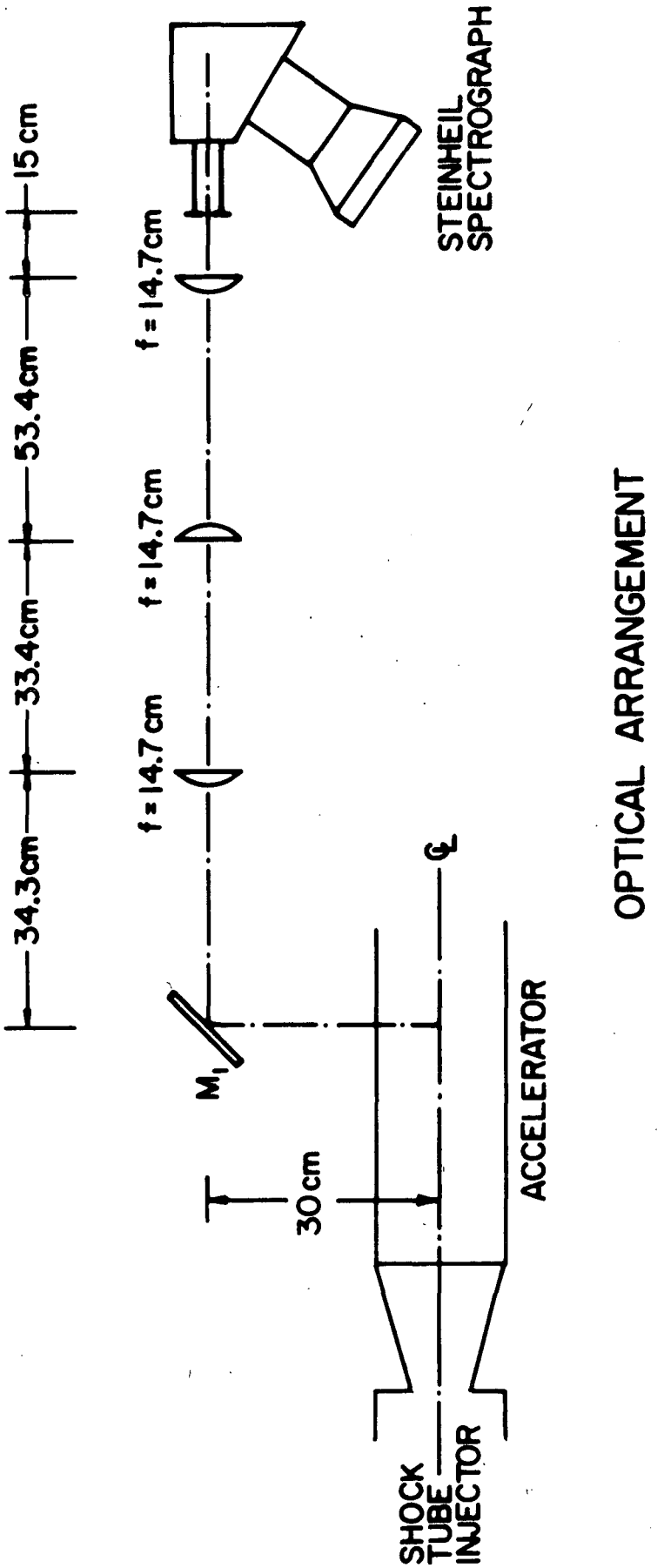

FIGURE 4-9
AP25 4789

The spectra of the discharge, taken at different axial locations for $I = 85$ kA and $\dot{m} = 96$ g sec^{-1} are shown in Fig. 4-10, These spectra cover the range from 4300 to 6500 Å. The top edge of each spectrum corresponds to the anode side of the channel while the bottom edge corresponds to the cathode side. Only the major components of the AII (singly ionized argon) as well as the major impurity lines which belong to hydrogen and molecular carbon are noted. The lines of AII dominate the spectrum of the discharge shown in Fig. 4-10a taken 10 cm upstream of the electrode-insulator junction.It is believed that this spectrum represents the quasi-steady portion of the pulse since the radiance of the luminous region associated with the transition phase of the discharge remains in front of the spectrograph slit for a time which is roughly equal to the width of the region divided by its velocity. Both these quantities can be estimated from photographs as the ones presented in the previous section. This time is approximately 5 cm/ 10^6 cm sec^{-1} which is roughly five microseconds while the length of the pulse is 210 μsec.

The spectrum taken at the electrode-insulator junction, Fig. 4-10b shows the AII lines as well as two distinct regions of continuum radiation attached to both electrodes as well as a darker region at the center of the channel just like that which appears in the photographs shown in Fig. 4-7. The spectral lines at this location are very broad, which might be the result of the high temperature, high pressure and high density environment which are believed to be present in this region. The spectrum shows asymmetry of some unidentified lines, some of which are broader at the anode side and some of which are broader at the cathode side. The bright region centered around the 4847.90 and the 4879.90 Å AII lines corresponds to the highly broadened H_β line (4861.33Å). This broadening, which is a function of electron density, will be discussed in more detail in the next section. The molecular carbon bands begin to appear at this position.

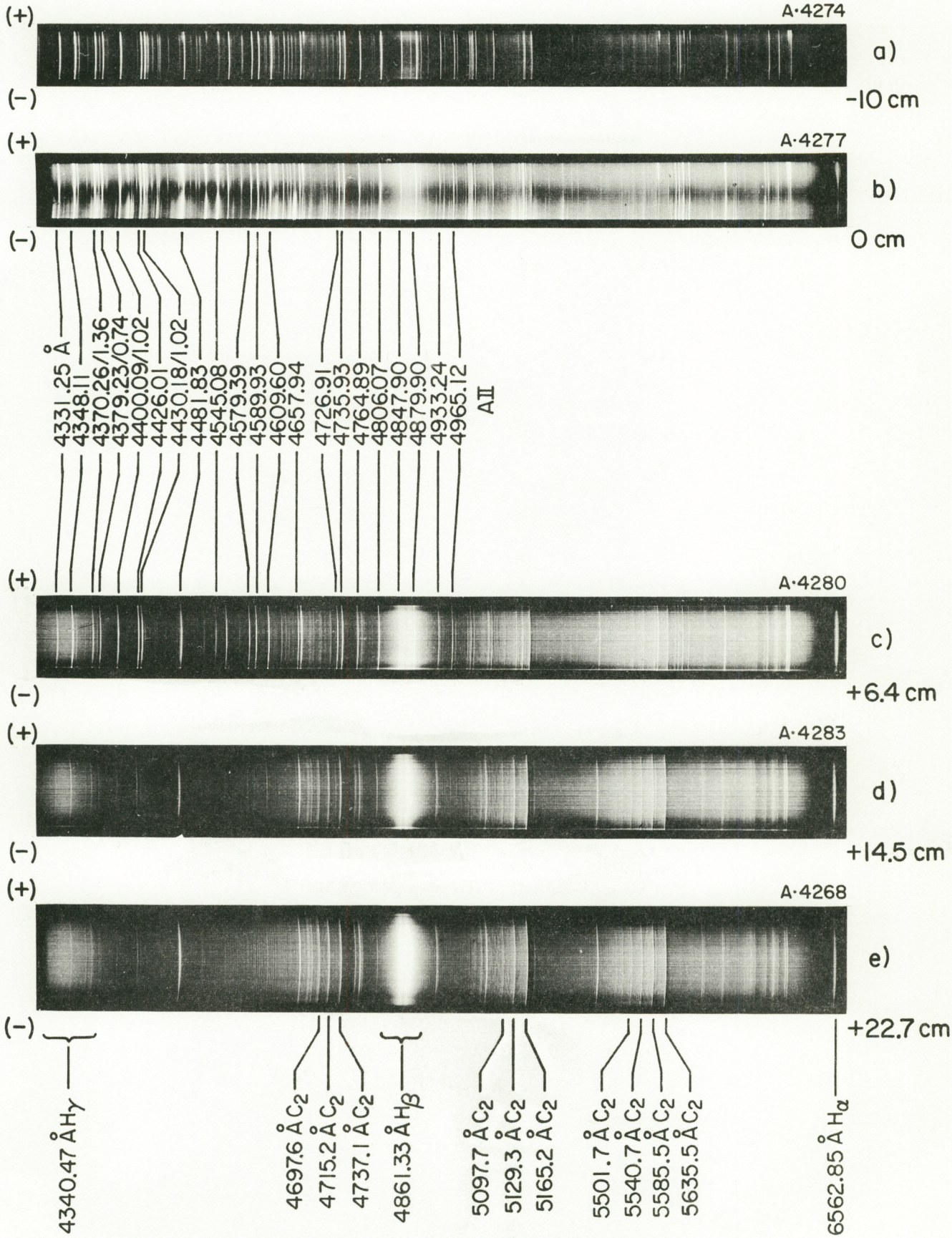

PARALLEL PLATE ACCELERATOR SPECTRA
$I = 85$ kA, $\dot{m} = 96$ g sec^{-1}

FIGURE 4-10
AP25 P408

Part c of the figures show the spectrum 6.4 cm downstream of the junction. The AII system is still very bright and dominates the spectrum. However, the H_α (6562.85 Å), H_β (4861.33 Å), and H_γ (4340.47 Å) lines are present. The H_β line is very broad and shows its characteristic dip in the center. The molecular carbon Swan bands are more prominent than at the previous position and occupy the whole height of the channel. Since the photographs presented in the previous section show that the radiance occupies the whole channel and originates in the flow, it is believed that the hydrogen and carbon are the product of the pyrolysis of the Nylon* and Plexiglas**[41] ablated from the accelerator channel. This material is carried downstream with the flow.

The spectrum corresponding to 14.5 cm downstream of the electrode insulator junction is shown in Fig. 4-10d. The radiance of the AII lines has decreased somewhat from the previous location while the radiance from the C_2 and H lines is roughly the same as at the 6.4 cm position.

The spectrum taken 22.7 cm downstream from the junction is shown in part (e) of the figure. In this spectrum the argon lines are quite dim and by now the spectrum is dominated by impurities. However, it must be noted that the width of the H_β line is roughly the same as in the previous spectra indicating that the electron density has not decreased significantly. This will be discussed in more detail in the following section.

b) <u>Electron Density Measurements</u>

The spectral lines of atomic hydrogen, present in the plasma as an impurity, can be used for the determination of electron densities in the discharge region and in the flow out of the acceleration region. The Stark broadening of the spectral lines of hydrogen, as a result of the interaction

* Nylon 66

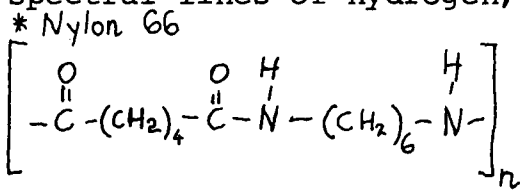

** Plexiglas

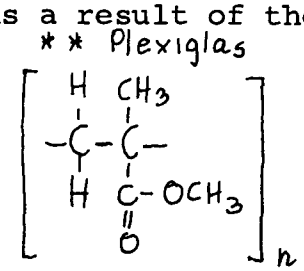

of the radiating atoms with electric fields originating in the surrounding ions and electrons,* is a direct function of the electron density. The quantum mechanical calculations which are used to determine the dependence of the width at half-intensity (half-width) of H_α and H_β on the electron density as well as experimental measurements to check the validity of the calculations are presented in Refs. 21 and 22. If $\Delta\lambda_s$ is the half-width of the H_β line (4861.33 Å) and n_e is the electron density, then, over the temperature range of 5×10^3 °K and 4×10^4 °K, (Fig. 4-11)

$$n_e = 3.3 \times 10^{14} \text{ Å}^{-3/2} \text{ cm}^{-3} \Delta\lambda_s^{3/2} \quad (4\text{-}5)$$

For this line, the agreement between the calculations and experimental measurements is very good which makes the measurement of its half-width one of the most accurate and convenient methods for the determination of electron densities in dense plasmas which contain hydrogen.

The electron densities in this accelerator are obtained from the half-width of the H_β line recorded photographically in spectra like the one shown in Figs. 4-10. Figure 4-12 shows the 4700 to 4960 Å region of the spectrum with the H_β line in detail. The characteristic central dip is due to the absence of an unshifted Stark component. Figure 4-12 also shows the transmission of the film at a location indicated by the arrow which corresponds to the midplane of the channel 22.8 cm downstream of the electrode insulator junction. This transmission was recorded in a Jarrel-Ash recording microdensitometer. The half-intensity point which is indicated in the densitometer trace is obtained by a procedure discussed in detail in Appendix B. This procedure hinges upon reproducible development of the photographic film.

*The effect of the field across the electrodes ($\sim 3 \times 10^4$ V m^{-1}) produces negligible broadening since fields in excess of 10^7 V m^{-1} are required to produce observable broadening in a discharge tube.[40]

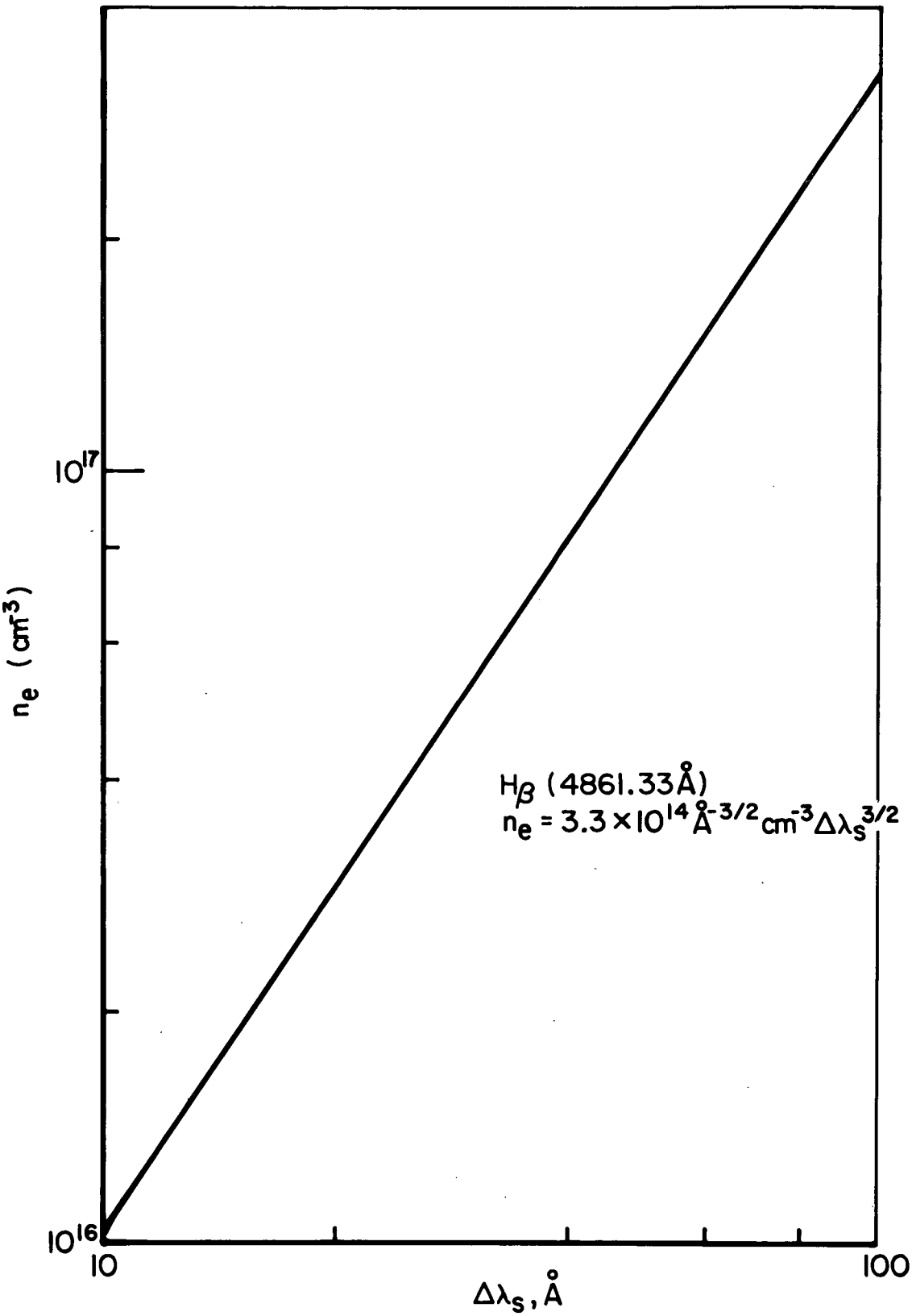

ELECTRON DENSITY AS A FUNCTION OF HALF WIDTH

FIGURE 4-11
AP25 4790

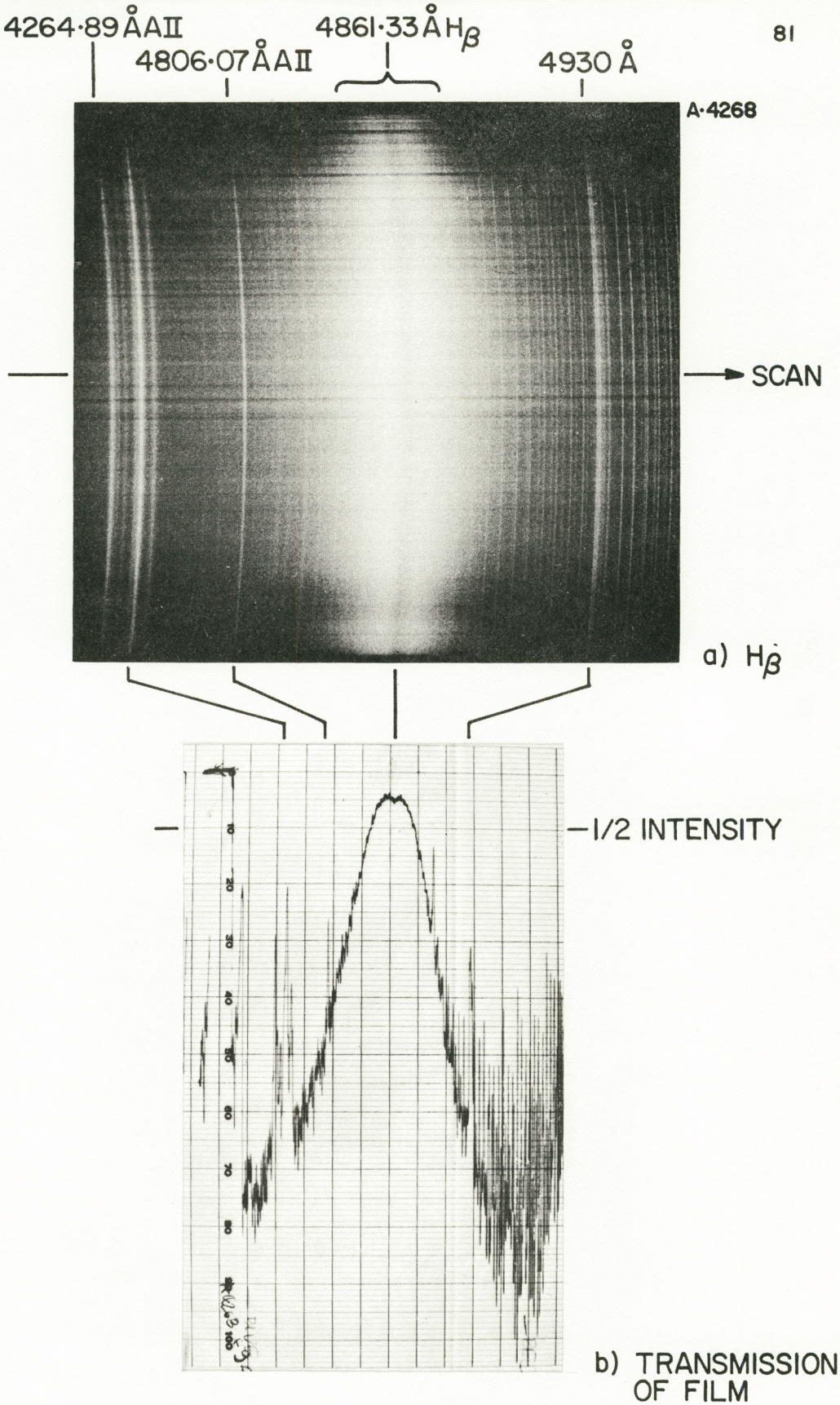

STARK BROADENING OF H_β, +22.7 cm
$I = 85$ kA, $\dot{m} = 96$ g sec^{-1}

FIGURE 4-12
AP 25 P 411

Electron densities across the height of the channel 22.7 cm downstream of the electrode-insulator junction obtained by successive scannings of H_β are shown in Fig. 4-13 for I = 57, 72 and 85 kA. The vertical position in the channel was determined from the known magnification of the system. The uncertainty in the vertical position is largest at the edges where the perspective effects are the greatest. This uncertainty is about 3 or 4 mm for the 22.8 cm axial position and less for positions further upstream. As has been discussed before, the radiance of the transition phase is neglected and the exposure is considered to be due to the quasi-steady portion of the discharge. The electron densities obtained by this method represent an average electron density over the line of sight. For the three currents shown, the electron densities are highest at the midplane and show a slight decrease towards the edges of the channel. The weak dependence of the densities upon the height of the channel is evidence that recombination at the channel walls is not extensive. Similarly, recombination at the sidewalls, would manifest itself by filling in the dip in H_β. Careful observation of the spectroscopic records indicates that this does not occur. The maximum electron density observed is 7.4×10^{22} m^{-3} for I = 89 kA and the lowest 3.7×10^{22} m^{-3} for I = 57 kA. The uncertainty which is believed to arise in the reduction of the photographic data and which also represents the scatter of data obtained from different spectrograms is represented by the error brackets. This uncertainty is of the order of 15 or 20%. Unfortunately, it was not possible to carry an absolute calibration of the system so that the possibility of systematic errors is not completely ruled out.

Electron density contours in the accelerator can be obtained from profiles, such as the ones shown above, taken at different axial locations. These contours, for I = 85 kA

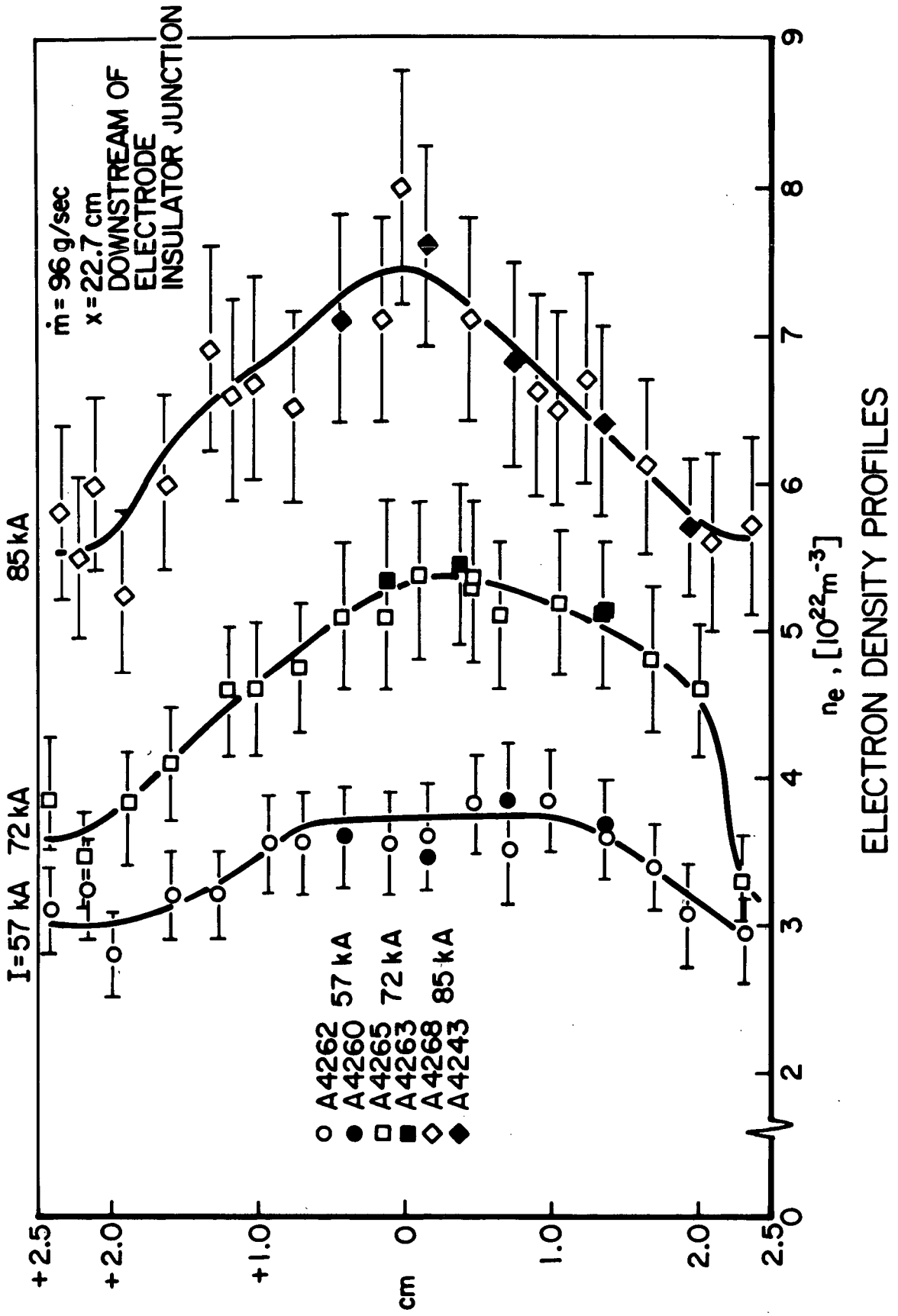

FIGURE 4-13
AP25 4762

and $\dot{m}$ = 96 g sec $^{-1}$, for the region downstream of the electrode-insulator junction are shown in Fig. 4-14. The data for these contours were taken at the electrode-insulator junction and 6.3, 14.5, and 22.7 cm downstream of it. In the figure, the height of the channel is shown in an expanded scale. The electron density is highest at the cathode side of the electrode-insulator junction. At the midplane, the electron density maximum is reached about one channel height downstream of the junction at roughly the same location where the two radiance zones discussed in Sec. 4-4 meet. In the following 15 cm., it drops roughly by 20% from 9.5×10^{22} m $^{-3}$ to 7.4×10^{22} m $^{-3}$.

c) Velocity Measurements

The measurement of velocities downstream of the acceleration region is desirable for several reasons:

a. It participates directly in any momentum and energy balance calculation.
b. It is necessary to compute the motional emf V_{uB}
c. It is the most interesting quantity from a propulsion standpoint.

From a conceptual standpoint, the simplest technique for measurement of velocities takes advantage of the so-called Doppler effect. This effect consists of an apparent wavelength change of the radiation emitted from a particle moving towards or away from an observer. If the velocity component in the direction of the observer is u_s, the fractional wavelength change $\Delta\lambda/\lambda$ is, for $u_s \ll c$,

$$\frac{\Delta\lambda}{\lambda} = \pm \frac{u_s}{c} \tag{4-6}$$

where c is the velocity of light. The plus and minus signs apply to particles receding and approaching the observer respectively.

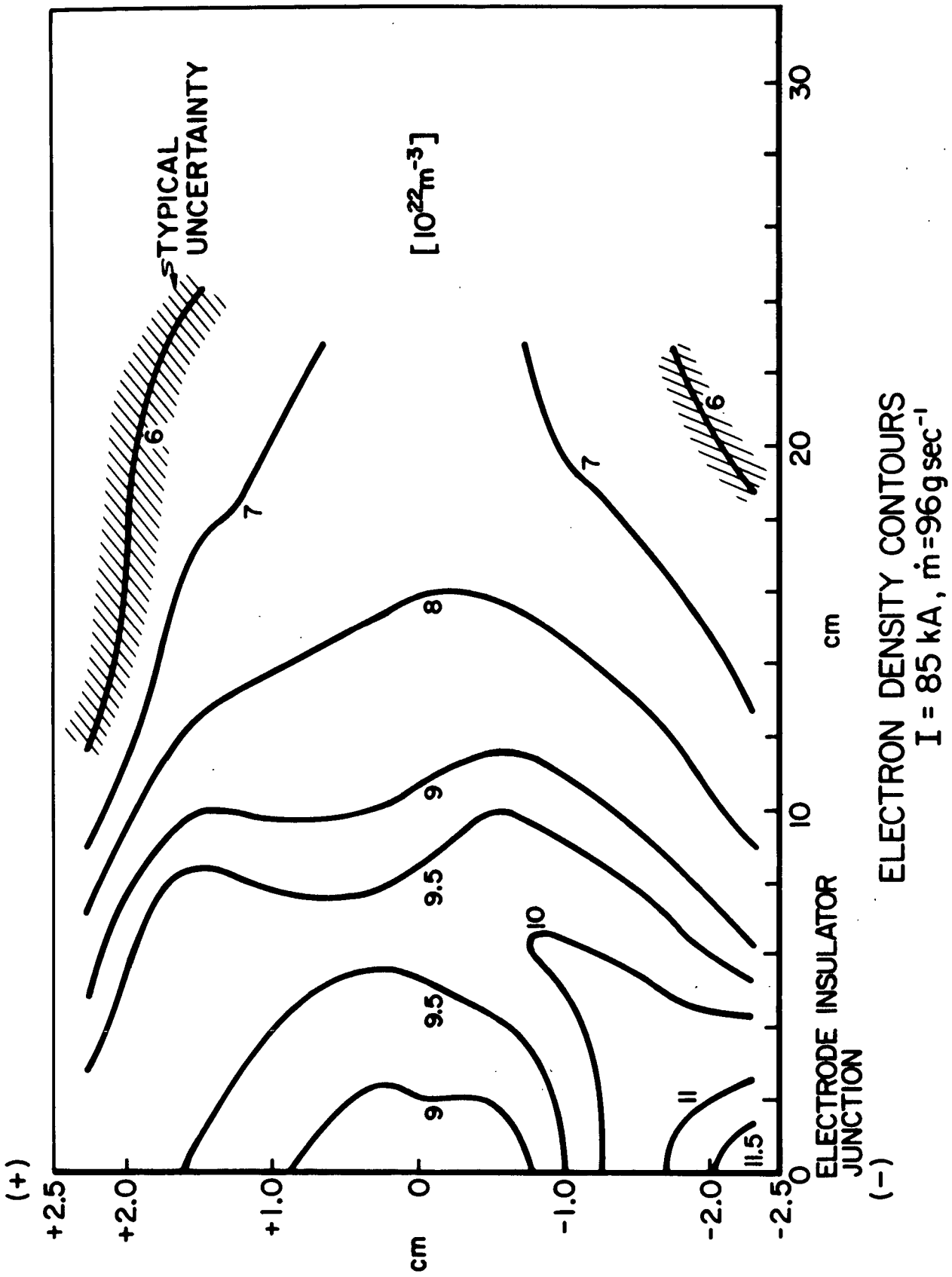

FIGURE 4-14
AP25 4767

The experimental arrangement used for this measurement, shown in Fig. 4-15, is very similar to the one described earlier in this section. It employs the Steinheil spectrograph with a slit width of 1.25×10^{-2} mm to compare the Doppler shifted spectra observed along the two lines of sight through a common point in the plasma. One of the lines of sight makes an angle of 51° with the flow direction while the other makes an angle of $\pi - 51^{\circ}$. The common point lies in the centerline of the accelerator, 22.4 cm downstream of the electrode-insulator junction. The spectra, therefore, represent light radiated along two paths which are oblique to the flow. One originates at the right edge of the channel 6 cm upstream of the common point and terminates 6 cm downstream of it at the left edge of the channel. The other originates 6 cm upstream of the common point at the right edge of the channel and terminated 6 cm downstream of it at the left edge.

The shifts were measured from the photograph for the 4348.11 Å and 4426.01 Å AII lines using a comparator capable of measuring $\sim 5 \times 10^{-4}$ mm. The measured shifts on the film are typically of the order of 2×10^{-2} mm which, with a linear dispersion of the order of 6 Å mm^{-1} at the blue end of the spectrum result in fractional wavelength shifts of 2.7×10^{-5}. These shifts correspond to relative velocities of 8.1×10^{3} m sec^{-1} which, when divided by twice the cosine of the angle correspond to velocities of $5\text{-}6 \times 10^{3}$ m sec^{-1}.

The axial velocities are displayed as a function of current in Fig. 4-16 for $\dot{m} = 96$ g sec^{-1}. Each point represents the average of measured velocities from several plates reduced from the two argon lines mentioned above. All the averaged values are contained within the error bars. The

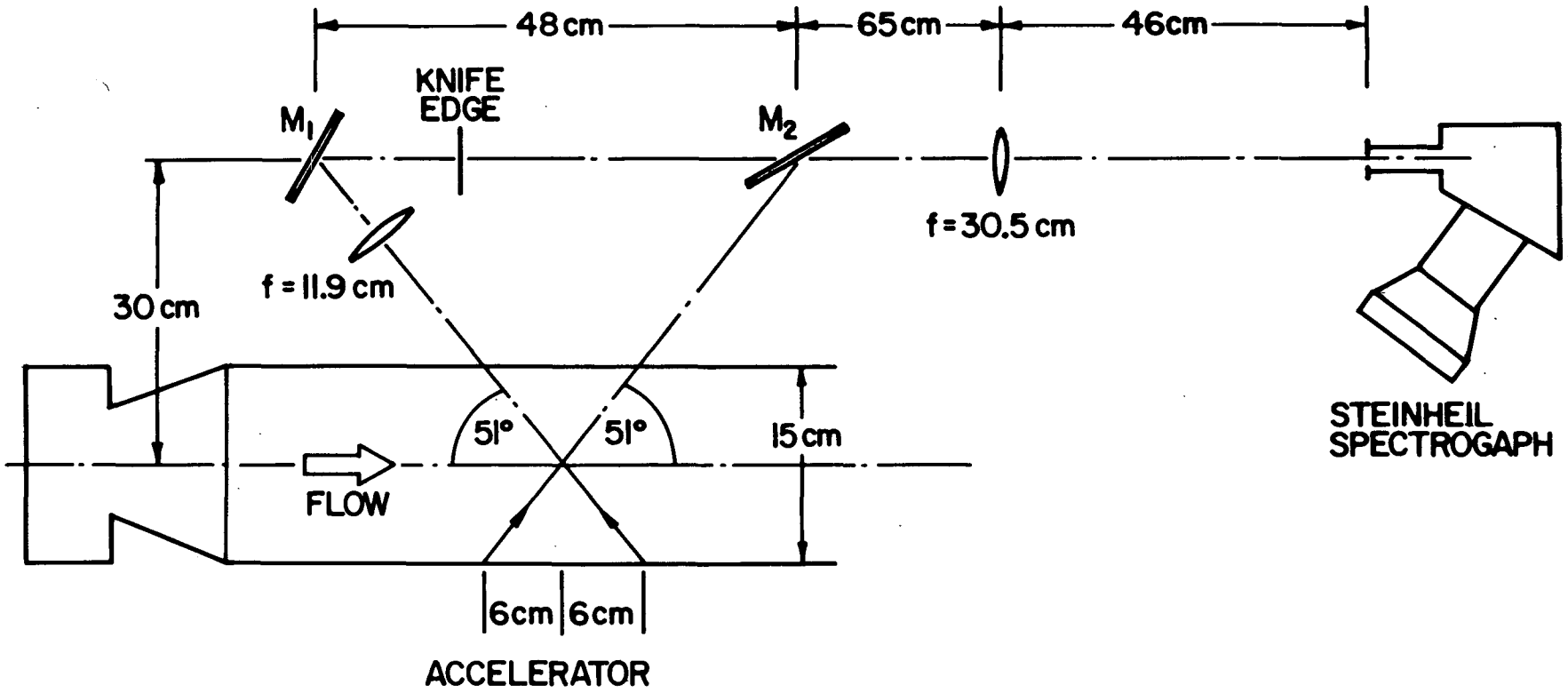

FIGURE 4-15
AP25 4781

DOPPLER SHIFT MEASUREMENT

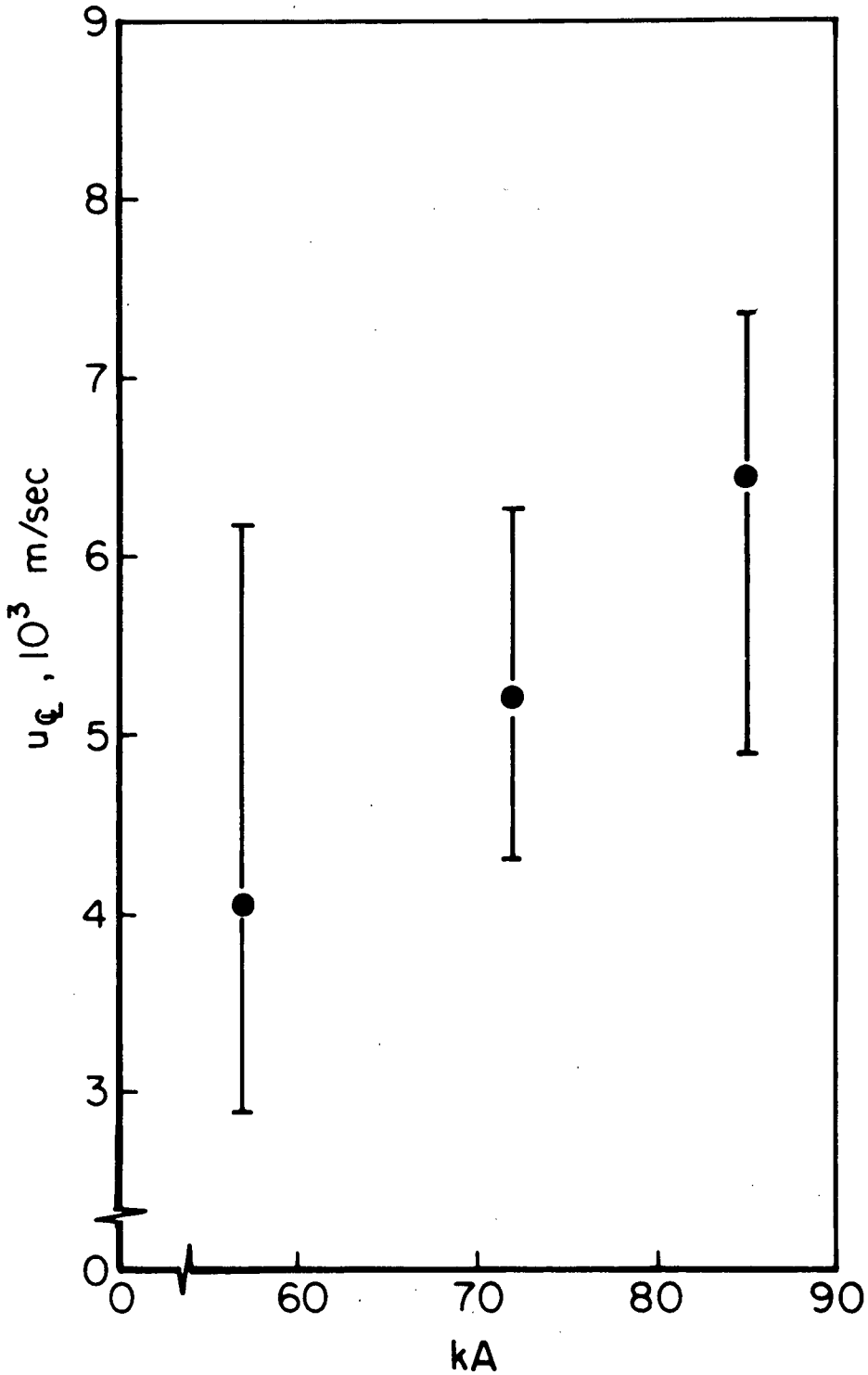

VELOCITY AS A FUNCTION OF CURRENT, $\dot{m}$ = 96 g/sec

FIGURE 4-16
AP25 4766

The same considerations which were introduced in the interpretation of the electron density data from the Stark broadening of H_β apply here as well; namely, the radiance of the plasma originates and coincides with the quasi-steady portion of the discharge. It is, therefore, reasonable to assume that the measured velocities correspond to the velocities which prevail during the quasi-steady phase. The measurements also represent an average of the velocity weighted by the radiance associated with the plasma along the line of sight. There is no direct way to assess the effect of slower fluid along the walls. However, an elementary boundary layer calculation presented in Chap. 5 shows that the thickness of the boundary layer is small compared to the width of the channel and the photographs displayed in Sec. 4-3 and 4-4 do not show any bright region at the edge of the channel. Therefore, it is reasonable to assume that the effect of the fluid near the walls is small.

The large error bars in the graph in Fig. 4-16 are associated with the uncertainty which arises in reading the data from the spectral lines. The source of the uncertainty is the width of the lines of the two spectra which are being compared. This width is a combination of the slit width of the instrument ($\sim 10^{-2}$mm) and the Stark and Doppler broadening of the spectral lines in the plasma environment. These considerations discouraged the application of this technique for velocity measurements at other locations in the accelerator where the spectral lines are noticeably broader as indicated by the spectra presented in Fig. 4-10.

4-6 WALL PRESSURE MEASUREMENTS

To establish the momentum balance of the flow and to determine the thermodynamic state of the fluid, it is desirable to measure the static pressure in the flow. In this geometry, it is reasonable to assume that the static pressure and wall pressure outside of the current distribution

2

are identical due to the absence of accelerating forces in a direction perpendicular to the channel wall. In the region of the current distribution, wall pressure measurements might yield some useful information about the acceleration mechanisms present.

a) The Pressure Probe

The pressure on the wall of the channel was determined with a fast response pressure probe described in detail in Ref.[23]. Some of the details of the probe are shown in Fig. 4-17. It consists of a piezoelectric transducer element bonded between two Plexiglas rods. On one side of the transducer element, a 5 cm-long stub is used to transmit the pressure signal from the plasma to the transducer. On the other side of the element, a 96 cm-long backing rod provides an acoustical delay line such that a stress wave (pressure signal) impressed at the transducer end of the backing rod takes roughly 1 msec to return after reflection at its free end. (The acoustic speed in Plexiglas is 2100 m sec^{-1}). The transducer is surrounded by a thin copper shroud which provides an electrostatic shield. The stub, which is covered with reflective silver paint, isolates the transducer element both thermally and radiatively from the plasma. A soft covering of Epoxy resin serves to keep the plasma away from the outer shield and electrical connections. The transducer, which produces a charge output that is directly proportional to pressure is connected to a Kistler 565 charge amplifier with an input impedance of $10^{12}\ \Omega$ and a risetime of 7 μsec. This amplifier delivers an output voltage which is proportional to the charge deposited at its input. Therefore, the whole system produces a voltage which is directly proportional to pressure. The experimental arrangement is shown in Fig. 4-17. The pressure probe is located inside a 7 cm-ID Plexiglas tube which is mounted vertically on the channel sidewall through a Nylon fitting. In this way, the tube forms an integral part

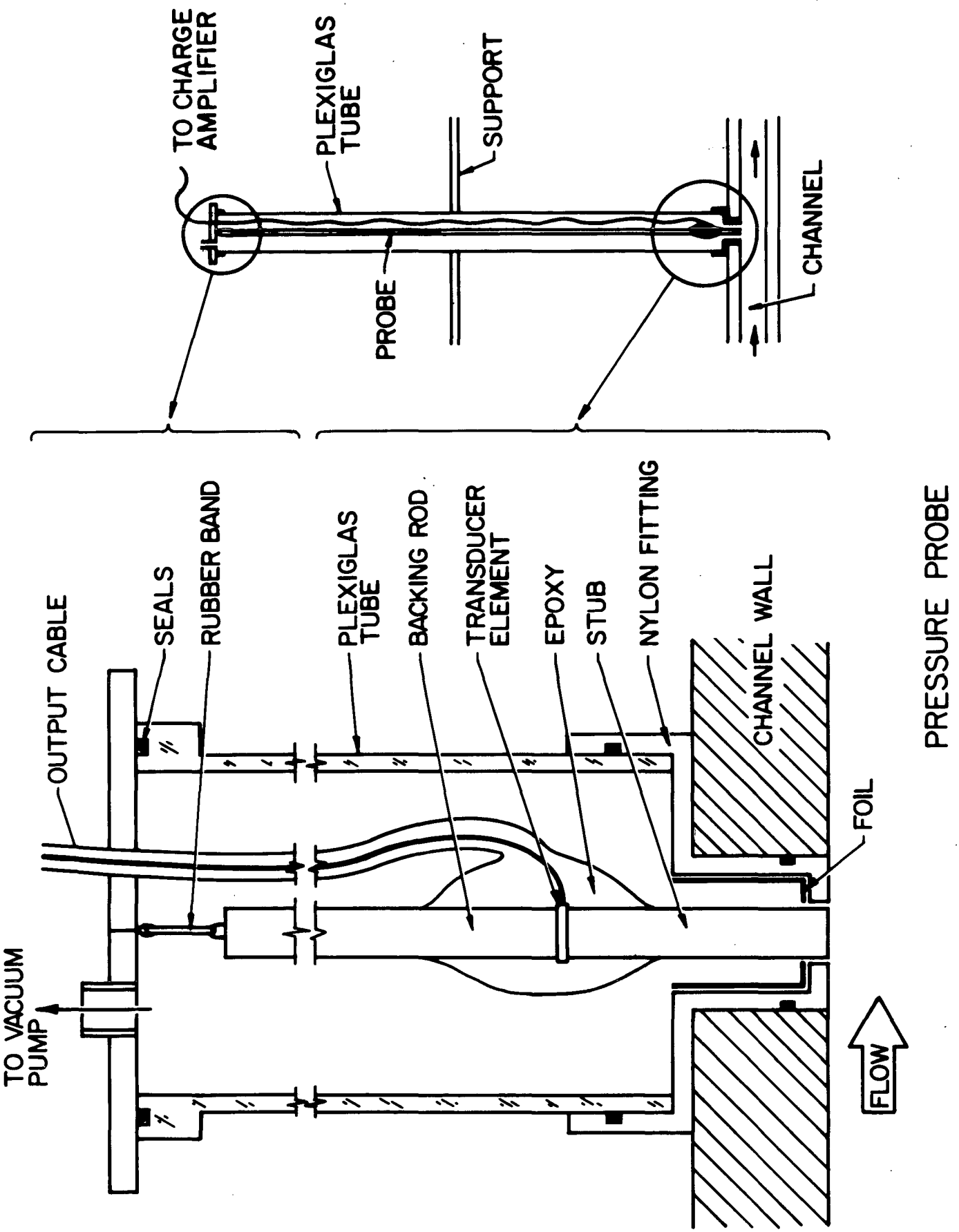

FIGURE 4-17
AP25 4757

of the accelerator vacuum system and isolates the probe acoustically from the laboratory environment. It also eliminates the requirement of a seal between the probe and the channel wall which would certainly introduce unwanted acoustical noise. A 1.6 mm annular clearance is provided between the stub (9.5 mm OD) and the hole (12.7 mm ID) in the Nylon fitting. The probe is suspended in the tube by an elastic suspension attached to the end of the backing rod. This suspension isolates the probe from vibrations originating in the building and experimental apparatus. The probe is accurately positioned so that the end of the stub is flush with the channel wall and the probe does not touch the fitting or any other part of the experimental apparatus. To shield the probe from the plasma radiation, the fitting is covered with silver paint and aluminum foil. The probe is connected to the charge amplifier via 15 feet of 50 Ω RG-174 A/U coaxial cable. The charge amplifier is located in the same screen room as the Tektronix 555 oscilloscope used to record the signal from the pressure probe-amplifier assembly.

b) Probe Response and Calibration

The probe must be calibrated to obtain reliable pressure measurements in the plasma. It is necessary to establish the voltage output for a given pressure and to establish that this voltage is linear and independent of frequency over the anticipated pressure range. The calibration procedure for this pressure probe has been described in detail in Ref. 23 and is summarized briefly in this section. To obtain the voltage output for a given pressure, the probe is loaded axially with a known weight and the voltage output is measured as the weight is quickly removed. This is called the yanked-weight calibration. A triple overlay of the voltage obtained by balancing a 200 g weight on the probe stub, with the end of the backing rod resting on the floor, and quickly removing it with a string is shown in Fig. 4-18a. The oscilloscope is triggered manually just before the weight is removed.

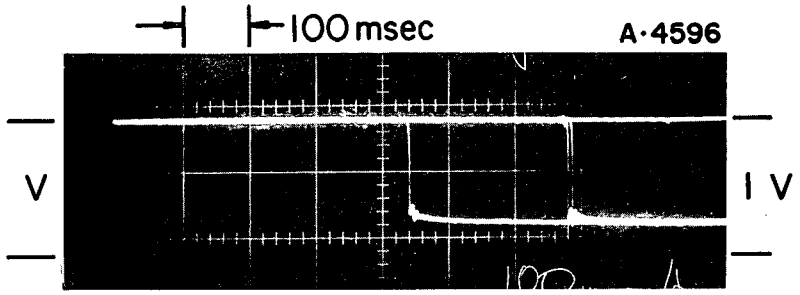

a) YANKED WEIGHT CALIBRATION
200 g, 1000 pF FEEDBACK CAPACITOR

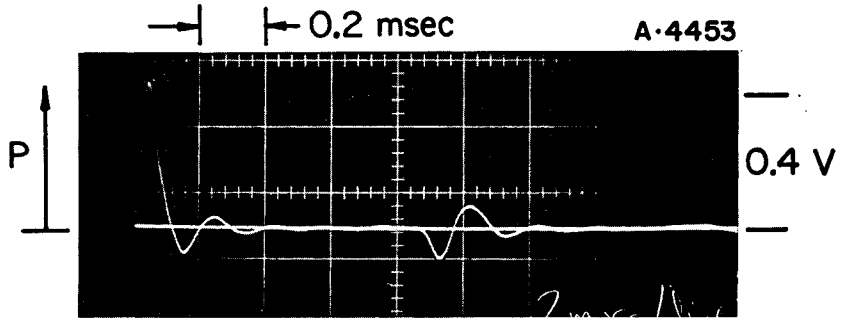

b) PENDULUM TEST

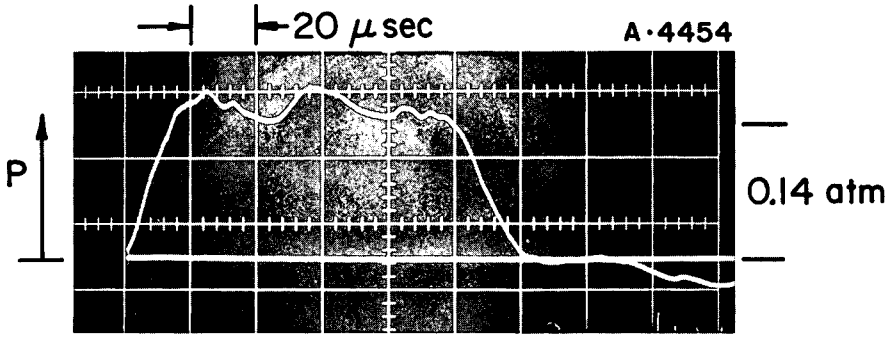

c) SHOCK WAVE TEST

PRESSURE PROBE CALIBRATION AND RESPONSE

FIGURE 4-18
AP25 407

The reproducibility, which is quite good, strongly depends on maintaining the probe perfectly vertical and accurately centering the weight in a way such that the rod does not bend. The results from a series of tests with weights of 20,50,100,200, and 500 g are summarized in Fig. 4-19. Since the area of the probe is 0.726 cm^2, the calibration constant of the probe is (0.344 ± .02) atm V^{-1} with a 1000 pF feedback capacitor in the charge amplifier, and (0.172 ± .02) atm V^{-1} with a 500 pF capacitor. The error bars in the graph represent the scatter in the data due to the difficulties in keeping the probe vertical and the weight centered. The 500 g weight corresponds to a pressure of 0.7 atm which is about one-half of the maximum pressure measured in the accelerator. However, this is the largest weight which could be balanced successfully on the probe without bending it. On the basis of the excellent linearity of the response, it is reasonable to expect that the calibration constant mentioned above is also valid in the 0.7 - 1.4 atm range. To establish that the response of the probe to the slow (several msec) changes in stress which are caused by removing the weight accurately reflect its response to the rapid pressure changes in the plasma, Cory, in Ref. 23, has calibrated the probe with a more laborious shock tube technique. This technique, within experimental error, yields the same results as the ones obtained with the yanked weight technique described above. Therefore, the calibration factors shown above are the ones used for the measurement of wall pressure in the accelerator.

The response of the probe can easily be established by two simple tests. One is the pendulum test which serves to demonstrate the long-time response (1 msec or less) and the other is the shock wave test which illustrates the behavior of the probe on a short time scale (20 μsec or less). In the pendulum test, the probe is struck with a 3.1 mm steel ball suspended from a 15 cm-long thread. This pendulum is

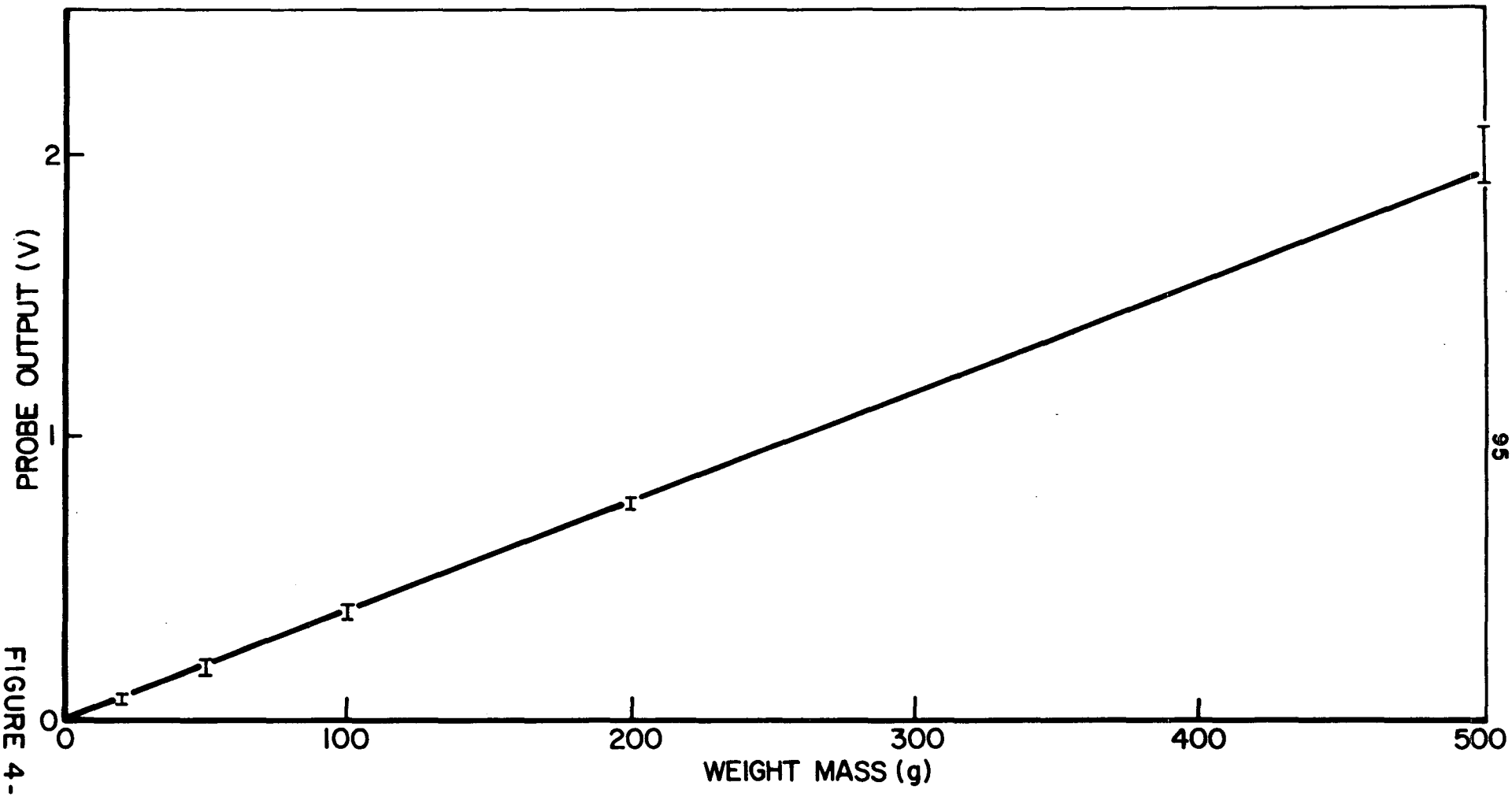

FIGURE 4-19
AP25 4761

YANKED WEIGHT CALIBRATION OF PRESSURE PROBE
(1000 pF FEEDBACK CAPACITOR)

used to induce an impulsive stress in the probe. For the test, the ball is held 1 cm away from the probe face and then released. The ball strikes the face of the probe and rebounds after about 50 μsec. This time is determined by the nature of the impact and the velocity of the stress waves induced in the ball. Due to the long period of the pendulum (700 msec) the ball remains away from the probe for the duration of the test (~2 msec). The voltage output of the probe and charge amplifier, resulting from this impulsive stress is shown in Fig. 4-18b. The first peak with an approximate duration of 100 μsec is due to the ball striking the face of the probe and rebounding. The second peak, which is negative is probably due to an acoustical inhomogeneity present in the stub-transducer-backing rod interface. After about 200 μsec, the long flat region indicates that all detectable stresses have propagated into the backing rod. The stress wave reflects as a tension wave at the free end of the backing rod and arrives at the transducer after 0.95 msec. By this time, the pulse is broadened and attenuated due to imperfections in the rods and interfaces. Therefore, this particular probe is useful for measurements which last less than 1 msec. After this time, the voltage output no longer is a simple function of the applied stress, except perhaps for measurements which last long enough to allow the internal reflections to subside. Due to the finite time associated with the rebound of the pendulum, this test does not provide any information about the risetime of the probe.

The risetime of the probe is established by subjecting the end of the stub to a shock wave in air. This shock wave, was generated by firing a toy cap gun into one end of a 1m-long, 5 cm-ID tube and placing the stub of the probe facing the other end of the tube. The oscillogram of the resulting

pressure wave is shown in Fig. 4-18c which shows a risetime of 16 μsec. This is estimated to be the risetime of the probe and amplifier assembly since the risetime of the shock is at most a few μsec.

c) Results

To obtain a reliable measurement of pressure on the wall, the streamlines of the flow along the wall must remain undisturbed. To this end, in the measuring arrangement used, the probe face is accurately positioned so that it is flush with the face of the channel wall. The effect of the 1.6 mm wide annular space around the probe, shown in Fig. 4-17, is difficult to assess accurately. However, it is believed to be small -- since its area is a small fraction of the area of the probe. To estimate the effect of this annulus in a similar measurement in the chamber of an MPD accelerator,[23] the annular space was filled with a plastic sponge to block leakage around the probe. It was found that although the acoustic noise increased, the pressure indication did not change. It was, therefore, concluded that the effect of the annular space on the measurement is negligible.

Figure 4-20 shows pressure records obtained at 4 axial locations on the centerline of the channel wall (anode side) for I = 57 kA and $\dot{m}$ = 96 g sec^{-1}. The locations are 10 cm upstream of the electrode-insulator junction, denoted by -10 cm and 2.5, 6.3 and 22.4 cm downstream of it, denoted by +2.5, +6.3 and +22.4 cm respectively. The last record in the figure corresponds to the 22.4 cm axial position 5 cm off the centerline. As a reference, current and voltage records obtained with the techniques described in Sec. 4-2 are shown in Fig. 4-20a. The same measurements for I = 72 and 85 kA are shown in Figs. 4-21 and 4-22 respectively. Since the stub introduces a 25 μsec acoustical delay in the pressure signal, the pressure records are displaced in the figure by the equivalent of 25 μsec. An estimate of the repeatability of the measurements is given by the triple

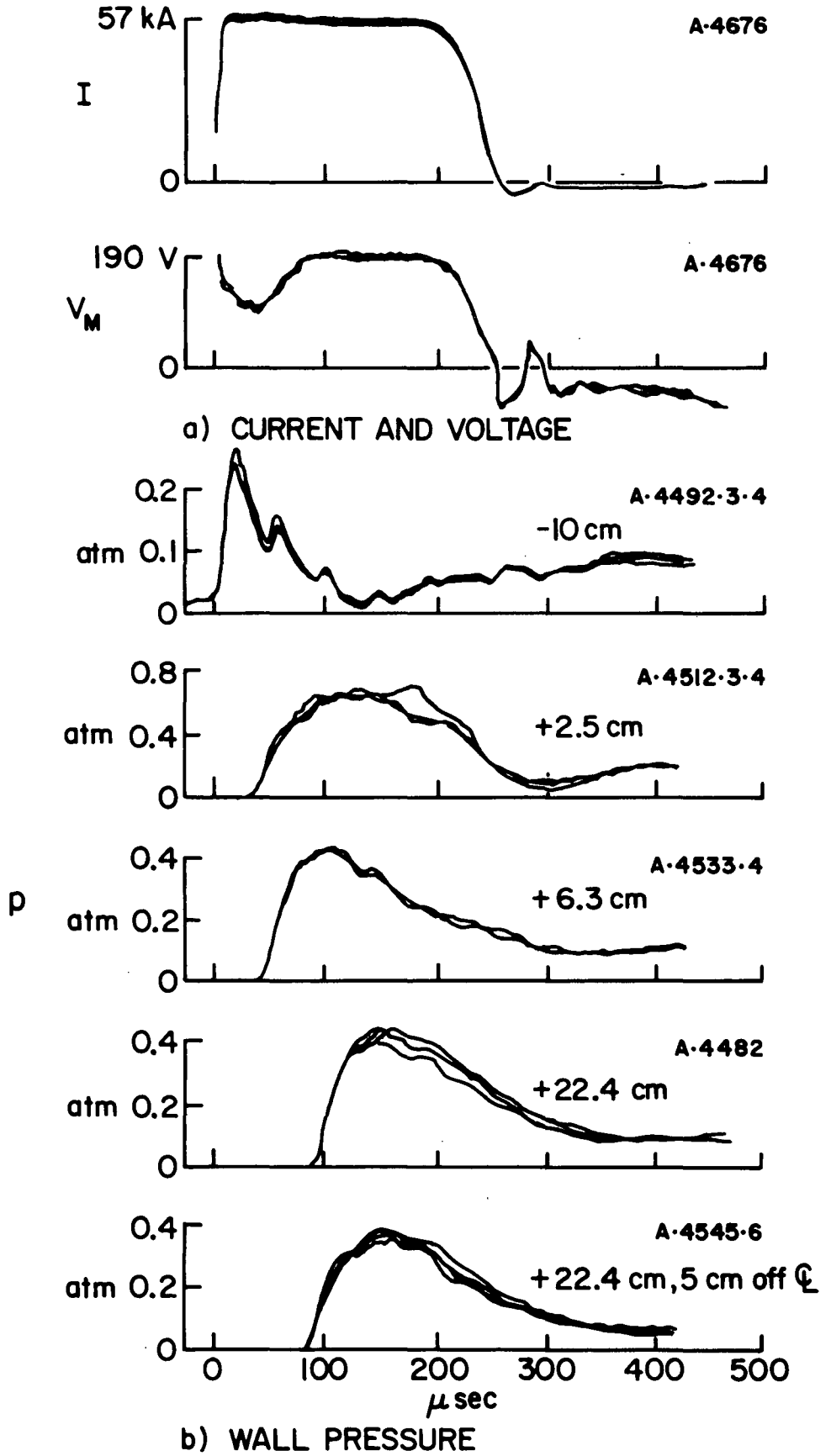

b) WALL PRESSURE

PRESSURE MEASUREMENTS
$I = 57$ kA, $\dot{m} = 96$ g sec^{-1}

FIGURE 4-20
AP25 4758

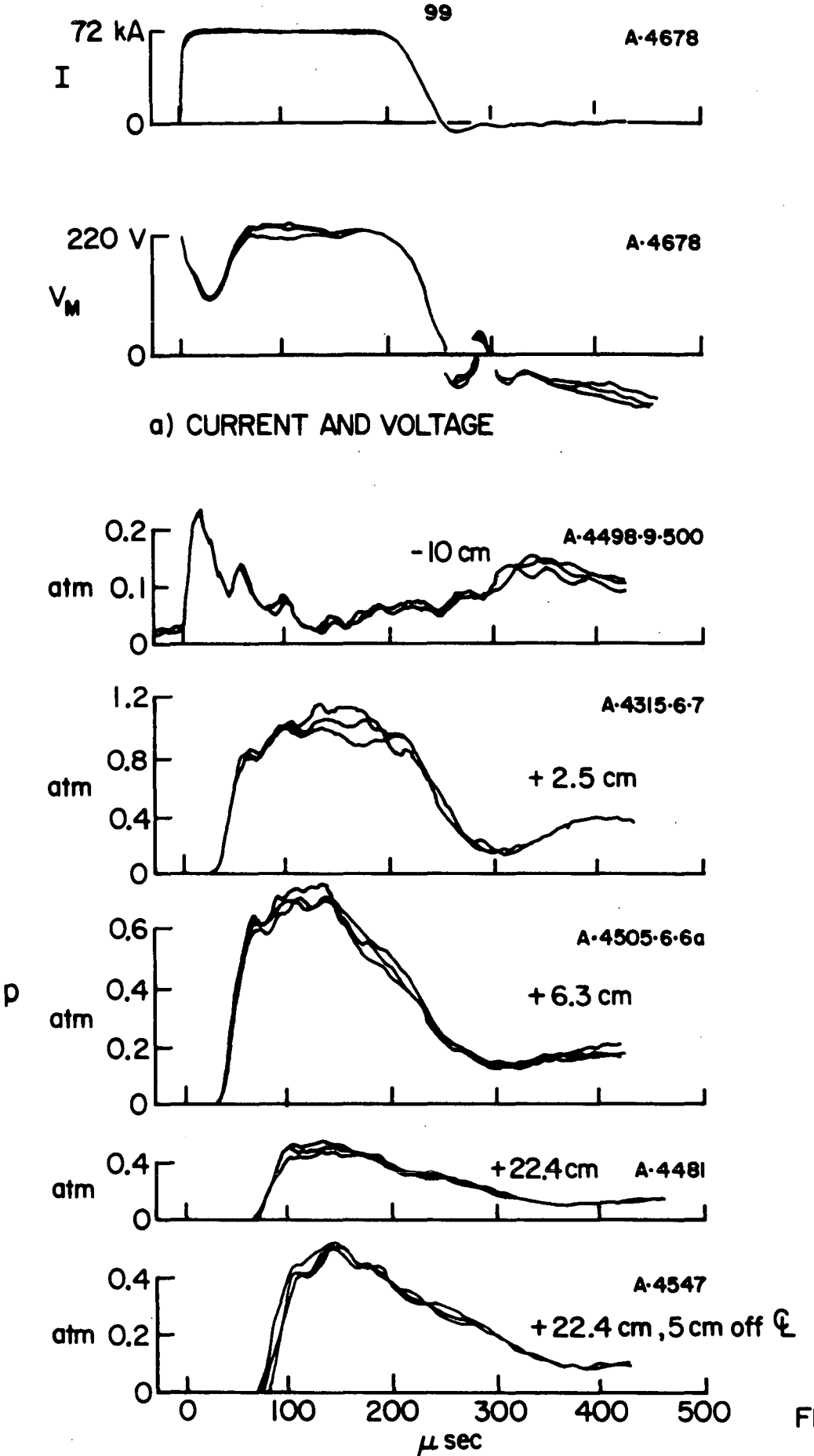

FIGURE 4-21
AP25 4760

PRESSURE MEASUREMENTS, I = 72 kA, $\dot{m}$ = 96 g sec^{-1}

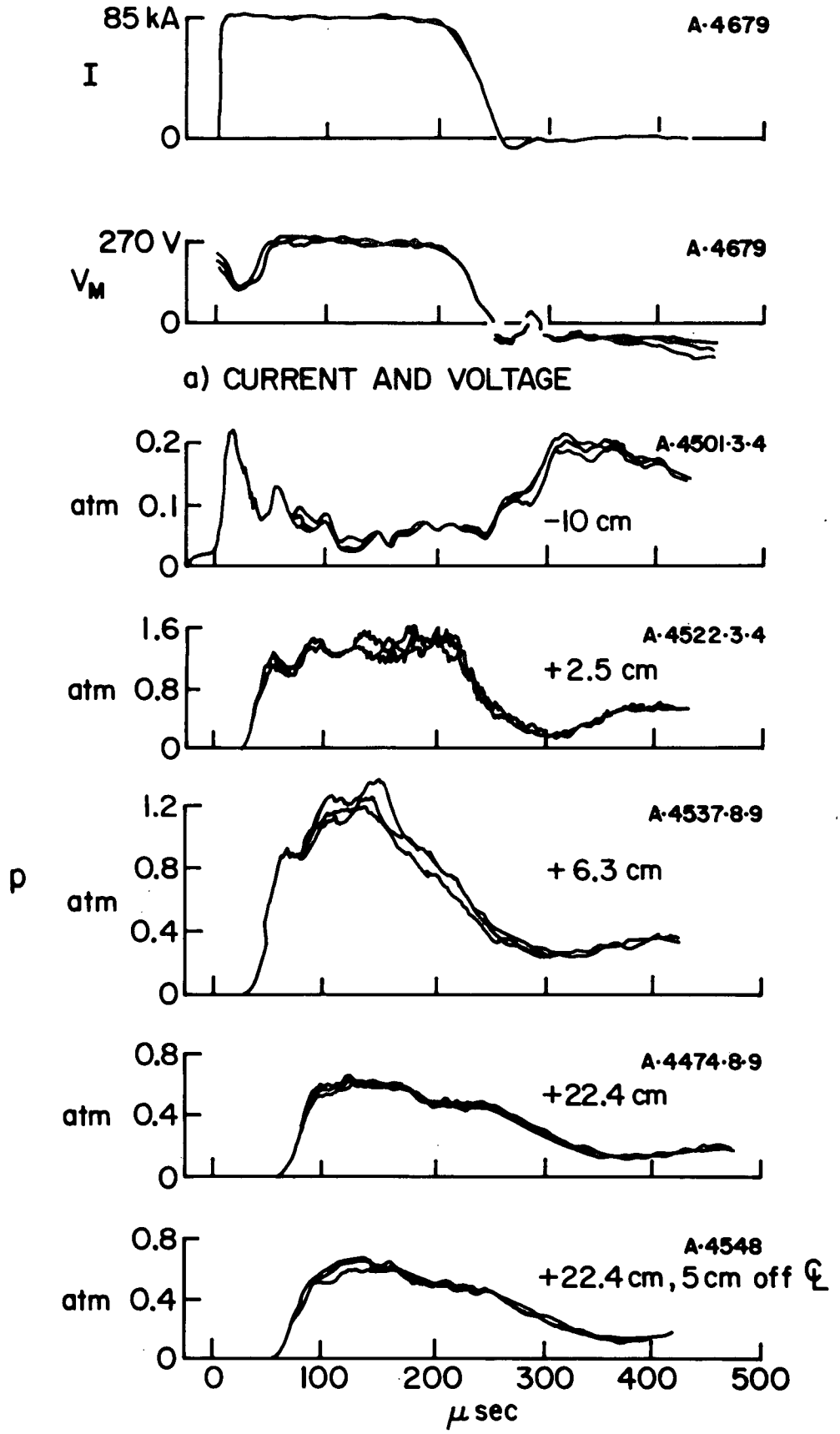

b) WALL PRESSURE

PRESSURE MEASUREMENTS
$I = 85$ kA, $\dot{m} = 96$ g sec^{-1}

FIGURE 4-22
AP 25 4759

overlays displayed. The records show that there is no detectable acoustic or electromagnetic noise present during the current pulse. This noise, if present, would appear in the baseline of the oscillograms. This is confirmed by firing the machine with the probe orifice closed with Mylar tape. The record shows a noise level equivalent to 9×10^{-4} atm - which is negligible with respect to the pressure measured in the course of the experiment.

The pressures measured at -10 cm are remarkably similar for all three current levels. The initial displacement from the baseline is due to the cold flow in the accelerator. A peak of about 0.2 atm appears some 20 μsec into the pulse. It is believed that this pressure peak is associated with the propagation of the current distribution towards the electrode-insulator junction. The other two peaks most probably originate from internal reflections in the probe stub. The pressure then drops to a low value of 0.01 - 0.02 atm for the rest of the pulse. Measurements 2.5 cm downstream of the junction (+ 2.5 cm) show a high pressure region with a maximum of 0.65 atm for I = 57 kA and 0.97 and 1.3 atm for I = 72 and 85 kA respectively. These high values are not surprising. The photographs of the discharge region presented in Sec. 4-4 suggest that the discharge region is convected downstream by the flow, thereby tilting the current distribution towards the walls of the channel (Fig. 4-23), a result later confirmed by measurements of the magnetic field. This tilt introduces a component of the $\vec{j} \times \vec{B}$ body force in the y direction $(\vec{j}_x \times \vec{B}_z)$ which gives rise to a pressure gradient along the height of the channel. The high pressures measured at this axial location are believed to originate with this pressure gradient. The quadratic dependence on the discharge current of the wall pressure at this location is further evidence of its electromagnetic origin. It is interesting to note that, for all three current levels investigated, the pressure at + 2.5 cm follows the steady portion of the voltage

trace very closely. This is especially true for 85 kA pulse in which the pressure and voltage achieve a steady value simultaneously which lasts over the whole pulse. The pressure at +6.3 cm is lower for all three current levels and its value is about 0.4 atm for I = 57 kA and 0.7 atm for I = 72 kA. At this location, the pressure is 1.1 atm for I = 85 kA. At this current level, the pressure drop between + 2.5 cm and + 6.3 cm is lower -- probably because the current distribution extends the farthest downstream. All the pressure records at this location show a sharp leading edge and the trailing edge shows the more gradual pressure drop typical of a rarefaction. At + 22.4 cm, the pressure for I = 57 kA is 0.3 atm. For I = 72 kA, the pressure at this position is 0.4 atm and for I = 85 kA, the value is 0.45 atm. The records again show the sharp leading edge and the gentle slope associated with the rarefaction. The measured pressures on the centerline at + 22.4 cm and 5 cm off the centerline at the same axial position are identical. Therefore there is no acceleration of the flow perpendicular to the axis of the channel. The velocity of the plasma can be estimated roughly from the arrival of the shoulder of the pressure wave at the different axial locations. These velocities about 5×10^3 m sec^{-1}.

4-7 MAGNETIC FIELD MEASUREMENTS

Magnetic field measurements are useful to establish some general characteristics of the current distributions within the accelerator. The technique used for these measurements employs a standard magnetic probe,[24] consisting of a small coil insulated from and immersed in the plasma. This coil delivers a signal which is proportional to the time rate of change of magnetic flux threading its opening. Passive integration of this signal provides a history of the magnetic field at the location of the probe. Through the use of Ampere's Law, and the one-dimensional assumption,

these measurements can be transformed directly into the current which flows downstream of the location of the probe. The probe was calibrated by placing the coil in the space between the 15.1 cm-wide conductors which feed the accelerator in the same approximate location as the current pickup coil described in Sec. 4-2. The magnetic field at this location can be calculated by using Ampere's Law and the 1-D approximation. The calibration factor for the probe is derived by comparison of the integrator output and the magnetic field at the probe location calculated from the known current.

The experimental measurements are shown in Fig. 4-23. This figure displays the ratio B/B_1 during the quasi-steady portion of the discharge at different locations in the discharge region for I = 85 kA. The measurements were performed by keeping the probe in the centerline of the channel and changing its height. As in the case of the electron density contours presented in Fig. 4-14, the height scale in the figure has been expanded. B_1 is the calculated magnetic field at the rear wall of the channel which is taken to be identical to the calibration magnetic field since the width of the channel and the width of the current feeder conductors are identical. For a strictly one-dimensional geometry, the ratio B/B_1 is equivalent to the ratio I/I_1 where I_1 is the current in the circuit and I is the current which flows downstream of the probe location. The negative values of B/B_1 cannot be interpreted as a negative current. They are merely a consequence of 2-D effects due to the finite width of the channel. The dotted line shows roughly the location of the contour of zero magnetic field which would correspond in the ideal case to the farthest downstream excursion of the current distributions. The figure shows that: (a) about 25% of the current flows upstream of the -10 cm location near the rear wall and, (b) the downstream extension of the

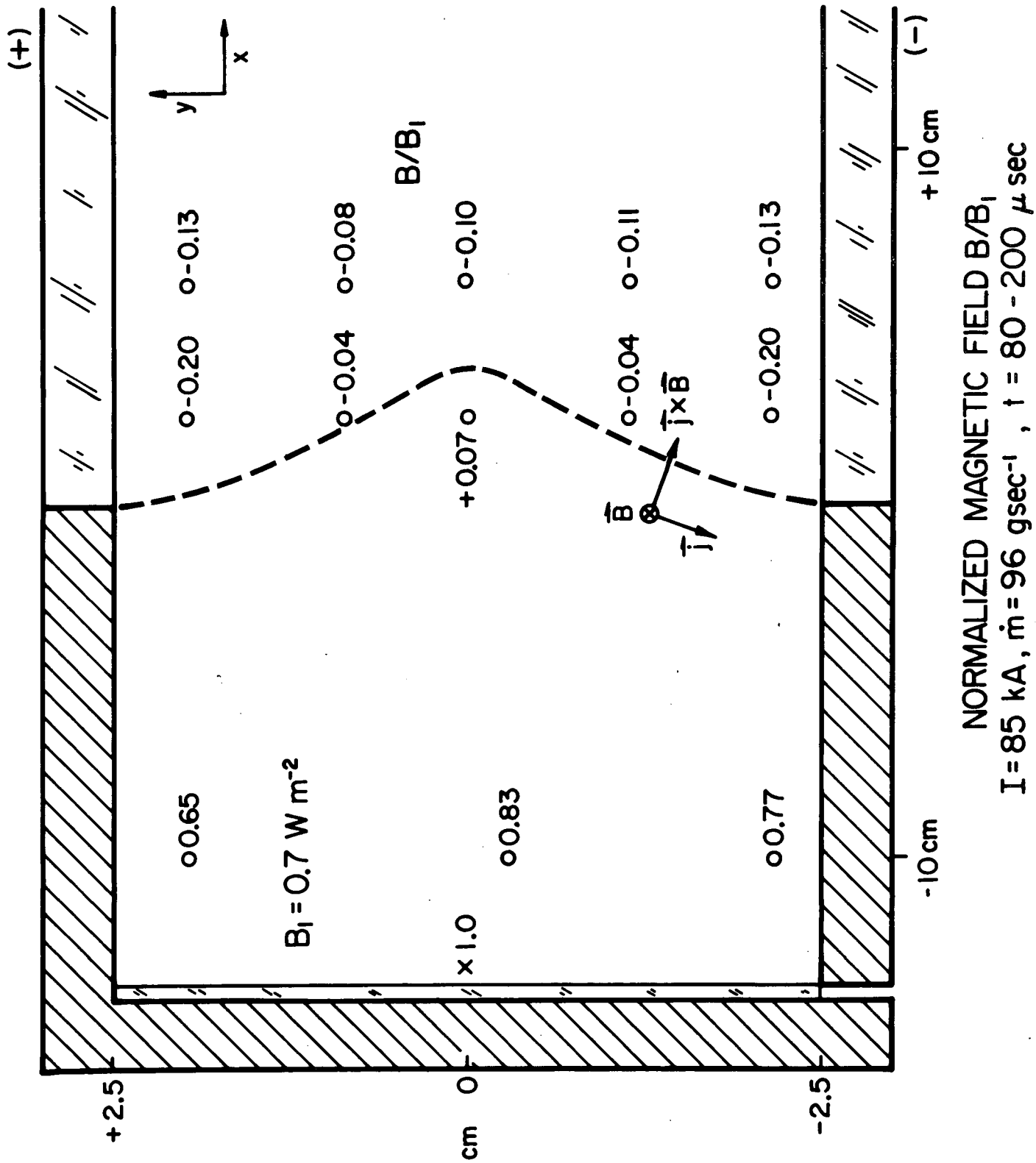

FIGURE 4-23
AP 25 4768

current distribution symbolized by the dotted line is about one channel height and, (c) the current distribution tilts somewhat towards the channel walls.

The measurements presented in this chapter form a well defined picture of the accelerator behavior. An analysis of this behavior based upon momentum and energy conservation arguments is presented in the following chapter.

CHAPTER 5

ENERGY DEPOSITION IN THE PARALLEL-PLATE PLASMA ACCELERATOR

5-1 INTRODUCTION

The central interest of this study is the initial apportionment of the input power to the streaming and thermal energy of the flow in a plasma accelerator. This initial energy deposition ratio achieves great importance if one is committed to the task of efficient plasma acceleration. Insufficient detailed knowledge of the electromagnetic, gasdynamic, and thermodynamic fields throughout the acceleration region commits us to obtain the energy deposition ratio through a "black box" or terminal analysis of the accelerator. This analysis is based upon measurement of the terminal electrical parameters of the accelerator and upon observation of properties of the flow into and out of the acceleration region. A self-consistent picture can then be drawn through the application of momentum and energy conservation arguments. Even on this basis, however, several complications arise due to the complex non-equilibrium state of the working fluid and the introduction of spurious mass into the flow through electrode and insulator erosion as well as ingestion of mass associated with the gasdynamic flow field established prior to the initiation of the discharge.

The parallel-plate geometry is particularly well suited for this analysis. The electromagnetic fields upstream of the acceleration zone can be obtained through simple one-dimensional arguments. Downstream of the acceleration zone, the plasma flow field is amenable to a steady, one-dimensional treatment as well. The first task, therefore, is to obtain the conservation relations in a convenient form for the analysis.

5-2 THE CONSERVATION RELATIONS

Analysis of the problem in a terminal fashion can best be performed with the conservation relations cast in integral form. This approach allows treatment of the problem on the basis of mass, momentum, and energy fluxes across appropriate surfaces without requiring any detailed knowledge of the processes which occur within the acceleration region.

a) Mass Conservation

The mass conservation equation for an arbitrary fixed volume can be written as:[25]

$$\int_V \frac{\partial \rho}{\partial t} dV = -\oint_A \rho \vec{u} \cdot d\vec{A} \tag{5-1}$$

where ρ is the density, $\vec{u}$, the velocity, V, the total volume, A, the total surface area of that volume, and dV and $d\vec{A}$ are respectively the volume and surface elements.

b) Momentum Conservation

The momentum conservation equation in integral form for an arbitrary fixed volume can be written as:[25]

$$\int_V \frac{\partial}{\partial t}(\rho \vec{u}) dV + \oint_A \rho \vec{u}(\vec{u} \cdot d\vec{A}) = -\oint_A p\, d\vec{A} + \int_V \vec{f}\, dV + \oint_A \overleftrightarrow{\tau} \cdot d\vec{A} \tag{5-2}$$

where p is the pressure, $\vec{f}$, the body force per unit volume, and $\overleftrightarrow{\tau}$, the viscous stress tensor. In the presence of electromagnetic forces, $\vec{f}$ takes the form:

$$\vec{f} = \vec{j} \times \vec{B} \tag{5-3}$$

where $\vec{j}$ is the current density and $\vec{B}$ is the magnetic field.

To transform the volume integral of the body forces into the required surface integral, the body force must be cast in the form of the divergence of a tensor.[26] The tensor can

then be integrated over the surface of the volume through the use of Ampere's Law in the low frequency limit ($u \ll c$):

$$\nabla \times \vec{B} = \mu_0 \vec{j} \tag{5-4}$$

the body force becomes:

$$\vec{f} = \vec{j} \times \vec{B} = \frac{1}{\mu_0} (\nabla \times \vec{B}) \times \vec{B} \tag{5-5}$$

Using the vector identity:

$$(\nabla \times \vec{B}) \times \vec{B} = (\vec{B} \cdot \nabla) \vec{B} - \frac{1}{2} \nabla (\vec{B} \cdot \vec{B}) \tag{5-6}$$

with:

$$0 = \vec{B} (\nabla \cdot \vec{B}) \tag{5-7}$$

added to both sides, the body force becomes:

$$\vec{j} \times \vec{B} - \frac{1}{\mu_0} (\nabla \times \vec{B}) \times \vec{B} = \nabla \cdot \frac{1}{\mu_0} \left(\vec{B}\vec{B} - \frac{1}{2} \overleftrightarrow{I} B^2 \right) \tag{5-8}$$

where

$$B^2 = \vec{B} \cdot \vec{B} \tag{5-9}$$

and $$\overleftrightarrow{I} = \delta_{ij}$$

The right hand term of Eq. (5-8) is the divergence of that part of the Maxwell stress tensor which is associated with the magnetic field.

By Gauss's theorem the volume integral is transformed into the desired surface integral:

$$\int_V \vec{f} \, dV = \frac{1}{\mu_0} \oint_A \vec{B} (\vec{B} \cdot d\vec{A}) - \frac{1}{2\mu_0} \oint_A B^2 \, d\vec{A} \tag{5-10}$$

and the momentum equation becomes:

$$\int_V \frac{\partial}{\partial t}(\rho \vec{u})dV + \int_A \rho\ \vec{u}(\vec{u}\cdot d\vec{A}) = -\oint_A \left(p + \frac{B^2}{2\mu_0}\right)d\vec{A} + \oint_A \frac{\vec{B}}{\mu_0}(\vec{B}\cdot d\vec{A}) - \int_A \overleftrightarrow{\tau}\cdot d\vec{A} \tag{5-11}$$

c) <u>Energy Conservation</u>

The energy conservation equation in integral form is:[25]

$$\int_V \frac{\partial}{\partial t}\left[\rho\left(e + \frac{u^2}{2}\right)\right]dV + \oint_A \rho\left(e + \frac{u^2}{2}\right)\vec{u}\cdot d\vec{A} = -\oint_A p\vec{u}\cdot d\vec{A}$$
$$-\oint_A (\vec{u}\cdot\overleftrightarrow{\tau})\cdot d\vec{A} + \int_V \left(\frac{\partial}{\partial t}\frac{B^2}{2\mu_0} + \vec{j}\cdot\vec{E}\right)dV + \oint_A \vec{q}\cdot d\vec{A} \tag{5-12}$$

where e is the internal energy per unit mass, $\frac{\partial}{\partial t}\frac{B^2}{2\mu_0}$ is the time rate of change of energy per unit volume associated with the magnetic field, and $\vec{q}$ is the heat flux vector. The quantity $\vec{j}\cdot\vec{E}$ where $\vec{j}$ is the current density as before and $\vec{E}$ is the electric field, represents the rate of conversion per unit volume of electromagnetic field energy into mechanical and thermal energy.

It is again advantageous to transform the volume integrals associated with the electromagnetic fields into surface integrals which are more closely related to the terminal parameters of the accelerator. To this end, using Ampere's Law:

$$\frac{\partial}{\partial t}\frac{B^2}{2\mu_0} + \vec{j}\cdot\vec{E} = \frac{\partial}{\partial t}\frac{B^2}{2\mu_0} + \frac{\nabla\times\vec{B}}{\mu_0}\cdot\vec{E} \tag{5-13}$$

With the identity:

$$(\nabla\times\vec{E})\cdot\vec{B} - \vec{E}\cdot(\nabla\times\vec{B}) = \nabla\cdot(\vec{E}\times\vec{B}) \tag{5-14}$$

and Faraday's Law:

$$\nabla\times\vec{E} = -\frac{\partial\vec{B}}{\partial t} \tag{5-15}$$

equation 5-13 becomes:

$$\frac{\partial}{\partial t}\frac{B^2}{2\mu_0} + \vec{j}\cdot\vec{E} = -\nabla\cdot\frac{(\vec{E}\times\vec{B})}{\mu_0} \tag{5-16}$$

Thus, using Gauss's theorem,

$$\int_V \left(\frac{\partial}{\partial t}\frac{B^2}{2\mu_0} + \vec{j}\cdot\vec{E}\right)dV = -\oint_A \frac{(\vec{E}\times\vec{B})}{\mu_0}\cdot d\vec{A} \tag{5-17}$$

The term $\frac{\vec{E}\times\vec{B}}{\mu_0}$ is the Poynting vector which represents the flux of electromagnetic energy per unit area per unit time. The energy equation therefore takes the form:

$$\int_V \frac{\partial}{\partial t}\left[\rho\left(e+\frac{u^2}{2}\right)\right]dV + \oint_A \rho\left(h+\frac{u^2}{2}\right)\vec{u}\cdot d\vec{A} = -\oint \frac{(\vec{E}\times\vec{B})}{\mu_0}\cdot d\vec{A}$$
$$+ \oint(\vec{u}\cdot\overleftrightarrow{\tau})\cdot d\vec{A} + \oint_A \vec{q}\cdot d\vec{A} \tag{5-18}$$

where the enthalpy h is defined as:

$$h = e + \frac{p}{\rho} \tag{5-19}$$

5-3 THE STEADY ONE-DIMENSIONAL APPROACH

The conservation relations derived in the previous section can be greatly simplified under the assumption of steady one-dimensional flow. With this assumption all terms containing time derivatives vanish and all properties of the flow and the electromagnetic field become the function of only one coordinate, namely the x coordinate as shown in Fig. 5-1. The relations are further simplified with the assumption of negligible viscous and heat transfer effects to be justified later.

The geometry of the accelerator is shown schematically in Fig. 5-1. The channel has an area A of width w and height h. The injector orifices in the back wall have a total area A_1. The injected argon propellant at the exit plane of the orifices has a pressure p_1, a density ρ_1,

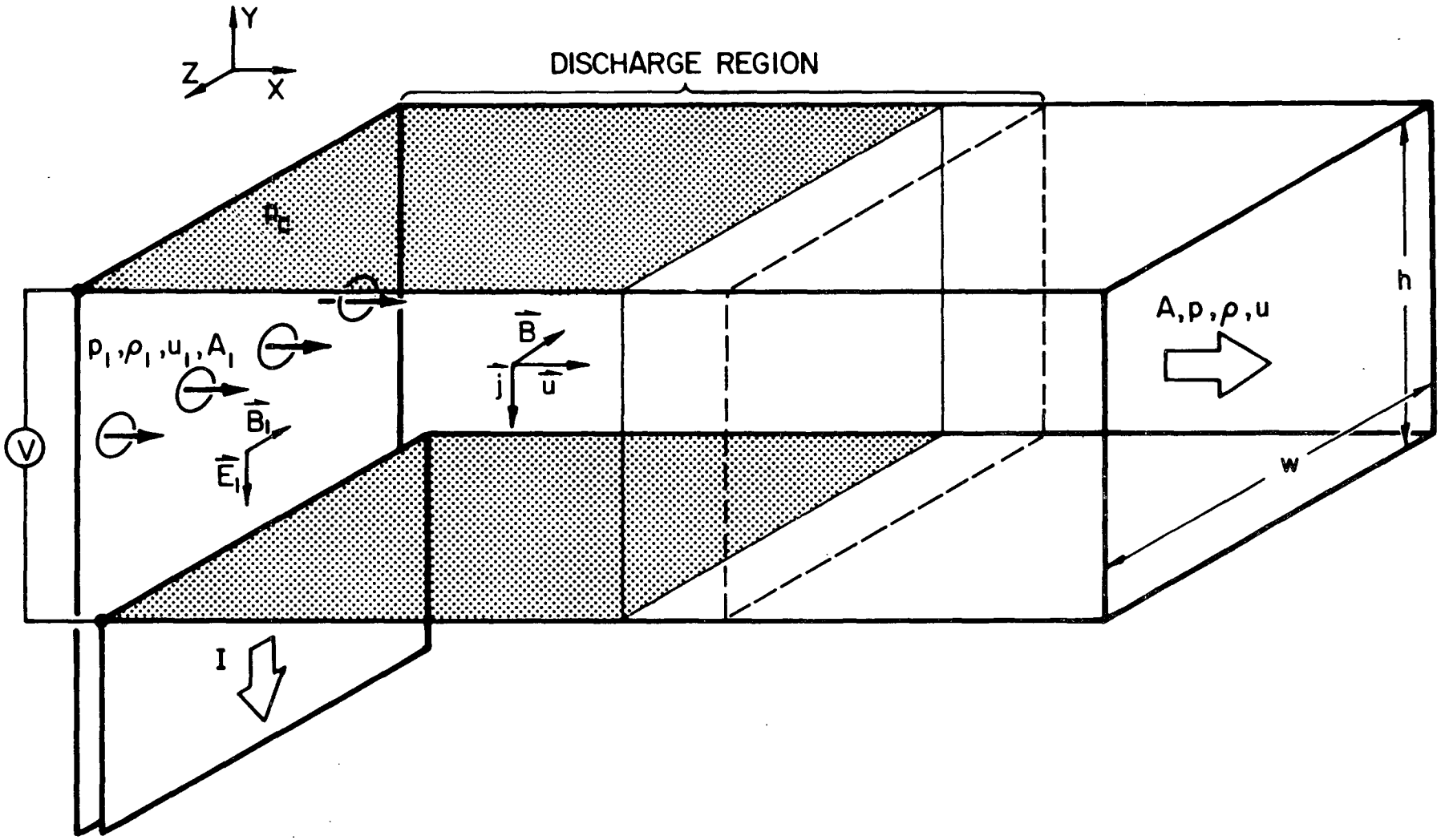

FIGURE 5-1
AP23 4791

SCHEMATIC OF PARALLEL-PLATE ACCELERATOR

and a velocity u_1 in the x direction. The current which flows through the backstrap and accelerator is I and the voltage drop across the electrodes is V. Downstream of the acceleration region the pressure is p, the density ρ, and the velocity u in the x direction.

Under the steady, one-dimensional assumption, the electromagnetic fields are obtained from the current and voltage across the accelerator. Due to the presence of anode and cathode fall voltages[27,28] only a fraction α of the voltage drop across the terminals is imposed on the flow. The voltage drop across the flow αV and the electric field $\vec{E}_1$ in the flow are related by:

$$\int \vec{E}_1 \cdot d\vec{l} = \alpha V \tag{5-20}$$

Assuming the electric field $\vec{E}_1$ is constant in the flow,

$$\vec{E}_1 = -\frac{\alpha V}{h}\,\hat{e}_y \tag{5-21}$$

The magnetic field $\vec{B}_1$ can be obtained from Ampere's Law:

$$\oint \vec{B}\cdot d\vec{l} = \mu_0 I \tag{5-22}$$

Therefore the magnetic field $\vec{B}_1$ is:

$$\vec{B}_1 = -\frac{\mu_0 I}{w}\,\hat{e}_z \tag{5-23}$$

The Conservation relations therefore become:

$$\rho_1 u_1 A_1 = \rho u A \qquad \text{Mass} \tag{5-24}$$

$$\rho u^2 A - \rho_1 u_1^2 A_1 = p_1 A_1 + A\left(p_e - p + \frac{\mu_0 I^2}{2w^2}\right) \qquad \text{Momentum} \tag{5-25}$$

$$\rho u A\left(h + \frac{u^2}{2}\right) - \rho_1 u_1 A_1\left(h_1 + \frac{u_1^2}{2}\right) = \alpha V I \qquad \text{Energy} \tag{5-26}$$

The remainder of the input energy, $(1-\alpha)$ VI, is assumed to be lost to the electrodes.

5-4 EXPERIMENTAL RESULTS

The experimental data strongly suggest that the steady analysis is applicable to this accelerator. A typical simultaneous record of current I, terminal voltage V_M and inductive voltage V_D (Sec. 4-2) taken at the 85 kA, 96 g/sec operating condition is shown in Fig. 5-2a. The current rises in 10 μsec and remains constant for 180 μsec. The inductive voltage, which is associated with changes of magnetic flux in the accelerator due to time derivatives of the total current or motion of the current distribution, drops to a negligible value after 50 μsec and remains practically zero until 180 μsec when the current begins to drop. The voltage V_M, which is measured downstream of the current distribution, represents the sum of the resistive voltage and the induced emf across the accelerator. This voltage assumes a constant value after 50 μsec and begins to drop at 180 μsec, indicating steady electrodynamic operation of the accelerator in this time interval.

Measurements of pressure in the accelerator channel (Sec. 4-6) show that steady gasdynamic operation is achieved as well. Fig. 5-2b shows triple overlays of simultaneous pressure measurements taken 10 cm upstream of the electrode-insulator junction and 23 cm downstream of the junction in the centerline of the channel top. The peak in the upstream pressure p_c is associated with the unsteady phase of the discharge. The second and third peaks are due to internal reflections in the probe so that the upstream pressure achieves a low but steady value of about 0.03 atm roughly at the same time the voltage reaches the steady phase.

The downstream pressure, on the other hand, achieves a steady value at 95 μsec and remains roughly steady at approximately 0.45 atm until 270 μsec. There is a time delay between achievement of the steady phase at the electrode-insulator junction and at the downstream station due to the time of transit of the plasma between the two stations. It

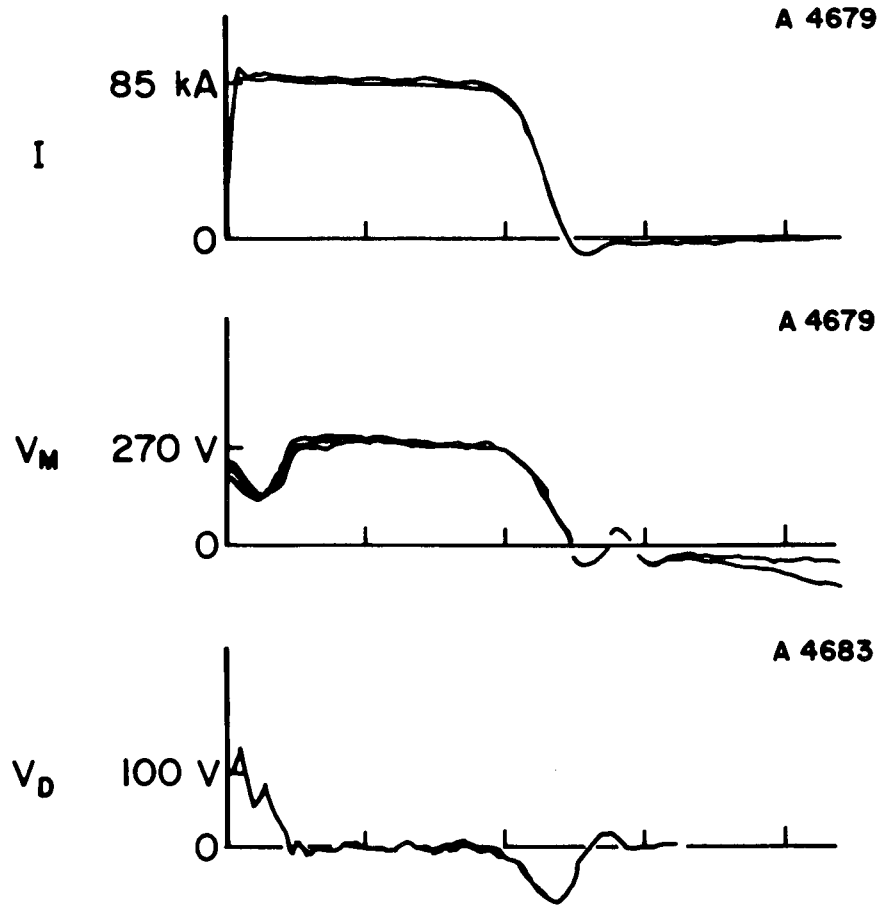

a) TERMINAL MEASUREMENTS

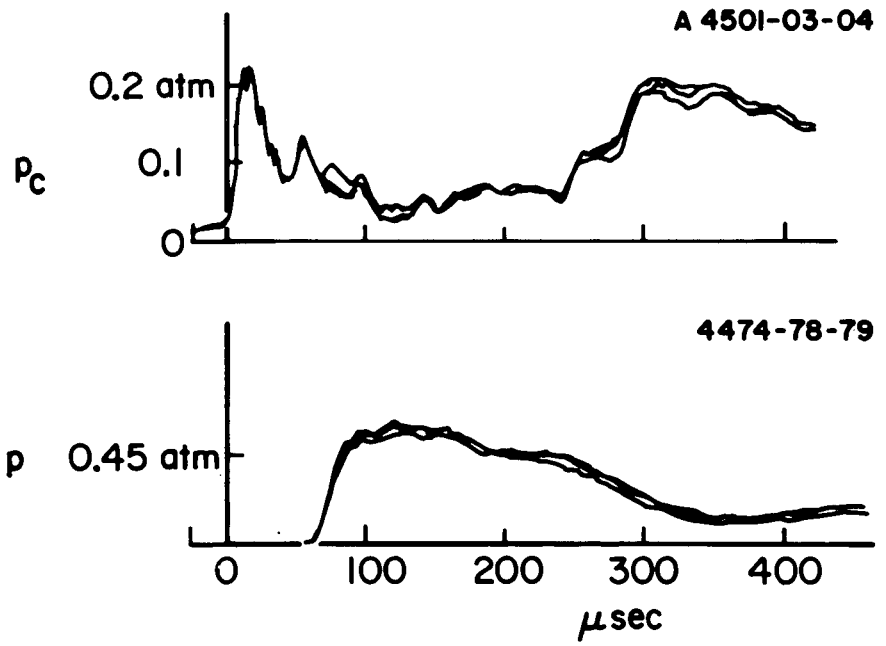

b) PRESSURE MEASUREMENTS, I = 85 kA

FIGURE 5-2
AP 25-4731

is important, however, to note that the duration of the steady phase is the same whether it is obtained from the pressure or terminal voltage measurements.

Measurements of pressure and electron density indicate that the one-dimensional assumption is valid as well. Pressures were measured at a station 23 cm downstream from the electrode insulator junction, at two representative positions in the channel top: the centerline of the channel and 5 cm to one side. The values of measured pressure fall within a few percent of each other indicating a negligible pressure gradient across the width of the channel as expected. No pressure measurements were taken across the height of the channel. However, it is reasonable to expect the pressure to remain uniform across this dimension at the downstream position, because this position is located outside the current distribution at a distance which is at least three times the characteristic distance associated with the downstream excursion of the current distribution.

A typical measurement of electron density across the height of the channel obtained spectroscopically (Sec. 4-5b) is shown in Fig. 5-3. These measurements represent an average of the electron density along the line of sight which is the width of the channel. Though the measured densities show some variation across the height of the channel, the deviations are found to be about 15 percent of the average. Therefore, for the purpose of the analysis, the electron density is considered constant with a value equal to its average value.

For the one-dimensional assumption to be valid it is also necessary to assume one-dimensionality in the electromagnetic fields as well. This assumption is based upon the small height of the channel with respect to its width and upon the uniformity of the current density in the discharge as well as in return conductors. Previous magnetic probing of the discharge in the same accelerator with similar

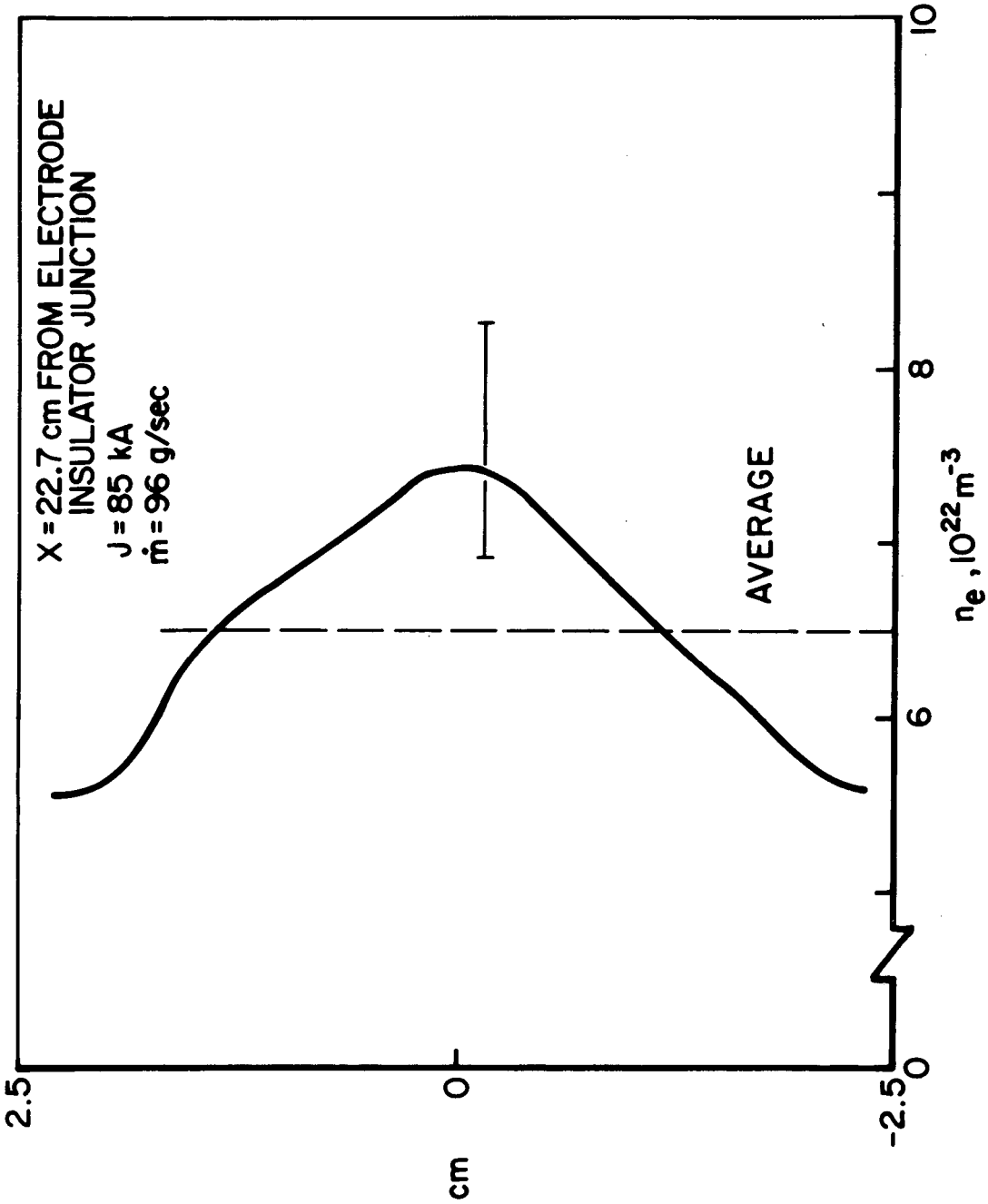

ELECTRON DENSITY PROFILE
(SAME AS FIG. 4-13)

FIGURE 5-3
AP 25-4732

currents[2,29] and photographic observations of the discharge region (Sec. 4-4) have shown that the two-dimensional effects associated with the finite width of the conductors are about 20 - 30% and that no distinct current concentrations or spokes exist. Therefore, a one-dimensional treatment of the problem is justified.

Since viscous and heat transfer effects depend quite heavily upon velocity and temperature gradients in the flow which are not known a priori as well as on transport properties of the fluid, the analysis will be carried out on the presumption that these effects are small and can be neglected. It will be later shown that this is indeed the case.

5-5 INTERPRETATION OF THE DATA

The experimental data presented in the previous section can now be interpreted within the framework of the steady one-dimensional conservation relations stated in Sec. 5-3. The analysis will be carried out between two stations in the channel:

Station 1. - Located 13.7 cm upstream of the electrode-insulator junction at the same axial position as the injectors, and,

Station 2. - Located 22.7 cm downstream of the electrode insulator junction.

a) Momentum Conservation

The pressure p_1, density ρ_1, and velocity u_1 at station 1 are estimated on the basis of an argon mass flow of 96 g sec^{-1} assuming choked flow at the orifices. Under these assumptions:

$$p_1 = 0.7 \times 10^5 \quad N\,m^{-2}$$
$$\rho_1 = 0.9 \quad Kg\,m^{-3}$$
$$u_1 = 3.7 \times 10^2 \quad m\,sec^{-1}$$

For a current of 57 kA, which is the lowest current used,

$$\frac{\mu_0 I^2 A}{2w^2} = 7 \times 10^2\ N \gg 0.35 \times 10^2 N = \rho_1 u_1^2 A_1$$

$$\frac{\mu_0 I^2 A}{2w^2} = 7 \times 10^2 N \gg 0.2 \times 10^2 N = p_1 A_1$$

$$\frac{\mu_0 I^2}{2w^2} = 9 \times 10^4\ Nm^{-2} \gg 0.5 \times 10^4\ N\ m^{-2} = p_c$$

Therefore, the terms on the right may be neglected in the momentum equation (Eq. 5-25) which becomes

$$p + \rho u^2 = \frac{\mu_0 I^2}{2w^2} \tag{5-27}$$

Table 5-I in page 119, summarizes the values of the magnetic pressure at station 1, $\frac{\mu_0 I^2}{2w^2}$, the static pressure at station 2, p, and the electron density at station 2, n_e. All these quantities are determined experimentally. Under the assumption of full (single) ionization, the density ρ of the fluid becomes:

$$\rho = n_e m_i \tag{5-28}$$

where m_i is the mass of the argon ions.

There is strong experimental evidence to suggest that the full (single) ionization assumption is indeed correct. Spectroscopic observation of the flow in this accelerator and in a coaxial MPD accelerator operating with similar current densities indicate that singly ionized argon is the dominant species in the flow.[30] Further, there is no energy source to increase the ionization level downstream. Extensive recombination, on the other hand, is not believed to take place in the bulk of the plasma since the constant area channel precludes expansion and cooling of the flow.

TABLE 5-I MOMENTUM CONSERVATION

$\dot{m}$	I	$\frac{\mu_0 I^2}{2w^2}$	p	n_e	ρ	ρu^2	u	u_D	$\dot{m}_p$	M	M_p
10^{-1} Kg sec^{-1}	10^3 A	10^5 N m^{-2}	10^5 N m^{-2}	10^{22} m^{-3}	10^{-3} Kg m^{-3}	10^5 n m^{-2}	10^3 m sec^{-1}	10^3 m sec^{-1}	10^{-1} Kg sec^{-1}		
0.96	85	2.0	0.45	6.5	4.3	1.6	6.0	6.8	2.0	2.0	1.6
0.96	72	1.4	0.41	4.8	3.2	1.0	5.6	5.3	1.4	2.0	1.3
0.96	57	0.9	0.31	3.5	2.3	0.6	5.1	4.5	0.9	-	1.2
±20%	± 5%		±20%	±15%				±20%		±15%	*

TABLE 5-II ENERGY CONSERVATION

$\dot{m}$	I	V	T_i	h	$\frac{u^2}{2}$	$\rho u A(h+u^2/2)$	αVI	$\frac{\rho u A(h+u^2/2)}{\alpha VI}$	$\frac{u^2}{2h}$	V_{uB}	$\frac{V_{uB}}{\alpha V - V_{uB}}$
10^{-1} Kg sec^{-1}	10^3 A	10^2 V	10^4 °K	10^7 m^2 sec^{-2}	10^7 m^2 sec^{-2}	10^7 W	10^7 W			V	
0.96	85	2.7	3.0	6.6	1.8	1.7	2.0	0.85	0.27	43	0.23
0.96	72	2.3	4.3	7.2	1.6	1.2	1.4	0.85	0.22	33	0.20
0.96	57	1.9	4.5	7.4	1.3	0.8	0.9	0.85	0.18	24	0.18
±20%	±5%	±5%									*

*Typical Uncertainties in Experimentally Determined Quantities

Using the measured values of p, I and n_e and the subsequently calculated density ρ, equation (5-27) is used to determine the average velocity u necessary to conserve momentum across the discharge. This value is compared in the table with the velocity u_D obtained from the Doppler shift measurements (Sec. 4-5c). The agreement between the calculated velocity and measured velocity is good verifying the several assumptions involved in the calculation.

Also shown in Table 5-I is the value of the Mach number M_p calculated as:

$$M_p = \left(\frac{\rho u^2}{\gamma p}\right)^{1/2} \tag{5-29}$$

where γ = 1.3 is the ratio of specific heats obtained from the aerodynamic observations of the flow. The values presented in the table show that the flow is supersonic for the three current pulses. The value of M_p may be compared to the Mach number M obtained, for I=85 and 72 kA, with the techniques described in Sec. 4-3. As indicated previously, the shocks observed with the 57 kA pulse were too faint to yield a useful measurement of Mach number and therefore there is no entry for M in the table for this condition. Despite the approximations involved in the two calculations, namely that the plasma can be treated as an ideal gas with constant specific heats, the agreement between the two values is quite reasonable.

The column $\dot{m}_p$ shows the mass flow calculated on the basis of the measured densities and calculated velocities at station 2 for the three currents studied. It is found that the output mass flow is a strong function of current despite the fact that the input mass flow is fixed at 96 g sec^{-1}. This indicates that mass is ingested from the gasdynamic flow established prior to breakdown, or from electrode and insulator ablation.

b) Energy Conservation

On the basis of the properties of the flow through the injectors it is found that the inlet kinetic energy is negligible with respect to the input electrical energy to the flow, i.e.

$$\rho_1 u_1 A_1 \left(h_1 + \frac{u_1^2}{2}\right) \ll \alpha V I \tag{5-30}$$

With this approximation, the energy equation becomes

$$\rho u A \left(h + \frac{u^2}{2}\right) = \alpha V I \tag{5-31}$$

The enthalpy in the exhaust flow could be expressed as a function of density and pressure. It is, however, more convenient to express it as a function of temperature and pressure for reasons which will become clear below.

Since there are no reliable temperature measurements in this accelerator, the ion temperature T_i can be estimated on the basis of an equation of state which takes into account the fact that the fluid acts like an ideal gas whose pressure is the sum of the partial pressures of electrons and ions:

$$p = n_e K T_e + n_i K T_i \tag{5-32}$$

Under the assumption of full (single) ionization, $n_e = n_i$ and:

$$p = n_e K \left(T_e + T_i\right) \tag{5-33}$$

Experimentally it has been found that, in accelerators of this type, the electron temperature T_e remains nearly constant at 1.5-2.0 eV over a wide range of operating conditions.[28] Table 5-II in page 119 shows the values of ion temperature obtained with this equation assuming

an electron temperature of 2×10^4 °K.
Consistent with the two-fluid model incorporated in the equation of state presented above, the enthalpy can be expressed as:

$$h = h(T_e, T_i, p) \tag{5-34}$$

Here, T_i describes the energy content of the random ion motion, while T_e describes the energy content of the electron random motion and of the excited states which in this case include full (single) ionization.

The electron temperature never reaches the ion temperature since thermal energy transferred from ions to electrons easily passes from the electron thermal modes into the excited state system. This process can account for the constant electron temperatures observed. With this model, the expression for the enthalpy becomes:[31]

$$h = \int_{T_1}^{T_e} C_p \, dT + \frac{5}{2} R \int_{T_e}^{T_i} dT \tag{5-35}$$

The first term can be obtained directly from a Mollier chart for argon[32] while the second may be evaluated directly for each calculated value of ion temperature. Assuming an electron temperature of 2×10^4 °K the expression for the enthalpy becomes:

$$h = (5.0 \times 10^7 + 5.22 \times 10^2 \, T_i \, {}^\circ K^{-1}) \frac{m^2}{sec^2} \tag{5-36}$$

The column h in Table 5-II displays the value of the enthalpy obtained with the above expression based upon the calculated ion temperatures. The total power in the exhaust, $\rho u A(h + \frac{1}{2} u^2)$ can then be calculated and is also shown in the table. This power should be compared to the total power available to the flow, αVI, defined previously. For an MPD

accelerator of comparable size and range of operation, the cathode and anode falls are typically of the order of 10 and 20 volts respectively.[28,27] It is therefore estimated that between 10 and 20 percent of the input power is lost to the electrodes resulting in a value of $\alpha = 0.85$. The total input power available to the flow, 0.85 VI, shown in the next column, compares very favorably to the total power in the exhaust.

c) <u>The Energy Deposition Ratio</u>

The initial energy deposition ratio, which is the central interest of this study can be calculated using two approaches. One approach uses the ratio of streaming to thermal energy in the exhaust under the assumption that the constant area channel does not allow acceleration of the flow downstream of the discharge region. The energy deposition ratio calculated by this method is shown in Table 5-II in page 119 in the column labeled $\frac{u^2/2}{h}$. According to the calculations only about 20 percent of the energy in the exhaust appears as directed kinetic energy.

The other approach uses the ratio of the motional emf and resistive components of the terminal voltage across the accelerator. To define the motional emf, the energy equation is used in the form:

$$W = \int_V \vec{E} \cdot \vec{j} \, dV \tag{5-37}$$

where W is the rate of energy input to the plasma by $\vec{E}$, the external electric field and $\vec{j}$ is the current density. In the plasma frame of reference, the electric field is $\vec{E}'$

$$\vec{E}' = \vec{E} + \vec{u} \times \vec{B} \tag{5-38}$$

where $\vec{B}$ is the local magnetic field and $\vec{u}$ is the velocity of the plasma. Substituting the equation above in the energy equation, the total energy input to the plasma by the external

fields becomes:

$$W = \int_V \vec{E}' \cdot \vec{j}\, dV - \int_V (\vec{u} \times \vec{B}) \cdot \vec{j}\, dV \qquad (5\text{-}39)$$

Since the total energy deposited in the streaming plasma can be written as αVI where as before α is the fraction of the input power available to the flow, the voltage drop minus the fall voltages can be written as the sum of two voltages:

$$\alpha V = \frac{1}{I}\int_V \vec{E}' \cdot \vec{j}\, dV - \frac{1}{I}\int_V (\vec{u} \times \vec{B}) \cdot \vec{j}\, dV \qquad (5\text{-}40)$$

$$= V_R + V_{uB} \qquad (5\text{-}41)$$

where V_R is defined as the resistive voltage drop across the accelerator while V_{uB} is the motional emf.

To perform a rigorous calculation of V_{uB} a detailed knowledge of the velocity and current density in the acceleration region is required. Its magnitude, however, can be estimated by assuming reasonable profiles for the velocity $\vec{u}$, current density $\vec{j}$, and magnetic field $\vec{B}$. Table 5-III in page 125 summarizes the results of calculations made for different arbitrary profiles. In this table, B_1 is the magnetic field upstream of the current distribution, u is the downstream velocity, w is the width of the accelerator, δ is the streamwise thickness of the current distribution and I is the total current. The table shows that the motional emf takes the form:

$$V_{uB} = u B_1 h Q \qquad (5\text{-}42)$$

where h is the height of the channel, and Q is a factor which depends on the particular profiles chosen for u and B. This value ranges between 0.16 and 0.41 for the profiles shown.

TABLE 5-III - V_{uB} FOR DIFFERENT VELOCITY AND CURRENT DENSITY DISTRIBUTIONS*
for: $0 \leq x \leq \delta$

	$u(x)$	$B(x)$	$j(x)$	V_{uB}
I	$\frac{ux}{\delta}$	$B_1\left(1 - \frac{x}{\delta}\right)$	$\frac{I}{w\delta}$	$\frac{1}{6}\ uhB_1$
II	$2u\left(\frac{x}{\delta} - \frac{x^2}{2\delta^2}\right)$	$B_1\left(1 - \frac{x}{\delta}\right)$	$\frac{I}{w\delta}$	$\frac{1}{4}\ uhB_1$
III	$u \sin \frac{\pi x}{2\delta}$	$B_1 \cos \frac{\pi x}{2\delta}$	$\frac{\pi}{2\delta}\ \frac{I}{w} \sin \frac{\pi x}{2\delta}$	$\frac{1}{3}\ uhB_1$
IV	$\frac{ux}{\delta}$	$B_F \cos \frac{\pi x}{2\delta}$	$\frac{\pi}{2\delta}\ \frac{I}{w} \sin \frac{\pi x}{2\delta}$	$\frac{1}{4}\ uhB_1$
V	$u \sin \frac{\pi x}{2\delta}$	$B_1\left(1 - \frac{x}{\delta}\right)$	$\frac{I}{w\delta}$	$\frac{4}{\pi^2}\ uhB_1$

*The general form of the $B(x)$ profile was chosen to satisfy: $B(o) = B_1$, $B(\delta) = 0$
Similarly, the general form of the $u(x)$ profile was chosen to satisfy:
$u(o) = 0$, $u(\delta) = u$

The ratio of motional emf to resistive drop is shown in the column $V_{uB}/(\alpha V-V_{uB})$ of Table 5-II in page 119. The value is calculated assuming that there is no downstream expansion of the flow. Therefore, the measured velocities accurately reflect the velocity of the fluid at the exit of the current distribution. The geometric factor Q for this calculation is set at 0.20.

There is reasonable agreement between the energy deposition ratio based on kinetic energy and enthalpy and the ratio based on motional emf and resistive voltage drops. Both these ratios point to the conclusion that the discharge itself imparts less energy to the flow by direct body acceleration than by resistive heating. In the absence of downstream expansion this predicates low exhaust speeds and high downstream pressures and temperatures. Conversely, it seems reasonable to infer that the comparatively high exhaust speeds found in conventional MPD arcs of the same power must be derived in substantial part from electrothermal conversion from the high enthalpy arc plasma via the downstream expansion permitted in this geometry.

d) Viscous Dissipation and Heat Transfer

The calculations performed in the previous section are based on the assumption that viscous drag is not severe. The values of the flow properties previously calculated and approximate values of the transport properties published in the literature can be used to estimate the magnitude of the viscous drag. For this purpose, the Reynolds number of the flow based upon the length of the channel for the 85 kA current pulse is:

$$Re_{\ell} = \frac{\rho u \ell}{\mu} = 3\times10^{5} \qquad (5\text{-}43)$$

where:[33]

$$\ell = 2 \times 10^{-1}\ m$$

$$\mu = 2 \times 10^{-5}\ Kg\ m^{-1}\ sec^{-1}$$

For an incompressible turbulent boundary layer, the friction coefficient is:[34]

$$f = \frac{0.03}{(Re_\ell)^{1/5}} = 2.4 \times 10^{-3} \qquad (5\text{-}44)$$

The ratio of viscous forces to electromagnetic forces becomes:

$$\frac{F_V}{F_M} = \frac{f \rho u^2\, 2 \ell w \left(\frac{h}{w}+1\right)}{h w (\mu_0 I^2 / 2 w^2)} = 2 \times 10^{-2} \qquad (5\text{-}45)$$

where $h = 5 \times 10^{-2}$ m and $w = 1.5 \times 10^{-1}$ m. It is therefore justified to drop the viscous dissipation from the momentum and energy equations.

Due to the complex nature of the working fluid, it is not possible to perform a similar calculation for the heat transfer to the channel walls. However, it is possible to estimate the magnitude of the heat transfer from the ratio of the power delivered to the flow to the total power in the exhaust which is shown in the column $\frac{\rho u A (h + u^2/2)}{\alpha V I}$ in Table 5-II in page 119. According to this ratio, 75 to 85% of the power delivered to the beam appears as power in the exhaust. On this basis, it is estimated that 15 to 25% of the input power is lost by either heat transfer to the channel walls or by radiation.

CHAPTER 6

SUMMARY AND CONCLUSIONS

The principal accomplishments of the research program described in the preceding chapters and in the appendices which follow are:

1. An "LC Ladder" network power source has been constructed from low-grade commercial energy storage capacitors. This power source can store safely a maximum charge of 27 C and 125 kJ of electrical energy.

2. This power source delivers flat-top, non-reversing current pulses with risetimes of 10 μsec and currents in the range from 33 kA to 120 kA with durations in the range from 0.84 to 0.21 msec respectively.

3. A parallel-plate accelerator has been operated with this power source in the quasi-steady mode with currents up to 100 kA and input argon mass flows up to 100 g sec^{-1}. For currents between 50 and 90 kA the exhaust flow is supersonic with typical velocities of 5-6 x 10^3 m sec^{-1}, electron densities of 4-7 x $10^{22} m^{-3}$ and pressures of 0.3 - 0.5 atm.

4. Momentum and energy conservation are satisfied across the discharge with a mass flow which obeys the following empirical relation:

$$\frac{I^2}{\dot{m}} = 3.7 \times 10^1 \ KA^2 g^{-1} sec \qquad (6\text{-}1)$$

5. A large fraction (85%) of the energy delivered to the plasma appears in the exhaust flow. However, only 20% of the energy in the exhaust appears as directed kinetic energy $u^2/2$. The remainder appears as enthalpy h which also includes ionization. Since the 1-D geometry of

the channel does not allow expansion of the flow, it is concluded that the discharge itself imparts less energy to the flow by direct body acceleration than by resistive heating.

7. The energy deposition ratio $u^2/2h$ shows reasonable agreement with the ratio $V_{uB}/(\alpha V - V_{uB})$ in which the motional emf is calculated on the basis of the prevailing velocities and magnetic fields in the discharge region.

8. A magnetic boundary layer model which considers the convection of the magnetic field by the flow and the diffusion of the magnetic field in the conducting fluid is used to explain some of the features of the discharge region. Specifically, the downstream convection of the magnetic field by the flow requires the presence of an axial component $\vec{j}_x$, of the current density. The $\vec{j}_x \times \vec{B}_z$ body force causes a pressure gradient in a direction orthogonal to the channel axis. This pressure gradient compresses the plasma against the insulated channel wall and does not contribute to the axial acceleration of the flow in the parallel-plate geometry. However, in coaxial MPD accelerators which allow a streamwise expansion of the plasma compressed towards the centerline of the channel by the $\vec{j}_x \times \vec{B}_\theta$ body force, it gives rise to the "pumping"[1] contribution to the thrust. The component of current density orthogonal to the channel axis, accelerates the flow in the axial direction in the parallel-plate accelerator and gives rise to the "blowing"[1] contribution to the thrust in coaxial MPD accelerators.

APPENDIX A
THE LAM ACCELERATOR GEOMETRY

A-1 INTRODUCTION

Improvements in the performance of MPD accelerators are strongly based upon an understanding of the acceleration region. One of the most important steps in this understanding is the formulation of a model which incorporates the experimental observations performed in the accelerator. Given the complexity of the problem, however, the model is best formulated in a geometry which is analytically tractable. As it will be seen in the last section of this appendix, this geometry would consist of an accelerator which is infinitely high to make the magnetic Reynolds R_M very large and infinitely wide to make three-dimensional effects negligible.

These requirements are difficult to satisfy from a practical point of view. However, they can be partly met by a geometry proposed by S. H. Lam.[35] It consists of the same accelerator system described in Chapter 3 of this thesis in which the 13.8 cm-long anode and the 109 cm-long insulating channel wall which follows it, has been replaced by a 123 cm-long aluminum electrode. Therefore, there is one full electrode, namely, the anode and one electrode-insulator junction at the cathode, as shown in Fig. A-1. This geometry has three advantages: a) Under the assumption of perfectly conducting electrodes the current density vector is normal at the electrode surface. Therefore the accelerator may be treated as one-half of an accelerator of twice the height whose plane of symmetry is the full electrode. b) The discharge is constrained at one electrode and for all practical purposes the other electrode appears infinite in the streamwise direction, and c) The larger effective height facilitates experimental observations.

This appendix describes experimental observations and measurements performed in this geometry, which hereafter will be called the Lam geometry, using the same techniques

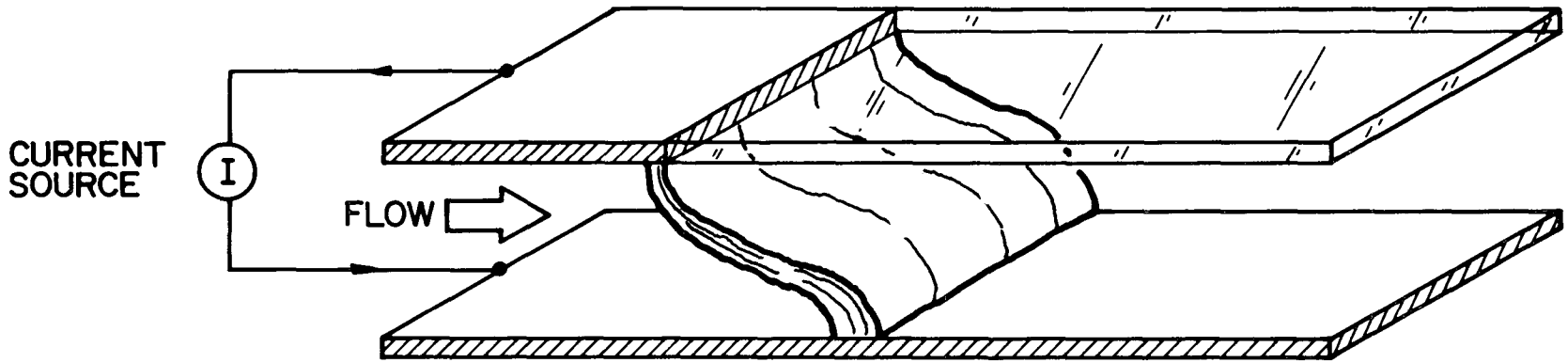

PARALLEL-PLATE ACCELERATOR
(LAM GEOMETRY)

FIGURE A-1
AP25 4786

discussed in Chapter 4 of this work. Momentum and energy conservation arguments are then applied to check the self-consistency of the measurements. The essential features of the model in conjunction with the experimental observations which lend support to the model are presented in the last section of this appendix.

A-2 EXPERIMENTAL OBSERVATIONS

a) Terminal Measurements

Terminal measurements obtained with the same techniques described in Sec. 4-2 are presented in Fig. A-2. It displays simultaneous record of current I, terminal voltage V_M and inductive voltage V_D for the 57, 72, and 85 kA pulses of 210 μsec duration for a mass flow of 96 g sec^{-1}. The signatures of V_D show that the discharge in this geometry stabilizes as well, though the initiation phase has a longer duration (120, 100, and 70 μsec for the three current pulses as opposed to 60 μsec for the fully insulated geometry). It is interesting to note that stabilization takes place despite the freedom offered by the uninsulated electrode which in principle allows unhindered excursion of the current distributions in the downstream direction. The plateau in the voltage V_M, which is identical to the terminal voltage after stabilization, is presented as a function of current for an argon mass flow of 96 g sec^{-1} in Fig. A-3. In the range of currents investigated, the voltage is linear with current in this geometry as well. However, the measured voltages are slightly higher and the slope of the voltage current characteristic is also larger than for the fully insulated geometry (Fig. 4-3).

b) Photographic Observations of the Discharge Region

A side view of the discharge region, obtained with the same shutter described in Sec. 4-3, is shown in Fig. A-4 for I=85kA and a mass flow of 96 g sec^{-1}. The

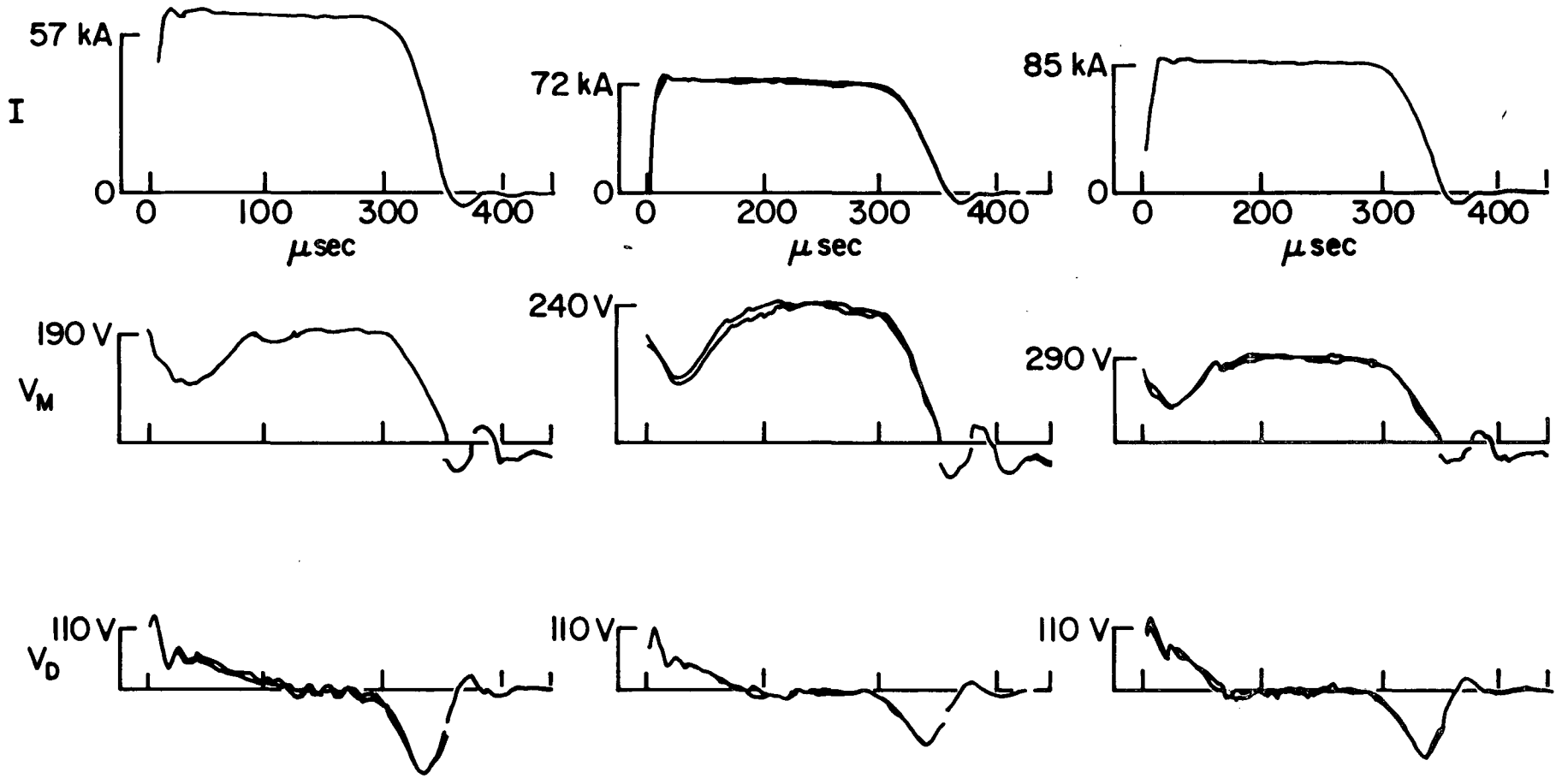

a) I = 57 kA

b) I = 72 kA

c) I = 85 kA

TERMINAL PROPERTIES
(LAM GEOMETRY)

FIGURE A-2
AP25 4785

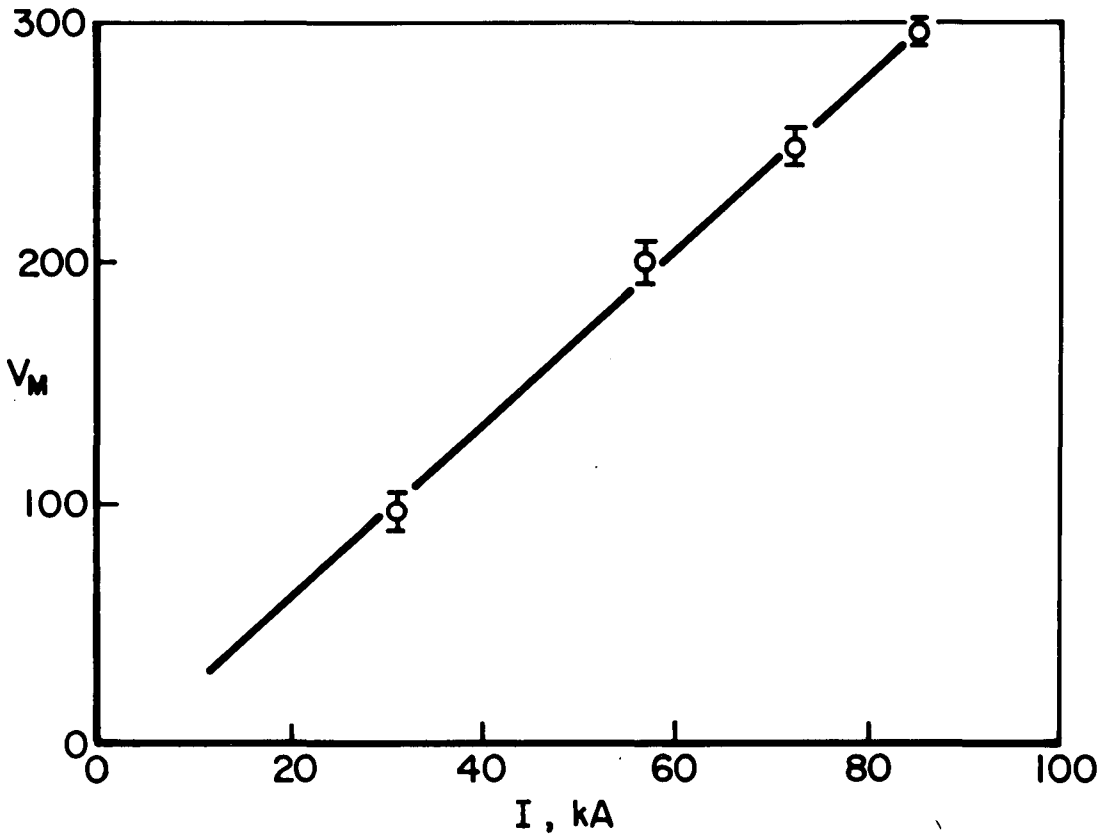

CURRENT VOLTAGE CHARACTERISTIC
$\dot{m} = 96\ g\,sec^{-1}$
(LAM GEOMETRY)

FIGURE A-3
AP25 4779

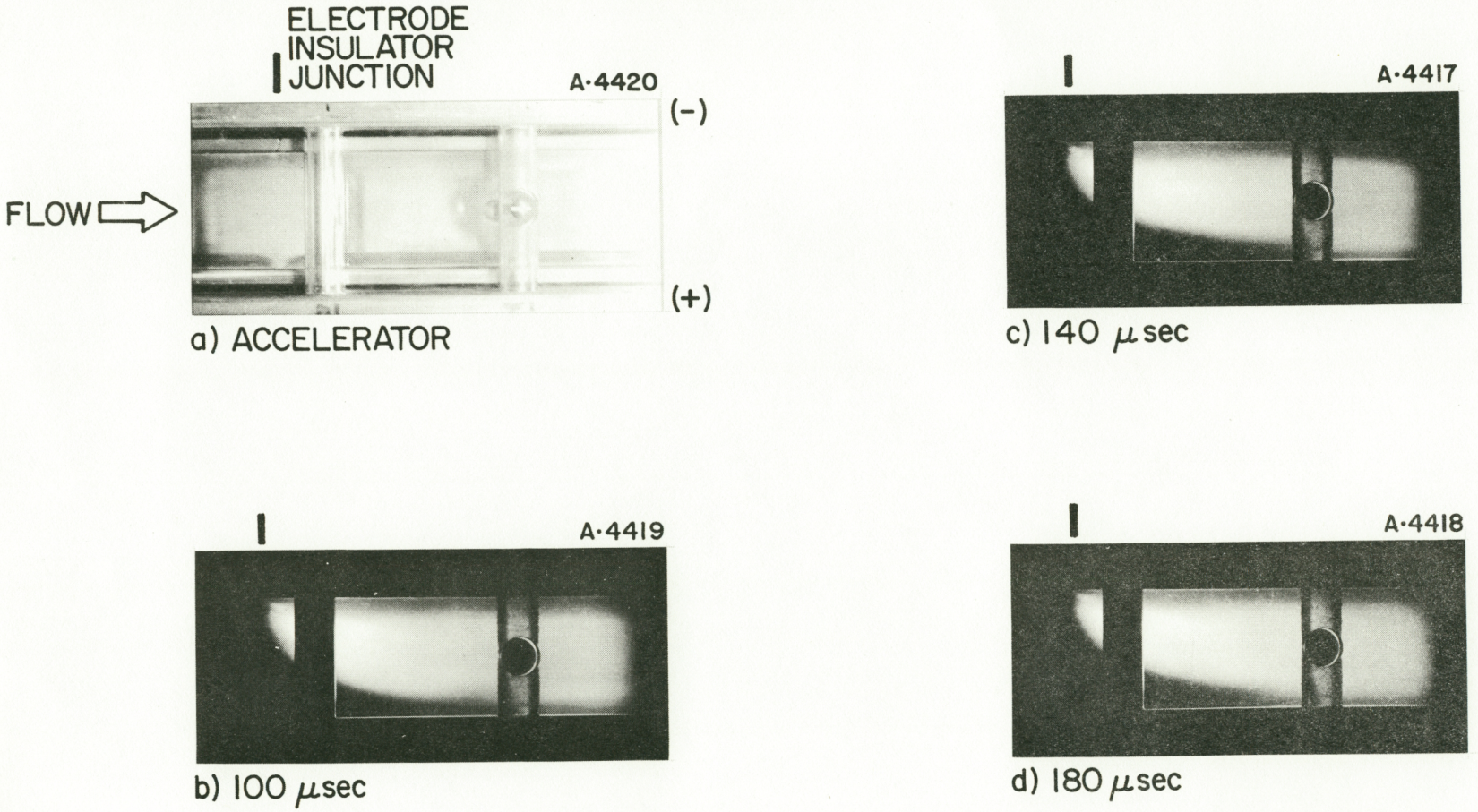

PHOTOGRAPHS OF ACCELERATOR OPERATION (SIDE VIEW)
$I = 85$ kA, $\dot{m} = 96$ g/sec
(LAM GEOMETRY)

FIGURE A-4
AP 25 P 417

accelerator channel and the location of the electrode-insulator junction at the cathode are shown in Fig. A-4a. Figure A-4b shows the discharge radiance at 100 μsec in the configuration it will retain for the rest of the pulse, as verified in Figs. A-4c and A-4d taken at 140 and 180 μsec respectively. The radiance is diffuse throughout the discharge region and its edge forms a sharp boundary of roughly parabolic shape with its vertex at the cathode. This boundary merges with the anode roughly two and one-half channel heights downstream of the electrode-insulator junction. This radiance pattern may be compared with the one obtained with the fully insulated geometry (Fig. 4-7) which appears to consist of two such parabolic regions which merge in the center of the channel, one channel height downstream of the electrode-insulator junction.

c) Electron Density Measurements

Measurements of electron density obtained across the height of the channel with the spectroscopic technique described in Sec. 4-5b are presented in Figs. A-5 and A-6. Figure A-5 shows the measured electron densities, for the 57, 72, and 85 kA pulses and an argon mass flow of 96 g sec^{-1}, 6.2 cm downstream of the electrode-insulator junction. At the higher currents, the profiles show a marked asymmetry with the highest electron densities measured on the cathode side of the channel at the bottom of the figure. The highest electron densities correspond to the bright region shown in the photographs presented in Fig. A-4.

At the 6.2 cm axial position, the electron densities for I=85 kA are about 30% higher than for the fully insulated geometry at the same current. Profiles of electron density across the height of the channel 22.7 cm

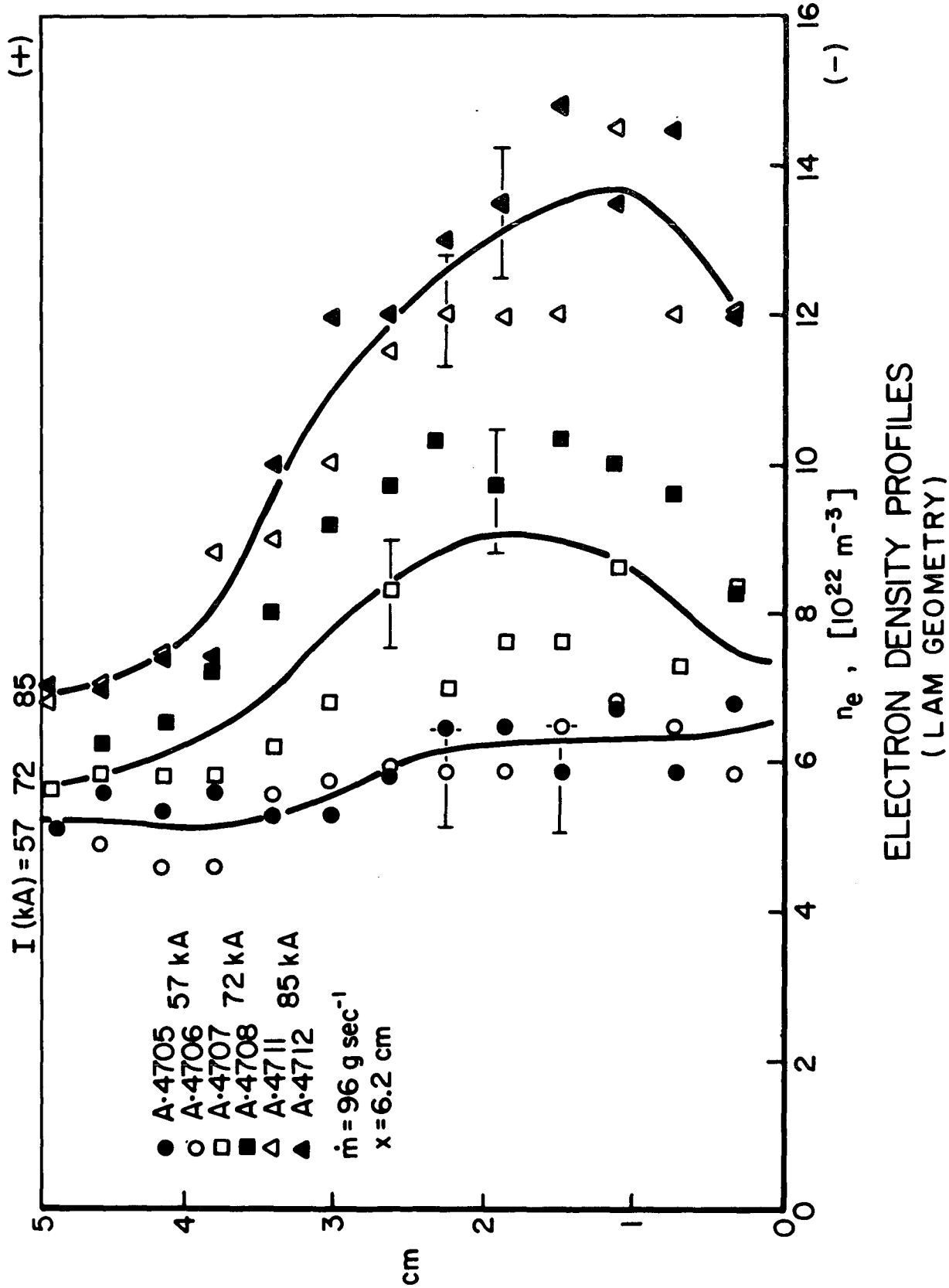

FIGURE A-5
AP25 4778

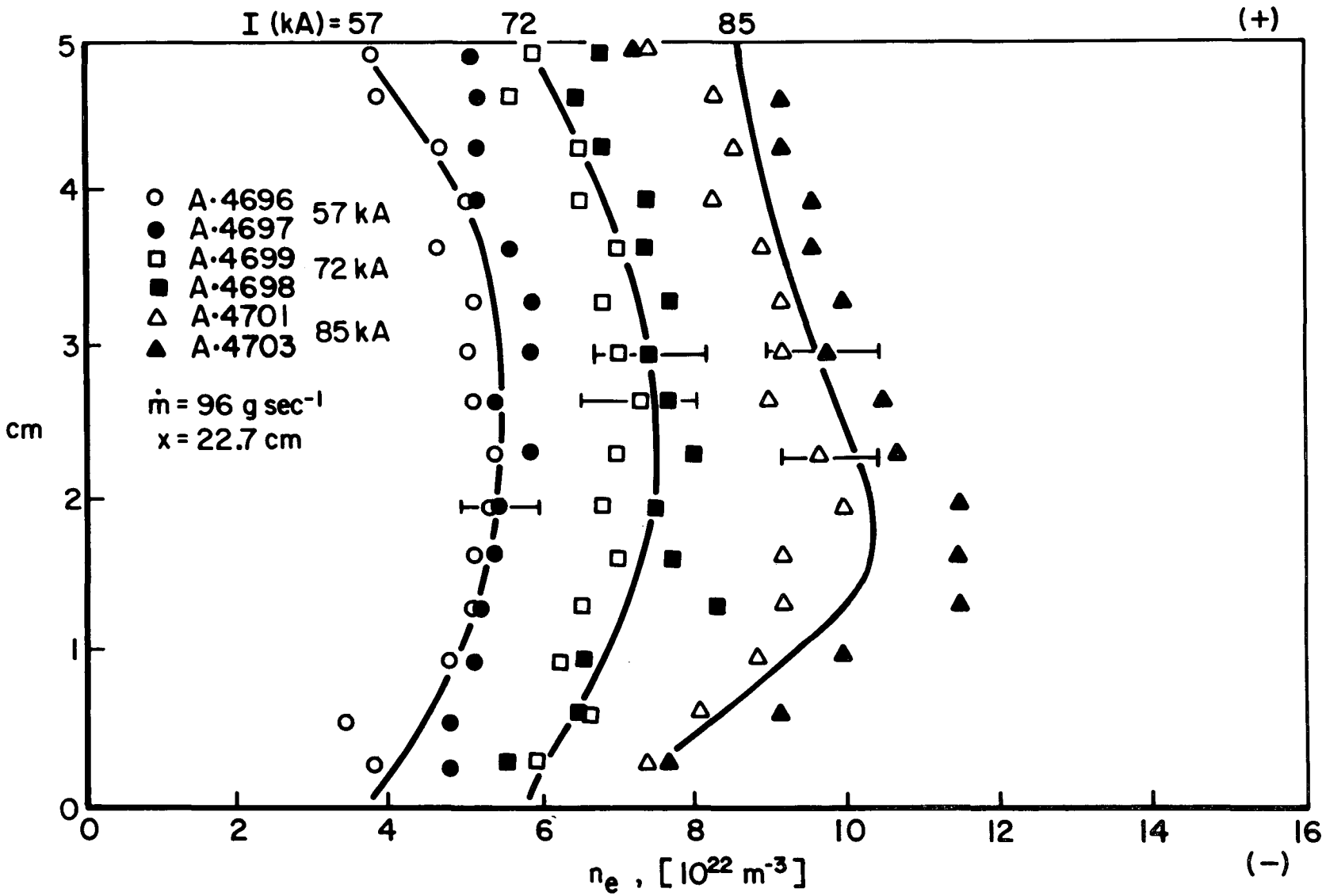

ELECTRON DENSITY PROFILES
(LAM GEOMETRY)

FIGURE A-6
AP25 4777

downstream of the junction, presented in Fig. A-6, are more symmetric, varying little across the height of the channel. The drop of electron density between the two axial positions is small indicating that both expansion of the flow and recombination downstream of the discharge region are not extensive in this geometry. The measured electron densities at the downstream position ($\sim 10^{23}$ m^{-3} for I = 85 kA) are also 30% higher than the densities, shown in Fig. 4-13,measured in the fully insulated geometry.

To estimate the magnitude of the error which arises from the photographic reduction of the spectroscopic data, the measurements of electron density indicated by the hollow data points shown in Figs. A-5 and A-6 were obtained from spectrograms exposed with a T = 0.25 neutral density filter placed in front of the spectrograph slit. The small difference between these measurements and the ones obtained from spectrograms exposed without the neutral density filter (full data points) indicate that the photographic technique described in App. B does not introduce a large systematic error in the measurements.

d) Pressure Measurements

Part (b) of Figs. A-7, A-8, and A-9 displays the pressures measured on the wall of the channel with the pressure probe described in Sec. 4-6 for an argon mass flow of 96 g sec^{-1} and currents of 57, 72, and 85 kA respectively. The pressure records for each current pulse correspond to 4 axial locations along the centerline of the channel wall on the cathode side of the channel, namely, 10 cm upstream of the electrode-insulator junction and 2.5, 6.3, and 22.4 cm downstream of it. The last record in the figures corresponds to the 22.4 axial position, 5 cm off the centerline. Current and voltage records are shown as a reference in part (a) of the figures.

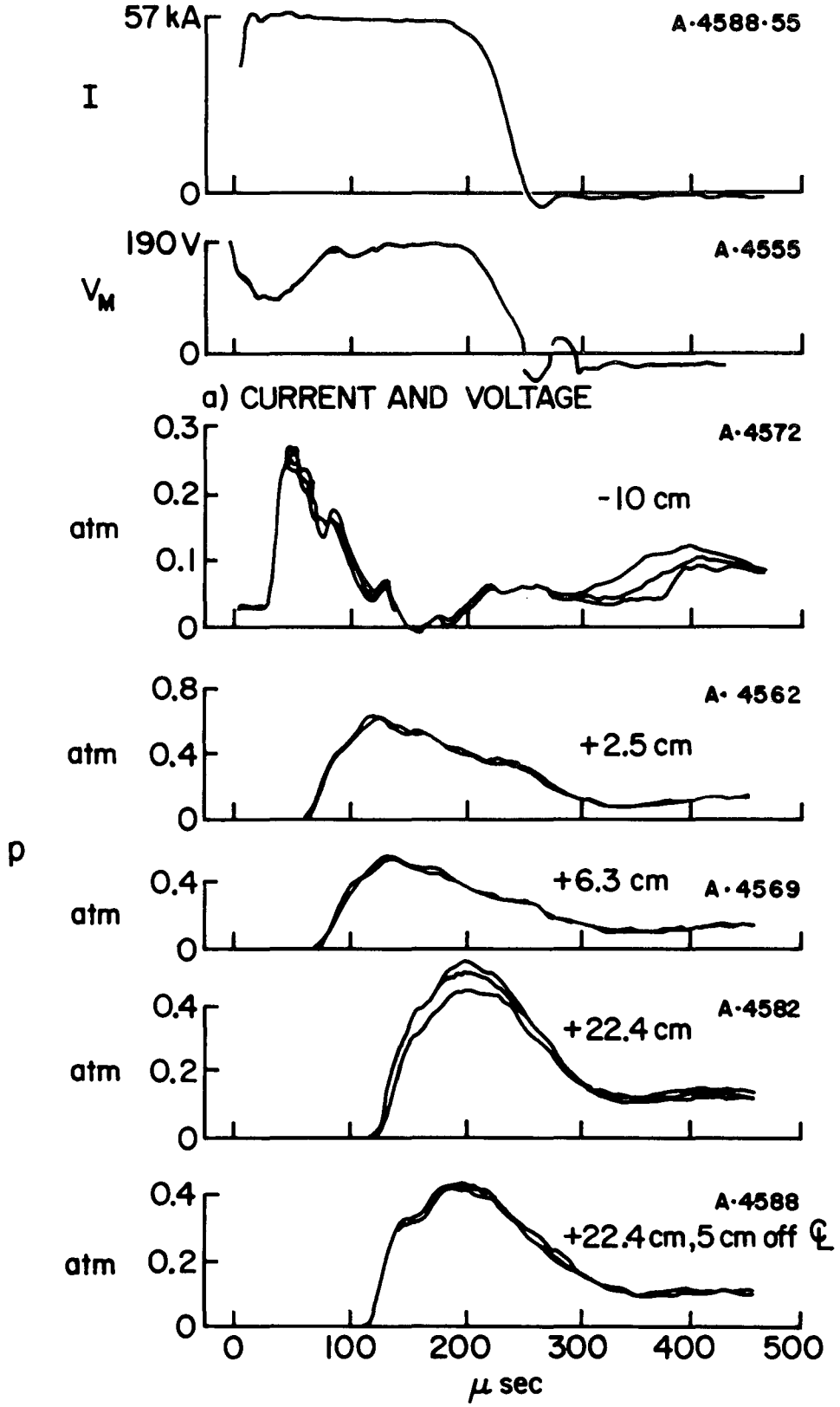

b) WALL PRESSURE

PRESSURE MEASUREMENTS
$I = 57$ kA, $\dot{m} = 96$ g sec^{-1}
(LAM GEOMETRY)

FIGURE A-7
AP25 4783

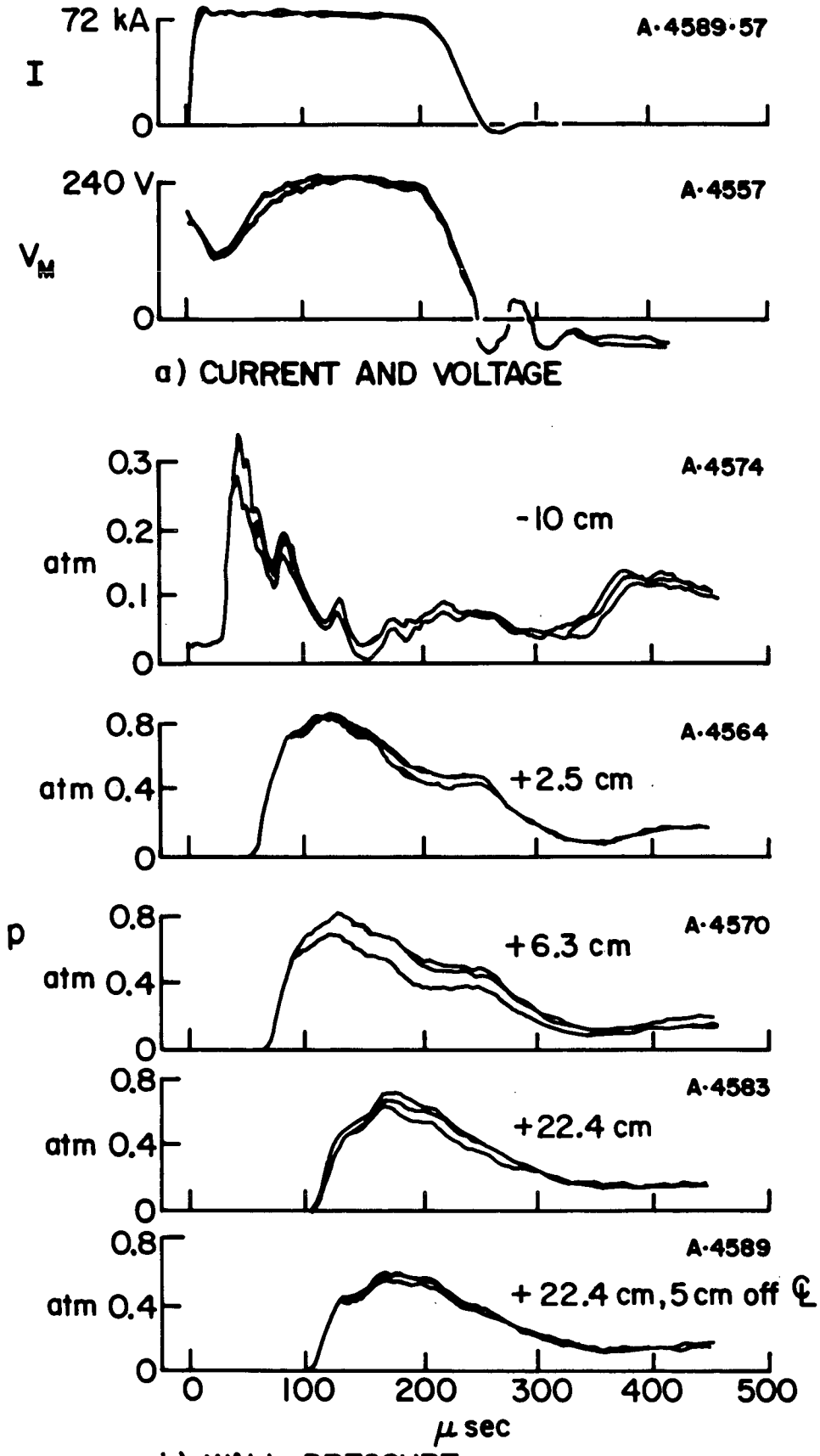

PRESSURE MEASUREMENTS
$I = 72$ kA, $\dot{m} = 96$ g sec^{-1}
(LAM GEOMETRY)

FIGURE A-8
AP25 4782

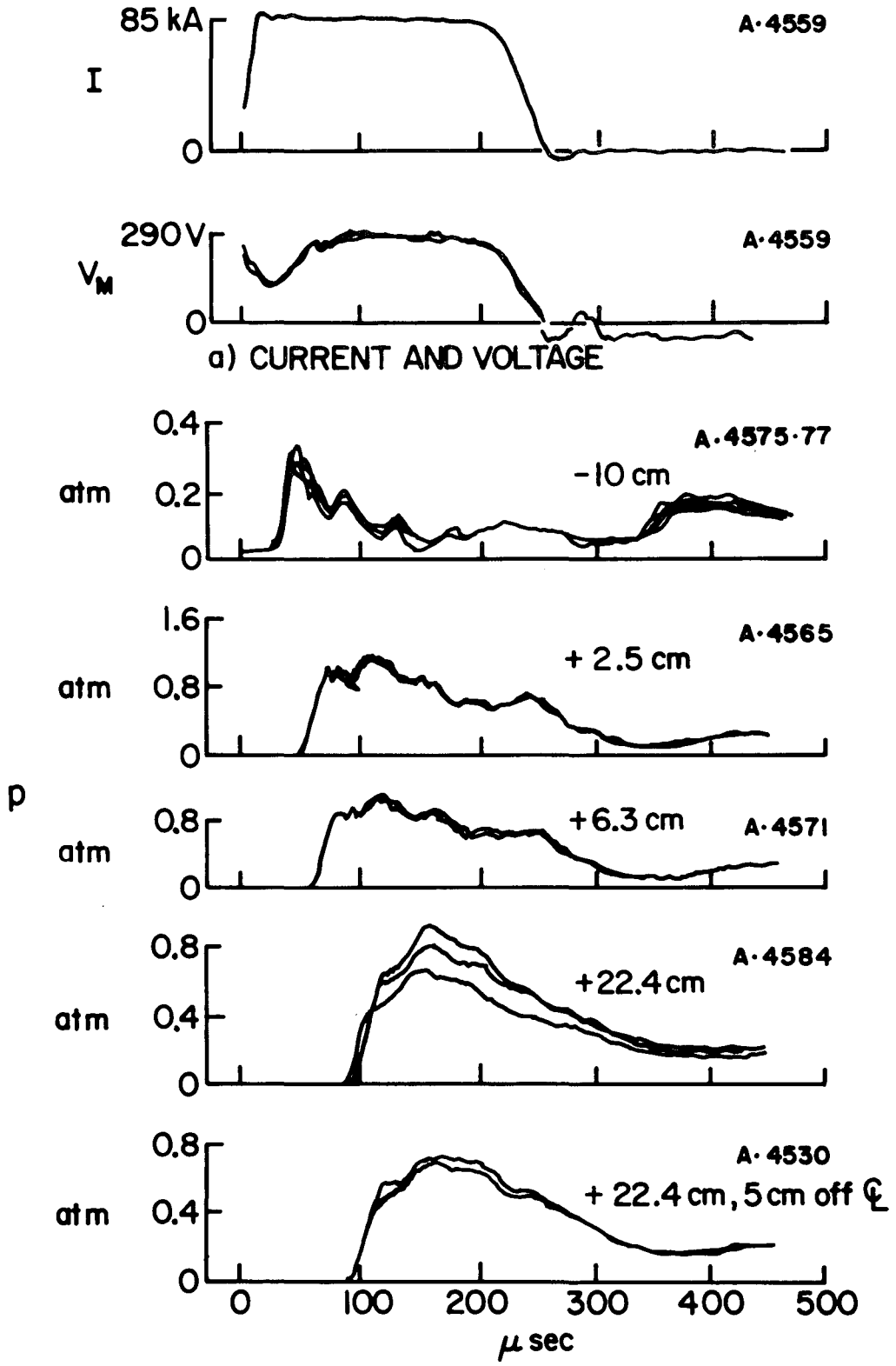

b) WALL PRESSURE

PRESSURE MEASUREMENTS
$I = 85$ kA, $\dot{m} = 96$ g sec^{-1}
(LAM GEOMETRY)

FIGURE A-9
AP25 4784

The wall pressures recorded at the - 10 cm axial position are the same for all three current pulses; they show the initial displacement from the baseline due to cold flow in the accelerator and a peak of 0.3 atm which is believed to be associated with the propagation of the current distribution toward the electrode-insulator junction. The other peaks originate from reflection of stress waves within the stub of the probe. The pressure then drops to a value of 0.02 - 0.05 atm for the rest of the pulse. The measurements 2.5 cm downstream of the junction show a high pressure region with maximum pressures of 0.6 atm for I = 57 kA, 0.8 atm for I = 72 kA and 1.0 atm for I = 85 kA. The pressures at this location achieved steady values of 0.4, 0.6, and 0.7 atm about 170 μsec into the pulse. The magnitude and shape of the pressure signatures obtained at 6.3 cm shows little change from the ones obtained at 2.5 cm. The measured pressures 22.4 cm downstream of the junction are 0.4, 0.5, and 0.6 atm for the three current pulses which suggests that little acceleration of the flow in the axial direction takes place between the 6.3 and 22.4 cm axial positions.

e) Magnetic Field Measurements

The magnetic fields, measured in the accelerator during the quasi-steady portion of the discharge with the techniques described in Sec. 4-7, are presented as the ratio B/B_1 for I = 85 kA in Fig. A-10. B_1 is the calculated magnetic field at the rear wall of the channel. As discussed in Sec. 4-7, for this geometry this ratio is identical to I/I_1 where I_1 is the current in the circuit and I is the current flowing downstream of the probe location. The negative values of B/B_1 are a consequence of 3-D effects which arise due to the finite width of the channel and should not be construed as a flow of negative current. The values of B/B_1 on the cathode side of the channel are very close to the ones obtained in the fully

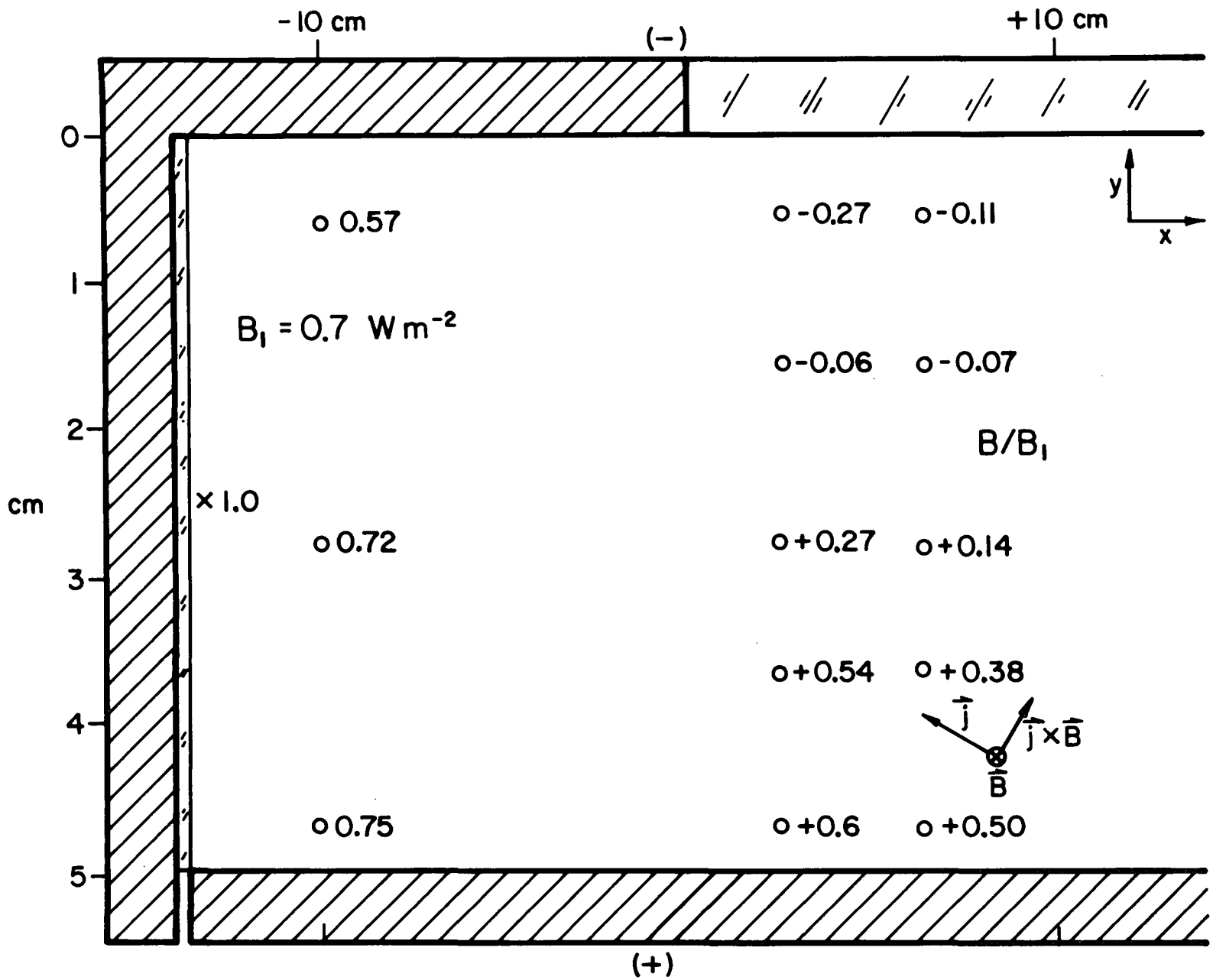

NORMALIZED MAGNETIC FIELD B/B_1
$I = 85$ kA, $\dot{m} = 96$ g sec^{-1}, $t = 80 - 200\ \mu$sec
(LAM GEOMETRY)

FIGURE A-10
AP 25 4780

insulated geometry presented in Fig. 4-23. This is an indication that close to the elecdrode-insulator junction in a parallel-plate geometry the current distributions are the same regardless of the length of the other electrode. On the anode side of the channel (long electrode), a significant fraction of the current flows downstream of the 6.3 cm axial position. This agrees with the photographic observations presented earlier in this section. This tilt of the current distribution towards the insulated side of the channel provides a component of the $\vec{j} \times \vec{B}$ body force which is directed towards the insulated wall. This component gives rise to a pressure gradient along the height of the channel which is believed to be responsible for the high wall pressures measured at these axial positions.

A-3 MOMENTUM AND ENERGY BALANCE

The consistency of the experimental measurements presented in the previous section may be confirmed by the application of the same steady one-dimensional conservation arguments as the ones presented in Secs. 5-5a and 5-5b. The analysis is carried out between two stations in the channel - one located 13.7 cm upstream of the junction and the other 22.7 cm downstream of it.

The results for momentum conservation in the axial direction are presented in Table A-I in page 146 where the column I presents the current in the circuit and the columns p and n_e the average values of pressure and electron density measured 22.7 cm downstream of the junction. As before, the momentum contribution of the inlet flow is neglected. Using the measured values of p and n_e, together with Eqs. 5-27 and 5-28 and, using the calculated values of magnetic pressure $\frac{\mu_0 I^2}{2w^2}$, the average velocity in the exhaust necessary to conserve momentum may be calculated. This velocity, for the three current levels

TABLE A-I MOMENTUM CONSERVATION

$\dot{m}$	I	$\frac{\mu_0 I^2}{2w^2}$	p	n_e	ρ	ρu^2	u	$\dot{m}_p$	M_p
10^{-1} Kg sec^{-1}	10^3 A	10^5 N m^{-2}	10^5 N m^{-2}	10^{22} m^{-3}	10^{-3} Kg m^{-3}	10^5 n m^{-2}	10^3 m sec^{-1}	10^{-1} Kg sec^{-1}	
0.96	85	2.0	0.58	9.4	6.6	1.4	4.7	2.3	1.4
0.96	72	1.4	0.52	6.9	4.5	0.9	4.5	1.6	1.2
0.96	57	0.9	0.35	5.0	3.4	0.5	4.1	1.1	1.0
±20%	± 5%		± 20%	±15%					*

TABLE A-II ENERGY CONSERVATION

$\dot{m}$	I	V	T_i	h	$\frac{u^2}{2}$	$\rho u A(h + u^2/2)$	αVI	$\frac{\rho u A(h + u^2/2)}{\alpha VI}$	$\frac{u^2}{2h}$	V_{uB}	$\frac{V_{uB}}{\alpha V - V_{uB}}$
10^{-1} Kg sec^{-1}	10^3 A	10^2 V	10^4 °K	10^7 m^2 sec^{-2}	10^7 m^2 sec^{-2}	10^7 W	10^7 W			V	
0.96	85	2.9	2.5	6.3	1.2	1.8	2.1	0.85	0.18	33	0.16
0.96	72	2.4	3.5	6.8	1.0	1.2	1.5	0.85	0.15	27	0.15
0.96	57	1.9	3.1	6.6	0.8	0.8	0.9	0.85	0.12	20	0.14
±20%	±5%	±5%									*

*Typical Uncertainties in Experimentally Determined Quantities

is displayed in the column u of the table. The velocities obtained for this geometry, typically of the order of 4-5 x 10^3 m sec^{-1}, are somewhat lower than the ones obtained in the fully insulated geometry (5-6 x 10^3 m sec^{-1}).

The mass flow in the exhaust, calculated on the basis of the measured densities and calculated velocities, is shown in the column m_p. The mass flow is a strong function of current despite the fact that the input argon mass flow is fixed at 96 g sec^{-1}. This appears to indicate that mass is ingested either from the gasdynamic flow established in the accelerator prior to breakdown or from erosion from the insulator surfaces. The mass flows for both geometries are quite similar (Table 5-I in page 119) despite the fact that the fully insulated geometry has a significantly larger area as well as two high pressure regions at the electrode-insulator junctions compared to one such region for the Lam geometry.

The measurements of wall pressure on the insulated (cathode) side of the channel, 2.5, and 6.3 cm downstream of the electrode-insulator junction and the measurements of magnetic field across the height of the channel at the same axial locations may be used with Eq. 5-11 to establish a momentum balance in the y-direction across the discharge. Under the assumptions of: a) steady flow, b) 2-D geometry, i.e., $\frac{\partial}{\partial z} = 0$, c) negligible pressure on the anode side of the channel, Eq. 5-11 takes a particularly simple form:

$$p = \frac{B^2}{2\mu_0} \qquad \text{(A-1)}$$

where p is the measured pressure on the cathode side of the channel and B is the magnetic field measured on the anode side of the channel. It is reasonable to expect assumption (a) to hold after stabilization, (b) may be justified by the small negative value of B on the cathode side of the channel compared to its value on the anode side,

(c) is reasonable on the basis of the pressure measurements upstream of the current distribution and (d) is based upon the requirement of zero velocity normal to the channel wall. The values of p and $B^2/2\mu_o$, which compare very favorably, are presented on the top of Fig. A-12.

An energy balance for this accelerator geometry is presented in Table A-II on page 146 which displays the current I and the terminal voltage V as well as the ion temperatures obtained from the pressure and electron density measurements through the use of Eq. 5-33. Column h in the table shows the enthalpy of the flow, calculated from the ion and electron temperatures through the use of Eq. 5-36. The total power in the exhaust is shown in column $\rho uA(h + \frac{u^2}{2})$. This power compares very favorably to the input power available to the flow expressed as $\alpha V I$ where, as discussed in Sec. 5-5b, the factor $\alpha = 0.85$ takes into account the power lost to the electrodes in the form of anode and cathode falls.

It is instructive to compare the energy deposition ratios in this geometry and in the fully insulated geometry. This ratio is shown in the column $u^2/2h$ which shows that only 15% of the energy in the exhaust appears as directed kinetic energy as opposed to 20% in the fully insulated geometry. The energy deposition ratio based upon the resistive voltage drop and induced emf is shown in the column $V_{uB}/(\alpha V - V_{uB})$ of Table A-II on page 146 which shows reasonable agreement with the ratio $u^2/2h$. These two results indicate that the discharge in both geometries imparts less energy to the flow by direct body acceleration than by resistive heating.

An estimate of the power lost through heat conduction to the walls as well as by radiation is indicated by the ratio $\rho uA(h + u^2/2)/\alpha VI$ shown in Table A-II. According

to this ratio about 85% of the input power delivered to the flow appears in the exhaust. It is therefore estimated that 15% of the input power is lost either by radiation or heat transfer to the walls.

A-4 THE CONVECTION-DIFFUSION MODEL FOR THE ACCELERATION REGION*

A model for the acceleration region, based upon the diffusion of magnetic fields in electrically conducting fluids and the convection of the fields by the flow, may be used to explain some of the experimental observations presented earlier in this appendix. The fundamental equation which governs both of these phenomena may be obtained[36] by eliminating the current density $\vec{j}$ and the electric field $\vec{E}$ from the following equations:

$$\nabla \times \vec{E} = -\frac{\partial \vec{B}}{\partial t} \qquad \text{(Faraday's Law)} \qquad \text{(A-2)}$$

$$\nabla \times \vec{B} = \mu_0 \vec{j} \qquad \text{(Ampere's Law)} \qquad \text{(A-3)}$$

$$\nabla \cdot \vec{B} = 0 \qquad \text{(A-4)}$$

$$\vec{j} = \sigma(\vec{E} + \vec{v} \times \vec{B}) \qquad \text{(Ohm's Law)} \qquad \text{(A-5)}$$

The equation for $\vec{B}$, the magnetic field, in the case of constant scalar conductivity σ for a fluid moving with velocity $\vec{v}$ is:

$$\frac{\partial \vec{B}}{\partial t} = \nabla \times (\vec{v} \times \vec{B}) + \frac{1}{\mu_0 \sigma} \nabla^2 \vec{B} \qquad \text{(A-6)}$$

which states that the local rate of change of the magnetic field $\vec{B}$ results from the net effect of diffusion of the field in the medium and convection of the field by the flow, represented by the Laplacian and curl terms respectively,

*The author is indebted to Prof. S. H. Lam for suggesting the approach presented in this section.

The analogy between Eq. A-6 and the equation which governs the convection and diffusion of vorticity $\vec{\omega}$:

$$\frac{\partial \vec{\omega}}{\partial t} = \nabla \times (\vec{V} \times \vec{\omega}) + \nu \nabla^2 \vec{\omega} \qquad \text{(A-7)}$$

suggests that a magnetic boundary layer model may be used to account for the observed features of the discharge region. As in the case of viscous flow, the model assumes that the flow field may be conveniently separated into two regions: one close to the electrode-insulator junction in which the gradients of magnetic field are large and where most of the current conduction takes place and the other, which has little current conduction through it in which the fields remain undisturbed. This assumption appears reasonable since this effect is quite similar to the skin effect which takes place in good electrical conductors in the presence of time-varying fields. The only difference is that the flow of conducting fluid across the field takes the place of the time derivative of the field.

To establish the characteristic dimension of the region in which the effects of convection and diffusion of the magnetic field become important, an approach similar to the one used to estimate the thickness of conventional boundary layers in viscous flow may be used.[37] To this end, under the assumption of steady 2-D flow geometry, Eq. A-6 becomes:

$$\frac{\partial}{\partial x} uB + \frac{\partial}{\partial y} vB = \frac{1}{\mu\sigma}\left[\frac{\partial^2 B}{\partial x^2} + \frac{\partial^2 B}{\partial y^2}\right] \qquad \text{(A-8)}$$

where u and v are the velocity components in the x and y directions respectively and B is the magnetic field in the z direction. It is useful to non-dimensionalize the above equation utilizing for this purpose the free stream velocity U, and a streamwise coordinate ℓ measured

from the electrode-insulator junction in the downstream direction as shown in Fig. A-11. The distances in the y direction may be nondimensionalized with respect to δ, the thickness of the boundary layer which is assumed to be small. Eq. A-8 therefore becomes:

$$\frac{\partial}{\partial x} uB + \frac{1}{\delta'}\frac{\partial}{\partial y} vB = \frac{1}{\mu_0 \sigma l U \delta'^2}\left[\delta'^2 \frac{\partial^2 B}{\partial x^2} + \frac{\partial^2 B}{\partial y^2}\right] \qquad \text{(A-9)}$$

where δ' is:

$$\delta' = \frac{\delta}{l} \qquad \text{(A-10)}$$

the dimensionless thickness of the magnetic boundary layer.

An estimate of v may be obtained from the continuity equation which, in dimensionless form is:

$$\frac{\partial}{\partial x}\rho u + \frac{1}{\delta'}\frac{\partial}{\partial y}\rho v = 0 \qquad \text{(A-11)}$$

Since the left term of Eq. A-11 is of order 1 (O(1)), v must be of O(δ'). With this assumption, both terms in the left hand side of Eq. A-9 are of O(1). In the magnetic boundary layer, $\frac{1}{\mu_0 \sigma l U \delta'^2}\frac{\partial^2 B}{\partial y^2}$ must also be of O(1). Therefore, it is required that $\mu_0 \sigma l U \delta'^2 \sim O(1)$ and therefore:

$$\delta \sim O\left(\sqrt{\frac{l}{\mu_0 \sigma U}}\right) \qquad \text{(A-12)}$$

The magnetic Reynolds number R_M defined with respect to the height of the channel L is:

$$R_M = \mu_0 \sigma U L \qquad \text{(A-13)}$$

Therefore Eq. A-12 becomes:

$$\delta \sim O\left(\sqrt{\frac{lL}{R_M}}\right) \qquad \text{(A-14)}$$

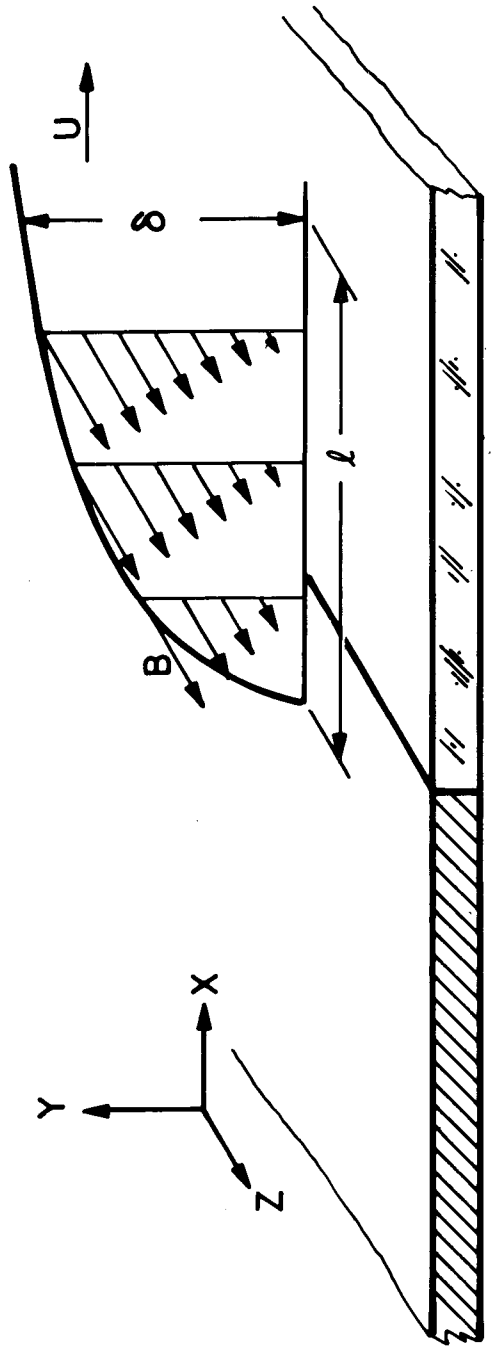

MAGNETIC BOUNDARY LAYER MODEL
(LAM GEOMETRY)

FIGURE A-11
AP25 4792

The coefficient of the right hand side of Eq. A-14 may be obtained from the solution to the complete boundary layer equations.[35] In the limit of:

a) $\frac{B^2}{2\mu_0} \gg p$

b) $R_M \longrightarrow \infty$

c) γ = constant = 2

where p is the thermodynamic pressure of the undisturbed fluid and γ is the ratio of specific heats, the coefficient η of the right hand side of A-14 is:

$$\eta = \left(\frac{2(\gamma-1)(\gamma+2)}{\gamma}\right)^{1/2} \qquad \text{(A-15)}$$

For this accelerator,

$$\gamma = 1.3$$

$$\sigma = 8 \times 10^3 \ \Omega^{-1} m^{-1}$$

$$(n_e = 10^{23} \ m^{-3}, \ T_e = 2.0 \ eV)^{30}$$

$$u = 4 \times 10^3 \ m \ sec^{-1}$$

$$\mu_0 = 4\pi \times 10^{-7} \ H \ m^{-1}$$

$$L = 5 \times 10^{-2} \ m$$

then:

$$R_M = 2$$

$$\eta = 1.2$$

and:

$$\delta = 2\sqrt{\ell} \qquad \text{(A-16)}$$

This parabola, shown as the dashed line in Fig. A-12, represents the edge of the magnetic boundary layer. This

parabola compares very well with the edge of the radiance region shown in the photograph on Fig. A-4, represented by the full line in Fig. A-12. This suggests that despite the drastic approximations involved, i.e.: $R_M = 2 \ll \infty$ and $\gamma = 1.3 \neq 2$, the magnetic boundary layer approximation for this accelerator is a good one. The same figure shows the measurements of magnetic field obtained across the height of the channel. The field which remains undisturbed upstream of the radiance edge, shows a steep gradient in the y-direction downstream of it, in the interior of the proposed magnetic boundary layer region.

To establish a momentum balance in the y-direction assuming steady 2-D flow, the momentum equation is:

$$u \frac{\partial v}{\partial y} + v \frac{\partial v}{\partial y} = -\frac{\partial p}{\partial y} - j_x B \qquad \text{(A-17)}$$

where as before u is the velocity in the x-direction, v is the velocity in the y-direction, p is the pressure of the fluid, j_x is the x-component of current density and B is the magnetic field in the z-direction. Eq. A-3, Ampere's Law may be used to determine j_x:

$$j_x = \frac{1}{\mu_0} \frac{\partial B}{\partial y} \qquad \text{(A-18)}$$

The momentum equation, therefore, becomes:

$$u \frac{\partial v}{\partial x} + v \frac{\partial v}{\partial y} = -\frac{\partial p}{\partial y} - \frac{B}{\mu_0} \frac{\partial B}{\partial y} \qquad \text{(A-19)}$$

Consistent with the magnetic boundary layer approximation ($R_M \rightarrow \infty$), both terms on the left of Eq. A-18 are of $O(\delta')$, the non-dimensional thickness of the magnetic boundary layer (v is of $O(\delta')$. Therefore these terms can be neglected with respect to the right hand side which

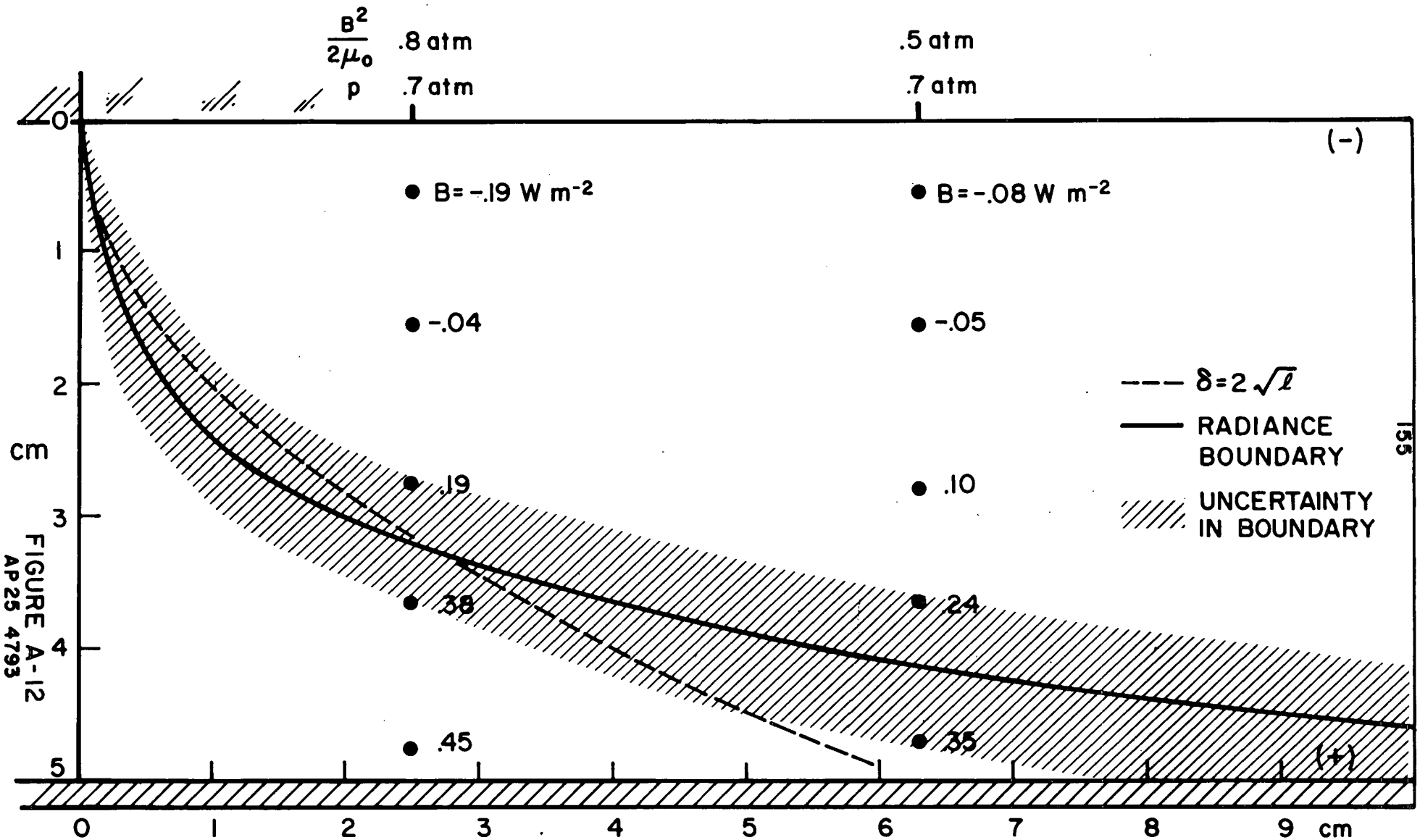

FIGURE A-12
AP 25 4793

SUMMARY OF EXPERIMENTAL OBSERVATIONS
(LAM GEOMETRY)

is of O(1) and which has a straightforward integral:

$$\mathbb{P}(x) = p + \frac{B^2}{2\mu_0} \qquad \text{(A-20)}$$

where $\mathbb{P}(x)$ is constant across the height of the channel. The experimental measurements of p_j 10 cm upstream of the electrode-insulator junction indicate that this quantity is negligible upstream of the magnetic boundary layer region. Therefore the pressure p, measured on the insulated side of the channel (top of Fig. A-12) must be equal to the value of $B^2/2\mu_0$ measured on the uninsulated side of the channel (bottom of Fig. A-12). The two values compare very well as shown along the top of Fig. A-12.

APPENDIX B

PHOTOGRAPHIC DETERMINATION OF SPECTRAL HALF-WIDTHS#

B-1 INTRODUCTION

The measurement of the width at half-intensity of the H_β line recorded photographically is required to determine the electron densities spectroscopically. In this case the measurement is a relative one since both the full intensity used as a reference and the half-intensity to be determined belong to the same spectral line recorded on one photograph. Since the response of the film to radiant energy consists of a silver deposit which is opaque to a luminous flux incident on it, it is required to determine the amount of blackening which arises from a given amount of incident radiant energy.

The blackening of the film is characterized by the quantity D, which is measured directly from the photographic plate. It is defined as:

$$D = \log_{10} \frac{F_i}{F_t} = \log_{10} \frac{1}{T} \qquad \text{(B-1)}$$

where F_i is the luminous flux incident on the silver deposit, F_t is the luminous flux transmitted by the deposit and T is the transmission factor. The incident radiant energy is measured as the exposure E. The exposure has the units of energy per unit area and can be expressed as:

$$E = It \qquad \text{(B-2)}$$

where I is the intensity of the radiation and t is the duration of the exposure in seconds. In the present case the exposure duration is the same for the full-intensity

#A detailed discussion of photographic measurements of radiant energy is presented in Ref. 39

and the half-intensity and therefore the half-intensity and half-exposure points are identical.

It has been found experimentally that the response of the photographic film can be displayed graphically as the D-log E curve, shown in Fig. B-1. The abscissa of the D-log E curve is the logarithm of the exposure while the ordinate is the density which represents the amount of silver deposited on the film. In the figure, D = 0 corresponds to the fog level of the film as it will be explained later. The straight line portion of the curve, between the points marked A and B, defines the region of correct exposure. Throughout this region, the density is directly proportional to the log of the exposure. To relate the measured change in D which accompanies a given change in E, a precise knowledge of the constant of proportionality γ, which is the slope of AB, is necessary. γ depends on the film as well as the developer used, its concentration, temperature, and time of development. To insure reproducible values of γ every time a photograph is developed, meticulous handling and processing of the film is required.

In general, the response of the film is proportional to It^p (Schwarzschild Law) where p is a function of the exposure time. Therefore the shape of the D-log E curve depends on the mode of exposure as well. Thus it is necessary to establish the response curve for the film and the developing process employed with an exposure which resembles closely in duration, intensity and wavelength, the exposure for which measurements are to be taken.

B-2 DETERMINATION OF γ

To establish the D-log E curve, the film was exposed through a step tablet in the spectrograph using the optical arrangement shown in Fig. B-2a. The light source is a commercially available Mity Lite Model 1 Xenon flash lamp, which delivers a light pulse with an intensity profile shown

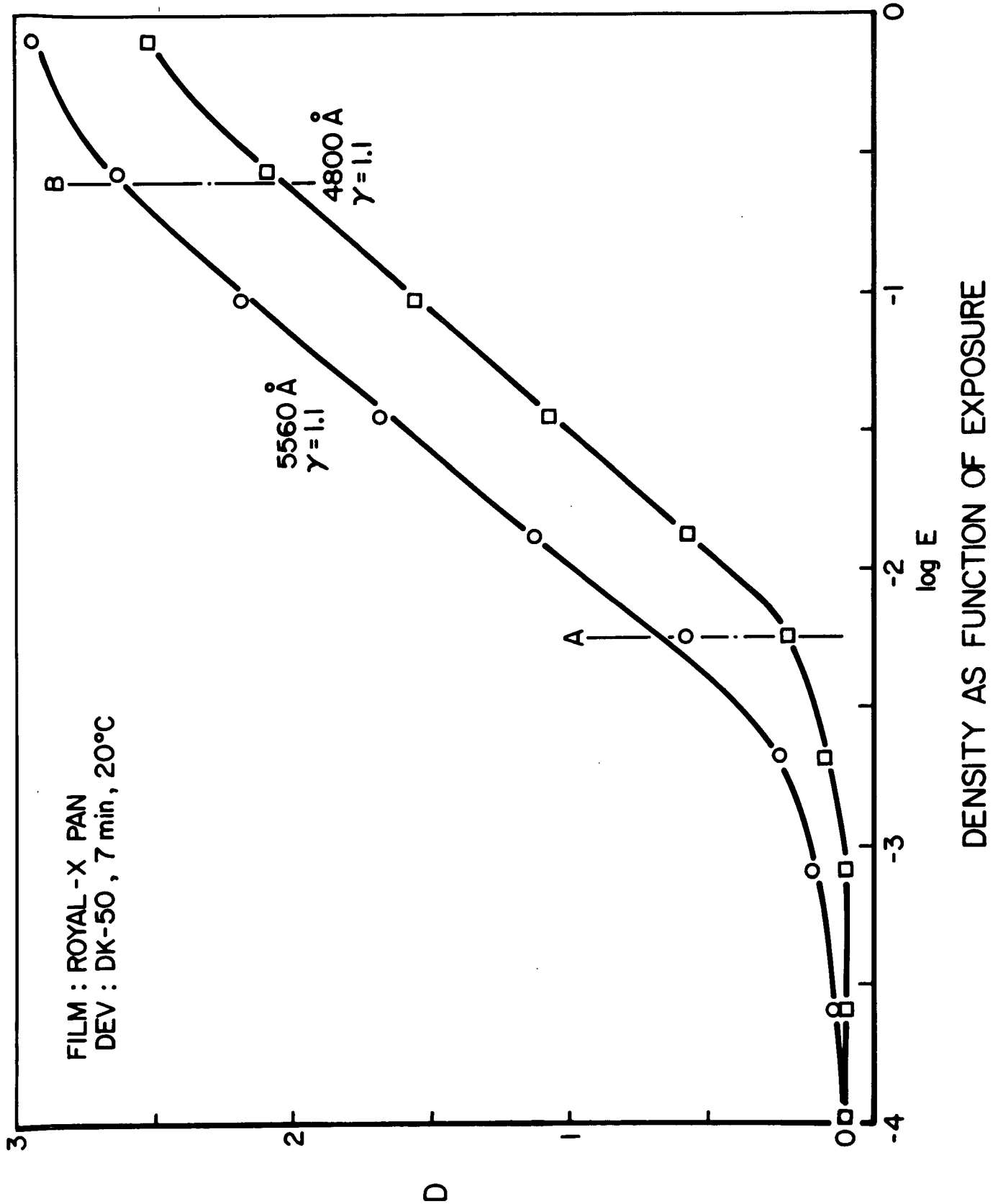

DENSITY AS FUNCTION OF EXPOSURE

FIGURE B-1
AP25 4765

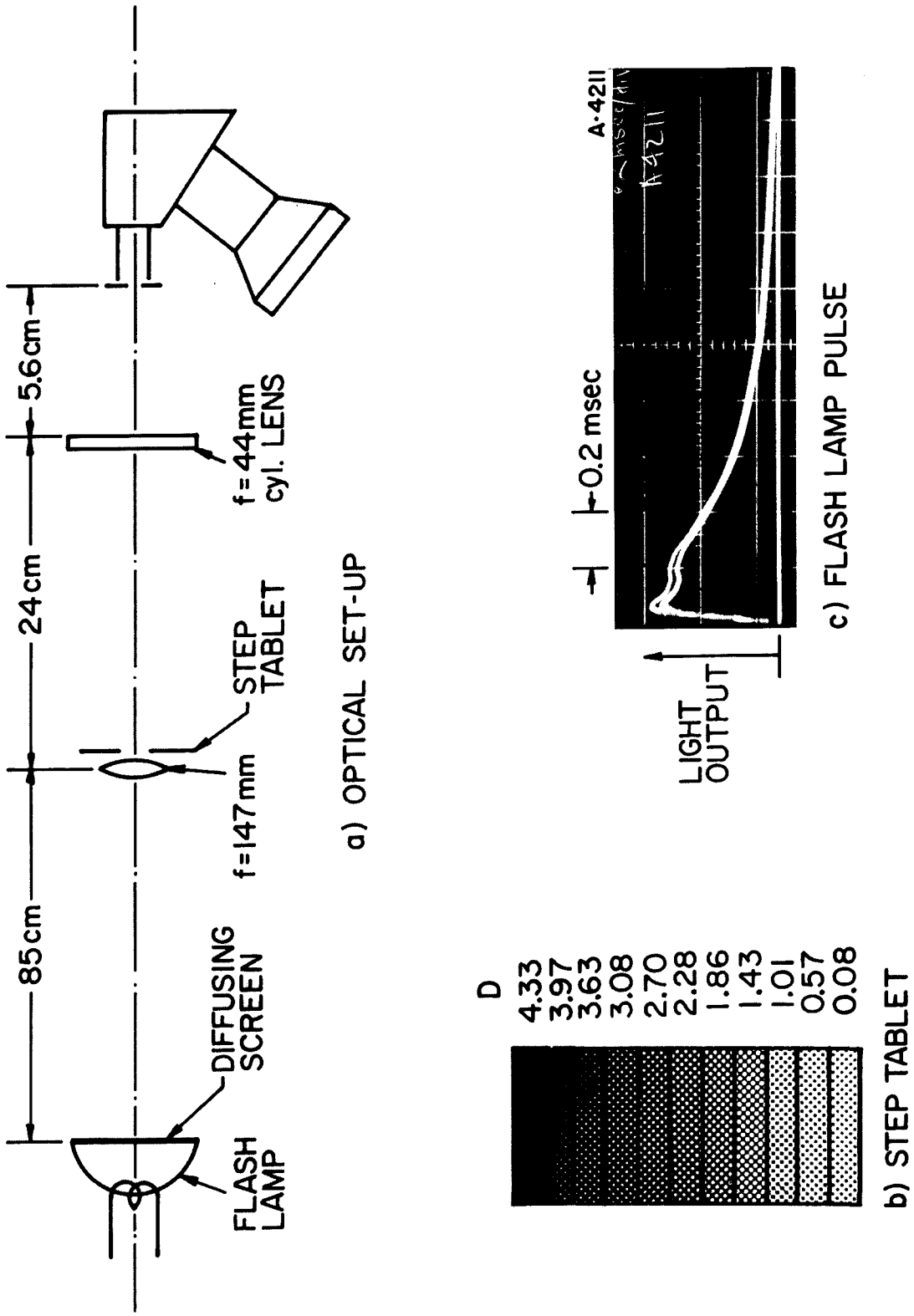

FIGURE B-2
AP25 P406

in Fig. B-2c. The pulse, recorded with an EG & G Lite Mike detector Model 560-61, consists of a flat top portion with a duration of 0.2 msec and an exponential decay with a τ_D = 0.4 msec. The light pulse delivered by this lamp is the closest approximation to the radiance profile of the parallel-plate accelerator which has a duration of 0.25 msec. The flash lamp is equipped with a translucent diffuser screen to provide a uniform illumination of the step tablet. The step tablet (Kodak 1A), shown schematically in Fig. B-2b, consists of a piece of photographic film exposed and developed to provide ten consecutive density steps in the range $0.08 \leq D \leq 4.3$, measured with a Jarrel Ash recording microdensitometer. Since the luminous flux transmitted by the steps is directly related to their density through Eq. B-1, the tablet provides a convenient method to produce a variable exposure on the photographic film. The step tablet is imaged on the spectrograph slit with the aid of a cylindrical lens shown in Fig. B-2a.

The photographic film and development procedure used are

Film:	Royal-X Pan (Kodak)	
Speed:	1000 ASA	
Developer:	DK-50	(Kodak)
Concentration:	Full Strength	
Temperature:	20 ± 0.5 °C	
Duration:	7.0 min	
Agitation:	Nitrogen burst 1 sec duration 30 sec interval	
Stop Bath:	Acetic Acid	(5%)
Duration:	45 sec	

Fixer: Kodak Acid Fixer
Concentration: Full Strength
Duration: 5 min

Wash: Tap Water
Duration: 1 hour

Typical film response curves at 5560 Å and at 4800 Å obtained with the optical arrangement and development procedure described above are shown in Fig. B-1. The density D was obtained directly from the transmission factor measured with the Jarrel-Ash microdensitometer. The density D = 0 corresponds to the transmission of the fog level of the film which is arbitrarily set equal to one. Since the measured density variations over an exposure taken without the step tablet are ± 0.3 over a mean density of 2.5, the error introduced by a nonuniform exposure is small. The exposure of the film is assumed to be directly proportional to the transmission of the step tablet and log E = 0 corresponds arbitrarily to the exposure with no step tablet present. The slope of the linear portion of the response curve between the points A and B is γ = 1.1. The average value of obtained from 13 determinations is:

$$\gamma = 1.07 \pm .09$$

B-3 DETERMINATION OF THE HALF-INTENSITY POINT

In general it is desired to establish the density or transmission factor of the film which corresponds to the 1/m intensity level of the spectral line. By the arguments presented in Sec. B-2, the intensity and exposure are equivalent and therefore the 1/m intensity level corresponds to the 1/m exposure. Since continuum radiation is present in the background of the spectrograms it is necessary to account for this radiation in the reduction of the data. Fig. B-3 shows an idealized transmission profile which corresponds to the measured profile presented in Fig. 4-12. The quantities

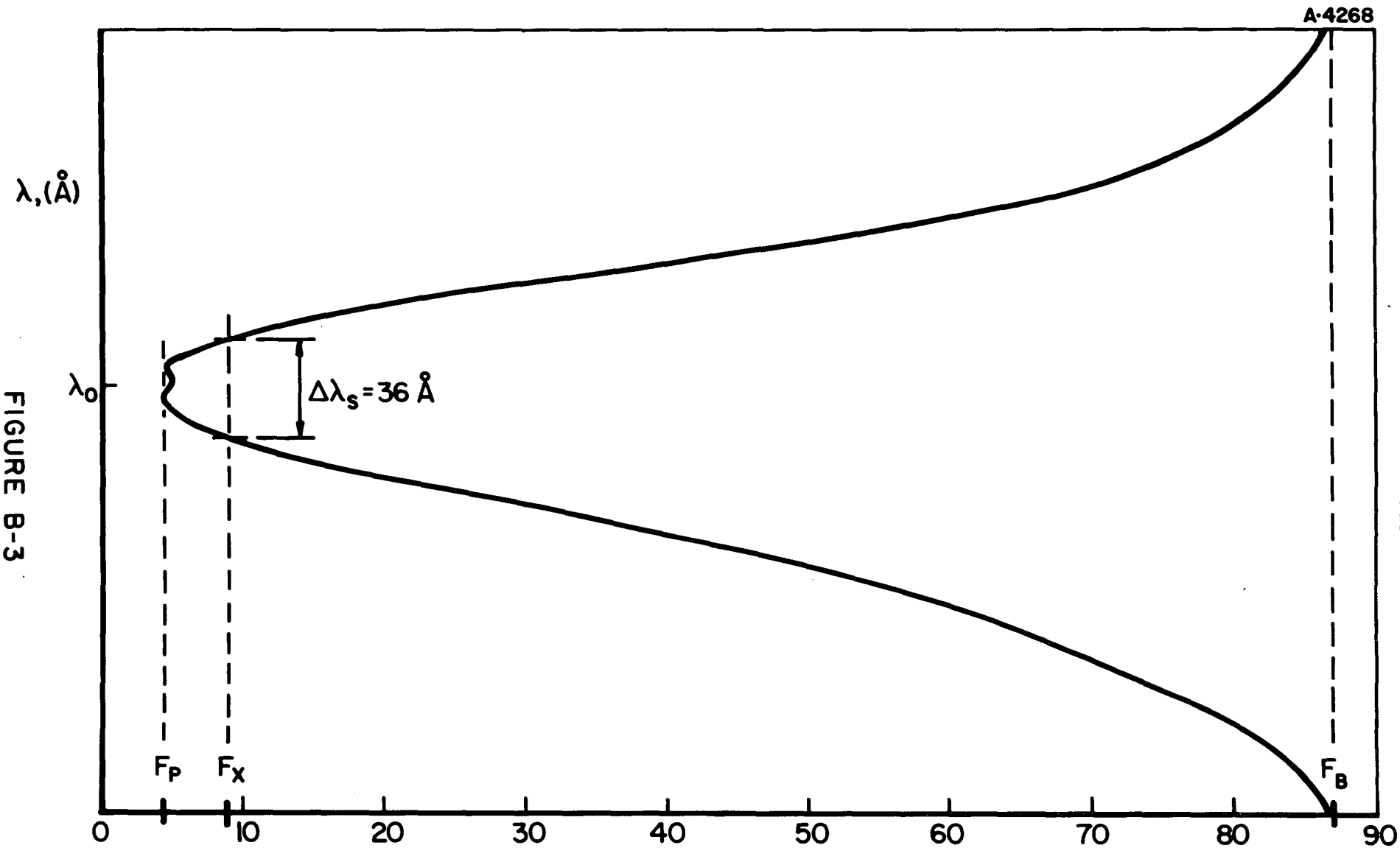

IDEALIZED TRANSMISSION PROFILE
(F_o at 160)

FIGURE B-3
AP25 4763

measured from the profile are:

F_o = Densitometer reading at fog level

F_B = Densitometer reading at background level

F_P = Densitometer reading at maximum intensity (Background + spectral line)

The quantity which is to be determined is:

F_x = Transmission corresponding to 1/m intensity level

For the densitometer used in this work, the reading or deflection F is directly proportional to the luminous flux incident on the detector. Therefore the transmission factors can be obtained as ratios of deflections.

The corresponding exposures are:

E_B = Exposure of background

E_P = Exposure of peak + background

E_{λ_o} = Exposure of peak intensity of spectral line

E_x = Exposure corresponding to 1/m intensity of spectral line

With the definitions above:

$$E_p - E_B = E_{\lambda_o} \tag{B-3}$$

$$E_p - E_x = \frac{m-1}{m} E_{\lambda_o} \tag{B-4}$$

In the linear section of the D-Log E curve:

$$\frac{E_p - E_x}{E_p - E_B} = \frac{m-1}{m} = \frac{\left(\frac{1}{F_p}\right)^{1/\gamma} - \left(\frac{1}{F_x}\right)^{1/\gamma}}{\left(\frac{1}{F_p}\right)^{1/\gamma} - \left(\frac{1}{F_B}\right)^{1/\gamma}} \tag{B-5}$$

Solving for F_x:

$$F_x = F_B\, m^{\gamma}\left(1 + (m-1)\left(\frac{F_p}{F_B}\right)^{1/\gamma}\right)^{\gamma} \qquad \text{(B-6)}$$

The ratio F_x/F_B as a function of F_p/F_B for m=2 and γ = 1.1 is shown in Fig. B-4. Equation B-6 takes a particularly simple form for two limiting cases:

$$\frac{F_x}{F_p} = m^{\gamma} \qquad \text{for} \qquad (m-1)\left(\frac{F_p}{F_B}\right)^{1/\gamma} \ll 1 \qquad \text{(B-7)}$$

$$\frac{F_x}{F_p} = 1 + \alpha\frac{m-1}{m} \qquad \text{for} \qquad \alpha = 1 - \frac{F_p}{F_B} \ll 1 \qquad \text{(B-8)}$$

The result in the second case is independent of γ . Another simple case is the one with no background present. In this case, the solution of B-3 and B-4 with E_B = 0 yields

$$\frac{F_x}{F_p} = m^{\gamma} \qquad \text{(B-9)}$$

which is identical with Eq. B-7.

For the profile of H_β presented in Fig. 4-13, for example:

F_B = 87

F_P = 4.5

γ = 1.1

m = 2

Substituting these values in Eq. B-6, the result is F_x = 9. Once F_x is located on the transmission profile, the width of the line (H_β) at half intensity can be obtained immediately which for this case is 36 Å corresponding to $n_e = 7 \times 10^{22}\ m^{-3}$.

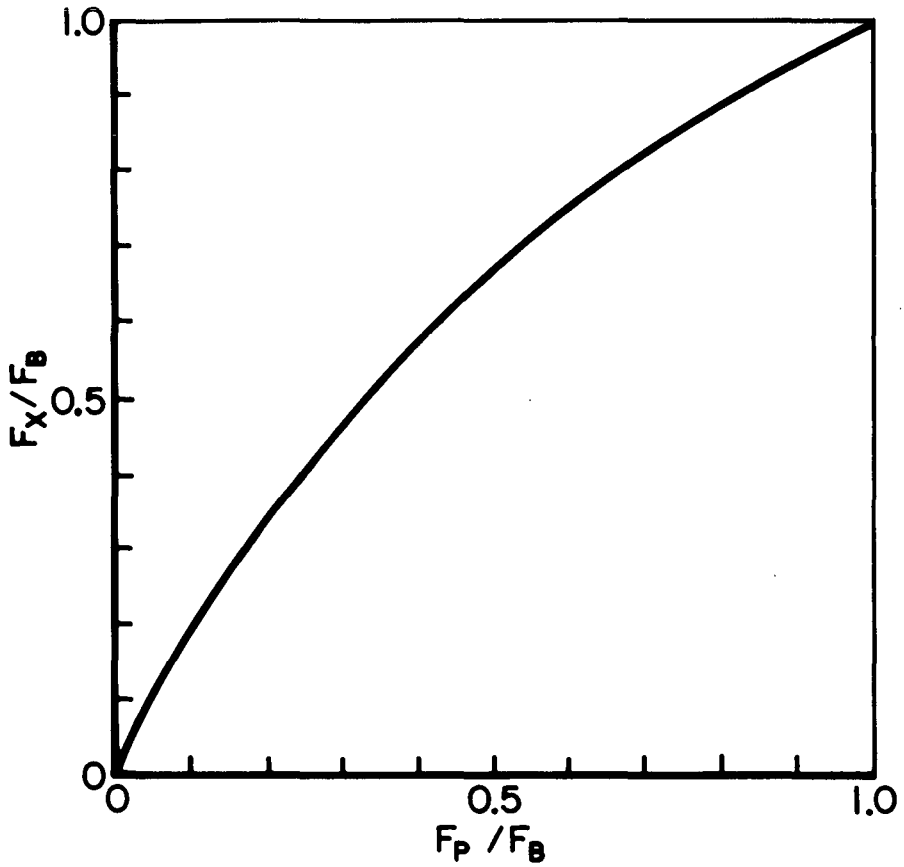

TRANSMISSION FACTOR RATIOS

FIGURE B-4
AP 25 4764

REFERENCES

[1] Jahn, R. G., The Physics of Electric Propulsion, McGraw Hill Book Co., New York, (1966).

[2] Eckbreth, A. C. and Jahn, R. G., "Current Pattern and Gas Flow Stabilization in Pulsed Plasma Accelerators," Aerospace and Mechanical Sciences, Report 857, Princeton University, Princeton, N. J. (1968).

[3] Clark, K. E. and Jahn, R. G., "Quasi-steady Plasma Acceleration," Princeton University, Aerospace and Mechanical Sciences Report 859, Princeton, N. J., (1969).

[4] Black, N. A. and Jahn, R. G., "Dynamics of a Pinch Discharge Driven by a High Current Pulse-forming Network," NASA NsG-306-63, Aerospace and Mechanical Sciences Rept. No. 718, Princeton University, Princeton, N. J., (1966).

[5] Wilbur, P. J. and Jahn, R. G., "Energy Transfer from a Pulse Network to a Propagating Current Sheet," AIAA Journal, Vol. 8, No. 1, Jan. 1970, pp. 144-149.

[6] White, H. J., Gillette, P. R., and Lebacqz, J. V., The Pulse-Forming Network," in: Pulse Generators, G. N. Glasoe and J. V. Lebacqz (eds.), M.I.T. Radiation Lab. Series, Vol. 5, McGraw Hill Co., New York, (1948).

[7] Cushman, R. and Stong, C. L., "Two devices for electric welding, one using a carbon torch and the other a rat-trap," in: The Amateur Scientist, Sci. Am., Vol. 215, No. 5, pp 147-148.

[8] Leonard, S. L., "Basic Macroscopic Measurements," in: Plasma Diagnostic Techniques, R. H. Huddlestone and S. L. Leonard (eds.), Academic Press, New York, (1965).

[9] "Radio Instruments and Measurements," U. S. Dept. of Commerce, National Bureau of Standards, Circular C74, (1937).

[10]Timoshenko, S., and Young, D. H., Elements of Strength of Materials, D. Van Nostrand Co., Inc., Princeton, N. J., (1962).

[11]Murray, J. G., and Bronner, A., "Application of Fuses for D. C. Capacitor Banks," AIEE Paper CP-62-1437, (1962)

[12]McFarlane, H. G., "A High Voltage Quick-acting Fuse to Protect Capacitor Banks," in: Exploding Wires, W. G. Chase and H. K. Moore (eds.), Plenum Press, Inc., New York, (1959).

[13]Bishop, A. E., and Edmonds, G. D., "Electrolytic Resistors in Plasma Physics Research," Plasma Physics (J. Nucl. Energy Pt. C), 7, pp. 423-426, (1965).

[14]Gross, R. A. and Miller, B., "Plasma Heating by Strong Shock Waves," Columbia University School of Engineering, Rept. No. 39, AFOSR AF49 (638)1634.

[15]Murray, J. G. and Farley, R. D., "Voltage Doubler Rectifier, Plasma Physics Laboratory, Report MATT-110, (1962).

[16]Clark, K. E., DiCapua, M. S., Jahn, R. G., and von Jaskowsky, W. F., "Quasi-steady Magnetoplasmadynamic Arc Characteristics," AIAA Paper 70-1095, AIAA 8th Electric Propulsion Conference, Stanford, Calif., 31 Aug.-2 Sept. 1970.

[17]Jahn, R. G. et al., "Pulsed Electromagnetic Gas Acceleration," NASA NgL 31-001-005 Progress Report 1 January 1970 to 30 June 1970, Aerospace and Mechanical Sciences Rept. No. 634o, July 1970, Princeton Univ., Princeton, N. J.

[18]Jahn, R. G., von Jaskowsky, W. F., and Casini, A. J., "Gas-Triggered Pinch Discharge Switch," Rev. Sci. Instr. 34, 12, pp. 1439-1440, (1963).

[19]Jahn, R. G., et al, "Acceleration Patterns in Quasi-steady MPD Arcs," AIAA Journal, 9, 1, pp. 167-172 (1971).

[20]Ames Research Staff, "Equations, Tables and Charts for Compressible Flow," NACA Report 1135 (1953).

[21]Griem, H. R., Plasma Spectroscopy, McGraw Hill Book Co., New York, (1964).

[22]Wiese, W. L., "Line Broadening," in Plasma Diagnostic Techniques, R. H. Huddlestone and S. L. Leonard (eds), Academic Press, New York, (1965).

[23]Cory, J. S. and Jahn, R. G., " Mass, Momentum and Energy Balance in an MPD Accelerator," NASA NgL 31-001-005, Aerospace and Mechanical Sciences Rept. No. 999T, Princeton Univ., Princeton, N. J., (1971).

[24]Lovberg, R. H., "Magnetic Probes," in Plasma Diagnostic Techniques, R. H. Huddlestone and S. L. Leonard (eds), Academic Press, New York, (1965).

[25]Liepmann, H. W., and Roshko, A., Elements of Gasdynamics, John Wiley and Sons, Inc., New York, (1965).

[26]Jackson, J. D., Classical Electrodynamics, John Wiley and Sons, Inc., New York, (1963).

[27]Oberth, R. C., and Jahn, R. G., "Anode Phenomena in High Current Discharges," NASA NGL 31-001-005, Aerospace and Mechanical Sciences Rept. No. 961, Princeton Univ., Princeton, N. J., (1970).

[28]Turchi, P. J. and Jahn, R. G., "The Cathode Region of a Quasi-steady Magnetoplasmadynamic Arcjet," NASA NGL 31-001-005, Aerospace and Mechanical Sciences Rept. No. 940, Princeton Univ., Princeton, N. J., (1970).

[29]Jahn, R. G. and von Jaskowsky, W. F., "Pulsed Electromagnetic Gas Acceleration," NASA NGL 31-001-005, Progress report for the period 1 January 1969 to 30 June 1969, Aerospace and Mechanical Sciences Rept. No. 634m, Princeton Univ., Princeton, N. J. (1969).

[30]Jahn, R. G. and von Jaskowsky, W. F., "Pulsed Electromagnetic Gas Acceleration," NASA NGL 31-001-005, Progress report for the period 1 January 1971 to 30 June 1971, Aerospace and Mechanical Sciences Rept. No. 634q, Princeton Univ., Princeton, N. J., (1971).

[31]Jahn, R. G., von Jaskowsky, W. F., and Clark, K. E., "Pulsed Electromagnetic Gas Acceleration," NASA NGL 31-001-005, Progress report for the period 1 January 1970 to 30 June 1970, Aerospace and Mechanical Sciences Rept. No. 634o, Princeton Univ., Princeton, N. J. (1970).

[32] Electro Optical Systems Inc., "Mollier Chart for Argon," USAF, OAR, Contract AF 33(657)-7940.

[33] Devoto, R. S., "Transport Properties of Partially Ionized Argon," Physics of Fluids, Vol. 10, No. 2, pp. 354-364, (1967).

[34] Eckert, E. R. G., Heat and Mass Transfer, McGraw Hill Book Co., Inc., New York (1959).

[35] Lam, S.H., Private Communication (1970).

[36] Shercliff, J. A., A Textbook of Magnetohydrodynamics, Pergamon Press, London, (1965).

[37] Prandtl, L. and Tietjens, O. G., Applied Hydro and Aeromechanics, Dover Publications, Inc., New York, (1957).

[38] Spitzer, L., Physics of Fully Ionized Gases, Interscience Publishers, New York, (1962).

[39] Jones, L. A., "Measurements of Radiant Energy with Photographic Materials," in Measurements of Radiant Energy, W. E. Forsythe (ed.), McGraw Hill Book Co., N. Y.,(1937).

[40] White, H. E., Introduction to Atomic Spectra, McGraw Hill Book Co., New York, (1934).

[41] Madorsky, S. L., Thermal Degradation of Organic Polymers, Interscience Publishers, New York, (1964)